

Systematic analysis of double-square-root-based stacking operators

Dissertation with the aim of achieving a doctoral degree
at the Faculty of Mathematics, Informatics and Natural Sciences
Department of Earth Sciences
of Universität Hamburg

submitted by
Ivan Abakumov

2016 in Hamburg

Day of oral defense: 10.01.2017

The following evaluators recommend the admission of the dissertation:

Prof. Dr. Dirk Gajewski

PD. Dr. Claudia Vanelle

Abstract

The development of the stacking theory has certain peculiarities. Almost all new stacking concepts (such as, common-midpoint stack, common-reflection-surface (CRS) stack, etc.) have originally been developed for simulating a zero-offset section from 2D prestack multicoverage monotypic data recorded along a seismic profile. Later, these techniques have been extended to three practically important “special” cases: the case of 3D acquisition geometry, the case of converted (PS) waves and the case of common-offset (CO) sections.

In the last years an increasing number of investigations is devoted to the double-square-root-based (DSR-based) stacking operators: Multifocusing and two extensions of the conventional CRS stack – implicit CRS (i-CRS) and non-hyperbolic CRS (n-CRS). The DSR-based stacking operators use the same kinematic wavefield attributes as the conventional CRS stack. However, due to a double square root structure, the DSR-based stacking operators approximate the diffraction events better than the conventional CRS stacking operator. As a result, stacking with the DSR-based operators provides higher resolved stacked sections and more reliable wavefield attributes which are extremely important for the subsequent processing, imaging and inversion steps.

Recent studies have systematically analyzed the DSR-based stacking operators and have proposed the search of wavefield attributes using global optimization techniques and the proper treatment of the conflicting dip problem. Together with a growing computing power, these studies unlock the full potential of the DSR-based stacking operators. Thus, nowadays, multidimensional stacking with the DSR-based stacking operators and the subsequent analysis of the obtained wavefield attributes constitute an exciting new technology.

In this thesis, I take the next logical step in the evolution of stacking theory and investigate the extension of the DSR-based stacking operators to the three above mentioned “special” cases. I construct extensions of n-CRS and i-CRS stacking operators for the 3D, PS and CO cases. I also present a new stacking operator, so-called explicit DSR stacking operator, which plays a very important role in the theory of DSR-based stacking operators. Furthermore, I investigate the accuracy of stacking operators, the accuracy of obtained wavefield attributes and discuss the implementation of the new stacking operators into the CRS-based software.

The derivations of DSR-based stacking operators require a simplified model to fit seismic data from a heterogenous overburden. It requires an auxiliary medium and an analytical description of the reflector. The existing mechanisms to account for the overburden heterogeneity, either by the shift in velocity (effective medium), or by the shift of the reference time (optical medium), could not yet be extended to the 3D case. Hence, I suggest an auxiliary anisotropic medium, which in the 3D case allows to simulate wavefronts

of complex shape. The auxiliary anisotropic medium and an analytical description of the reflector surface constitute the 3D simplified model, which yields the derivation of the 3D i-CRS, 3D n-CRS and 3D DSR stacking operators.

In the case of converted PS waves, I suggest the simplified model with a constant ratio of P- and S- wave velocities. The PS simplified model together with a newly introduced γ -CMP coordinates, which account for the symmetry of the problem, allow to derive the DSR-based stacking operators for converted waves and formulate the efficient parameter search strategy. Furthermore, for the most general CO case, I demonstrate that similar to the classical CRS stacking operator the DSR-based stacking operators could be derived from the paraxial ray theory. This result justifies the implementation of the DSR-based stacking operators in the case of an anisotropic medium and opens the possibility of construction of an anisotropic velocity model by inversion of the stacking parameters.

Thus, the research presented in this thesis not only provides a theoretical basis for extension of the DSR-based stacking operators to the 3D, PS and CO cases, but also makes practical recommendations regarding the implementation of the new stacking operators. I believe that the results of this work could be a starting point for further investigations and that the technologies presented here will be of high demand by industry and basic research.

Zusammenfassung

Die Entwicklung der Theorie des Stapelns enthält bestimmte Besonderheiten. Fast alle neuen Stapelungskonzepte (wie die common-midpoint Stapelung, common-reflection-surface (CRS) Stapelung usw.) wurden ursprünglich für simulierte zero-offset Sektionen aus 2D prestack multicoVERAGE monotypischen Daten, aufgenommen entlang eines seismischen Profils, entwickelt. Im Laufe der Zeit wurden diese Techniken zu drei praktisch relevanten Spezialfällen erweitert: die 3D Akquisitionsgeometrie, konvertierte (PS) Wellen und die common-offset (CO) Sektion.

In den letzten Jahren hat sich eine steigende Anzahl an Untersuchungen auf die double-square-root (DSR)-basierten Operatoren fokussiert: Multifocusing und zwei Erweiterungen der konventionellen CRS Stapelung – impliziertes CRS (i-CRS) und nicht-hyperbolisches CRS (n-CRS). Die DSR-basierten Stapeloperatoren approximieren Diffraktionen besser als der konventionelle CRS Stapeloperator. Als Resultat liefert die Stapelung mittels DSR-basierten Operatoren besser aufgelöste Stapelsektionen und verlässlichere Wellenfeldattribute, die sehr wichtig für nachfolgende Prozessierung, Abbildung und Inversionsschritte sind.

Kürzlich erfolgte Studien haben die DSR-basierten Operatoren systematisch analysiert und vorgeschlagen die Suche der Wellenfeldattribute mittels globaler Optimierungstechniken und unter Berücksichtigung von interferierenden Wellenfelder (conflicting dips) durchzuführen. Zusammen mit wachsender Rechenleistung ermöglichen diese Studien das volle Potential aus DSR-basierten Stapeloperatoren zu nutzen. Heutzutage stellt multidimensionales Stapeln mittels DSR-basierten Stapeloperatoren und anschließender Analyse der erhaltenen Wellenfeldattributen eine aufregende neue Technologie dar.

In dieser These nehme ich den nächsten logisch folgenden Schritt in der Entwicklung der Stapelungstheorie und untersuche die Erweiterung der DSR-basierten Stapeloperatoren auf die drei genannten Spezialfälle. Ich erweitere die n-CRS und i-CRS Stapeloperatoren für die 3D, PS und CO Fälle. Weiterhin präsentiere ich einen neuen Stapeloperator, den sogenannten explizierten DSR Stapeloperator, der eine sehr wichtige Rolle in der Theorie von DSR-basierten Stapeloperatoren einnimmt. Weiterhin untersuche ich die Genauigkeit der Stapeloperatoren, der erhaltenen Wellenfeldattribute und diskutiere die Implementation des neuen Stapeloperators in die CRS-basierte Software.

Die Ableitungen des DSR-basierten Stapeloperators benötigen ein vereinfachtes Model um seismische Daten bei heterogenem Deckgestein zu beschreiben. Es benötigt ein Hilfsmedium und eine analytische Beschreibung des Reflektors. Der existierende Mechanismus um das heterogene Deckgestein zu berücksichtigen, entweder durch velocity shift (effektives Hilfsmedium) oder time shift (optisches Hilfsmedium), konnte bisher nicht auf den 3D Fall erweitert werden. Daher schlage ich vor ein anisotropes Hilfsmedium zu

benutzen, da es erlaubt Wellenfronten von komplexer Form im 3D Fall zu simulieren. Das anisotrope Hilfsmedium und eine analytische Beschreibung der Reflektoroberfläche stellen das vereinfachte 3D Modell dar, welches die Herleitung der 3D i-CRS, 3D n-CRS und 3D DSR Stapeloperatoren liefert.

Im Falle von konvertieren PS Wellen schlage ich ein vereinfachtes Modell mit konstantem P- und S-Wellen Geschwindigkeiten vor. Das vereinfachte PS Modell zusammen mit neu eingeführten γ -CMP Koordinaten, die die Symmetrie des Problems berücksichtigen, ermöglichen es die DSR-basierten Stapeloperatoren für konvertierte Wellen herzuleiten und die effiziente Parametersuchstrategie aufzustellen.

Weiterhin, für den allgemeinsten CO Fall, demonstriere ich, das ähnlich wie bei dem klassischen CMP Stapeloperator, der DSR-basierte Stapeloperator aus der paraxialen Strahlentheorie hergeleitet werden kann. Das Resultat rechtfertigt die Implementierung des DSR-basierten Stapeloperators im Falle eines anisotropen Mediums und eröffnet die Möglichkeit ein anisotropes Geschwindigkeitsmodell, mittels Inversion der Stapelparameter, zu konstruieren.

Die Forschung, die in dieser These präsentiert wird, liefert nicht nur die theoretische Basis zur Erweiterung DSR-basierter Stapeloperatoren auf die 3D, PS und CO Fälle, sondern macht auch praktische Vorschläge bezüglich der Implementierung des neuen Stapeloperators. Ich glaube die Ergebnisse dieser Arbeit könnten ein guter Startpunkt für weitere Untersuchungen sein, denn die hier präsentierten Technologien sind von großem Interesse in Industrie und Forschung.

Contents

Abstract	i
Zusammenfassung	iii
Introduction	1
1 Theoretical background	5
1.1 Seismic reflection experiment	5
1.2 Common-midpoint stack	7
1.2.1 Normal moveout	7
1.2.2 Shifted hyperbola	9
1.2.3 3D normal moveout	11
1.2.4 Converted waves	12
1.2.5 Common-offset stack	12
1.3 Multidimensional stacking	12
1.3.1 Common-reflection-surface stack	14
1.3.1.1 2D zero-offset CRS stacking operator	15
1.3.1.2 3D zero-offset CRS stacking operator	16
1.3.1.3 Common-offset CRS stacking operator	17
1.3.1.4 CRS stacking operator for converted waves	17
1.3.2 Double-square-root-based stacking operators	17
1.3.2.1 Multifocusing	18
1.3.2.2 Implicit CRS	20
1.3.2.3 Non-hyperbolic CRS	21
1.4 Conclusions	22
2 Theory of 3D DSR-based stacking operators	25
2.1 Introduction	25
2.2 Statement of the problem	26
2.3 Coordinate system	29
2.4 Auxiliary anisotropic medium	31
2.5 Curvature of reflector	33
2.6 3D simplified model	35
2.7 Implicit stacking operator (3D i-CRS)	36
2.7.1 Linearized iterative approach	37
2.7.2 Trigonometric iterative approach	38

2.8	Explicit stacking operators	39
2.8.1	3D DSR stacking operator	39
2.8.2	3D n-CRS stacking operator	40
2.9	Conclusions	40
3	Accuracy and implementation of 3D DSR-based stacking operators . . .	43
3.1	Applicability of the simplified model	43
3.2	The most effective iterative approach	44
3.3	The most accurate stacking operator	47
3.4	On the role of explicit stacking operators	50
3.5	Computational difficulty	51
3.6	Implementation into the CRS software	51
3.7	Conclusions	52
4	DSR-based stacking operators for converted waves	53
4.1	Introduction	53
4.2	Theory	55
4.2.1	Statement of the problem	56
4.2.2	Simplified model for converted waves	56
4.2.3	γ -CMP coordinates	57
4.2.4	DSR stacking operator for converted waves	58
4.2.5	CRS stacking operator for converted waves	59
4.2.6	n-CRS stacking operator for converted waves	60
4.2.7	Extension to the 3D case	60
4.3	Accuracy and implementation	61
4.3.1	Accuracy of the stacking operators for converted waves	61
4.3.2	Pragmatic search strategy for converted waves	63
4.3.3	Accuracy of the wavefield attributes	64
4.3.4	Complex synthetic data example	66
4.4	Conclusions	66
5	Common-offset DSR stacking operator	69
5.1	Introduction	69
5.2	Traveltime approximation from paraxial ray theory	71
5.3	DSR approximation from paraxial ray theory	73
5.4	Special cases	76
5.4.1	Zero-offset, monotypic waves	76
5.4.2	Zero-offset, converted waves	77
5.4.3	Common-offset, diffractions	78
5.4.4	Anisotropic media	78
5.5	Conclusions	78
	Summary and Outlook	81

A	Traveltime of NIP and normal waves	85
A.1	Traveltimes in inhomogeneous medium	85
A.2	Traveltime of NIP wave in auxiliary medium	86
A.3	Traveltime of normal wave in auxiliary medium	86
A.4	Group velocity components	89
A.4.1	Additional useful relations	89
A.4.2	Ratios of group velocity components	90
A.4.3	Vertical group velocity component	90
B	3D i-CRS stacking operator	91
B.1	Ellipsoidal reflector	91
B.1.1	Parameterization by lateral coordinates	92
B.1.2	Parameterization by polar angles	92
B.2	Linearized iterative approach	92
B.3	Trigonometric iterative approach	93
C	Explicit stacking operators	95
C.1	Alternative representation of n-CRS	95
C.2	3D n-CRS stacking operator	95
C.3	3D DSR stacking operator	96
C.4	Relation between 3D DSR and 3D n-CRS	98
D	Stacking operators for converted waves	99
D.1	Deviation angle	99
D.2	Derivation of DSR-PS stacking operator	100
D.3	Derivation of CRS-PS stacking operator	102
D.4	Derivation of n-CRS-PS stacking operator	103
D.5	DSR-PS stacking operator in CMP coordinates	103
E	PS exact solution	105
E.1	Method	105
E.2	Isochrone of converted wave	106
E.3	Tangency condition	107
E.4	Coefficients of the sixth-order equation	108
	List of Figures	110
	List of Tables	112
	List of Symbols	115
	List of Publications	119
	References	120
	Used software	129
	Acknowledgments	131

Eidesstattliche Versicherung 133

Introduction

Due to the growth of the world population and the rising living standards, the worldwide energy consumption is constantly increasing. Though the world becomes more energy efficient and the alternative energy sources develop, in the near future the hydrocarbons (natural gas, oil, coal) will remain a major source of the energy. Most of conventional reservoirs are already explored and depleted. Future reservoirs characterize by the increasing depth and complexity, giving a constant high demand for innovative and advanced technologies for hydrocarbon exploration.

The reflection seismic method is the most effective geophysical method for hydrocarbon exploration. The goal of the reflection seismic method is to create an image of the Earth's subsurface using the reflected seismic waves. The seismic image contains valuable information about the location and configuration of the seismic reflection horizons. There are two types of the seismic images: images in the time domain (linked to the vertical two-way travelttime) and images in the depth domain (linked to the depth).

Imaging in time domain was historically the first type of imaging. Its development was closely related to the ability to digitize analog signals. An image in the time domain may be obtained, for instance, by stacking the common-midpoint (CMP) gathers, first suggested by [Mayne \(1962\)](#). Over the last fifty years, this simple CMP stacking has evolved into a sophisticated technology that requires complicated mathematics and state-of-the-art computation ([Rashed, 2014](#)).

The last 20-30 years have seen a growing interest in the methods for imaging the subsurface in depth domain. The main feature of these methods is the requirement of an initial velocity model. The modern strategy for imaging in depth domain is based on the full waveform inversion (FWI) for an iterative update of the initial velocity model and further prestack depth migration (PSDM) performed using the resulting velocity model (see e.g. [Warner et al., 2013](#)). This procedure allows reconstruction of highly resolved depth images of the subsurface with correct locations and dips of the reflection horizons. However, the quality of the depth imaging depends significantly on the initial velocity model, which should be sufficiently close to the true velocity model.

On the contrary, imaging in time domain does not require the initial velocity model. Moreover, it extracts the stacking parameters that may be used to estimate the velocity

model for subsequent imaging steps. Currently, about 70% of the seismic reflection data are processed only in the time domain (Landa, 2007), mainly due to the lower cost of imaging in time domain compared to imaging in depth domain. Hence, the development of improved algorithms for imaging in time domain is a promising research topic.

The multidimensional stacking is a modern method for imaging in time domain. It consists of stacking traces in the neighboring CMP gathers. The multidimensional stacking significantly increases the stacking fold, which results in the enhanced continuity of reflection horizons and the improved image resolution. This procedure requires the stacking operator: an expression describing the traveltime of the reflected wave.

Two alternative multidimensional stacking operators have been proposed almost simultaneously at the end of the 20th century: the common-reflection-surface (CRS) stacking operator (Mann et al., 1999; Jäger et al., 2001) and the Multifocusing (MF) stacking operator (Gelchinsky et al., 1999; Tygel et al., 1999). Both stacking operators are formulated in terms of near-surface kinematic wavefield attributes of Hubral (1983) and are valid for arbitrary velocity models and arbitrary source-receiver pairs in the vicinity of the chosen imaging point. Both CRS and MF give comparable results for reflection events.

However, the seismic wavefield contains not only reflection events but also diffraction events. The "diffractions" appear at terminations of reflectors (e.g., at faults, edges, pinch-outs) and at small scattering inhomogeneities of the subsurface. The diffractions carry valuable information necessary for the velocity model building (e.g., by means of the NIP-wave tomography, Duvencok, 2004; Bauer et al., 2016b), for the migration velocity analysis (Fomel et al., 2007) and for the recovery of structures smaller than the seismic wavelength (Khaidukov et al., 2004).

The CRS stacking operator cannot properly fit traveltimes of diffraction events, whereas the MF stacking operator is designed to account for diffraction events. Hence, the MF stack produces better stacked sections (images) than the CRS stack (Landa, 2007). In order to improve the performance of the conventional CRS stack, two alternative approaches have recently been proposed: the implicit CRS (i-CRS) stack (Schwarz et al., 2014) and the non-hyperbolic CRS (n-CRS) stack (Fomel and Kazinnik, 2013). Since MF, i-CRS and n-CRS describe the traveltime of the reflected/diffracted event as a sum of two square roots, they are called "double-square-root-based" (DSR-based) stacking operators. Recent studies (Schwarz et al., 2015; Walda et al., 2016) indicate that all DSR-based stacking techniques give superior results compared to the conventional CRS stack.

All multidimensional stacking operators (CRS, MF, i-CRS and n-CRS) are traditionally formulated for the 2D zero-offset (ZO) acquisition geometry and monotypic waves. The conventional CRS stack has extensions to three important cases: the case of 3D surveys (Müller, 2003), the case of converted (PS) waves (Bergler et al., 2002) and the case of the common-offset (CO) acquisition geometry (Zhang et al., 2001). However, apart from few exceptions, the DSR-based stacking operators do not have extensions to these special cases.

The conventional CRS stacking operator originates from the paraxial ray theory (see

e.g. Hubral et al., 1992). Moser and Červený (2007) recently formulated the paraxial ray theory for the general anisotropic case. This opens the possibility of a large number of applications, including the estimation of the kinematic wavefield attributes in the general anisotropic media. The DSR-based stacking operators are usually derived from the model-based approach. The question naturally arises whether it is possible to derive the DSR-based stacking operators from the paraxial ray theory and, thus, extend them to general anisotropic media.

In this thesis, I present the extensions of the DSR-based stacking operators to the three special cases (3D, PS, CO) and demonstrate the derivation of the DSR-based stacking operators from the paraxial ray theory. The thesis is structured as follows.

In **Chapter 1**, I review the theory of stacking starting from the classical CMP stack over the CRS stack to the modern DSR-based stacking operators. I also discuss extensions of these stacking techniques to three special cases: the 3D case, the case of converted PS waves and the case of CO acquisition geometry. Furthermore, I introduce and explain notations and terms that are used in the next chapters.

Chapter 2 is dedicated to the theory of 3D stacking operators. I suggest a 3D simplified model which consists of the curved reflector in the auxiliary anisotropic medium. Based on this 3D simplified model, I propose the 3D extensions of the i-CRS and n-CRS stacking operators and the completely new 3D DSR stacking operator.

In **Chapter 3** I investigate the accuracy of the new 3D stacking operators based on the simple numerical tests. I also discuss the implementation of the new stacking operators into the CRS-based software.

Chapter 4 is concerned with the stacking operators for converted PS waves. Based on a fairly reasonable assumption of constant ratio of P- and S-wave velocities, I suggest extensions of the DSR and n-CRS stacking operators to the case of converted waves. Furthermore, I introduce a pragmatic search strategy for converted waves, similar to the one suggested by Müller (1999) for monotypic waves. The new stacking operators and the new pragmatic search strategy together form an efficient tool to obtain high-quality stacked sections for converted PS waves.

In **Chapter 5**, based on the paraxial ray theory, I obtain the DSR stacking operator for the most general common-offset (CO) case. This expression extends the range of applicability of the DSR-based stacking operators and demonstrates their close relationship with the standard CRS stacking operators.

In **Summary and Outlook**, I conclude the results of this thesis and provide an outlook to future directions of investigations.

Chapter 1

Theoretical background

“Everything that happens once can never happen again. But everything that happens twice will surely happen a third time”

– Paulo Coelho, *The Alchemist*

Stacking is one of the basic steps of the reflection data processing workflow. In this chapter, I attempt to present, in historical sequence, the main stages of the development of the stacking theory. I also introduce and explain notations and terms that will be used in the next chapters.

1.1 Seismic reflection experiment

The seismic reflection experiment consists of the recording of reflected seismic waves. The seismic waves are generated by a seismic source (dynamite charge, vibrator, airgun, etc.) that is located at a ground level or is buried in the ground at a shallow depth (see Figure 1.1a). The seismic waves propagate in a complex inhomogeneous medium that is often called "overburden" or "subsurface". The velocity of propagation of seismic waves depends on rock properties, density and other factors (see, e.g., [Sheriff and Geldart, 1995](#)). At a boundary of different rocks (reflecting surface, "reflector"), a discontinuous change of the rock properties occurs. In such a case, an incident seismic wave is partly reflected and partly transmitted (see Figure 1.1b). The reflected wave returns back to the ground surface, where it is recorded by receivers.

There are two modes of the seismic wave in an isotropic solid medium: a compressional P-wave and a shear S-wave. These waves travel in the medium with different velocities. Since the velocity of the S-wave is about half that of the P-wave, the reflected PP wave comes before the reflected SS wave. The reflected PP waves are usually investigated in the

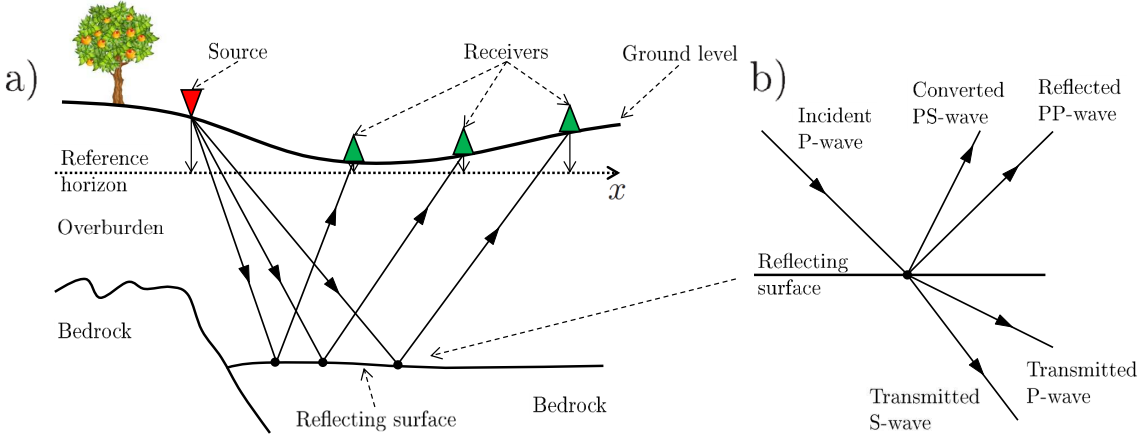


Figure 1.1: Illustration of the seismic reflection experiment. The incident seismic wave, emitted by the source, reflects from the reflecting surfaces to the receivers on the ground surface (a). At the reflecting surfaces the incident seismic wave is partly reflected, partly converted and partly transmitted (b). The red and green triangles indicate the source and receiver locations, respectively.

seismic reflection experiment.

During the reflection, the mode conversion can occur at the reflecting surface. The converted PS and SP waves are formed as the wave changes the mode. The converted PS waves are commonly used to obtain valuable information about S-wave velocities.

The seismic reflection experiments are complicated by topographic variations and complex low-velocity near-surface structures. In order to overcome these problems, static corrections (constant timeshifts) are applied to the recorded data (Cox, 1999). After the static correction, the sources and the receivers belong to the reference horizon (so-called "measurement surface") and the complex low-velocity near-surface layers are replaced by constant-velocity layers.

It is usually assumed that the reference horizon is located at a zero depth $z = 0$. In the 2D case, the measurements are performed along the seismic profile. Seismic data are generally acquired in the shot-receiver (x_s, x_g) coordinates, where x_s and x_g denote the shot and receiver locations along the profile. However, the processing of seismic data is usually carried out in the midpoint-offset coordinates:

$$x_m = \frac{x_g + x_s}{2}, \quad h = \frac{x_g - x_s}{2}, \quad (1.1)$$

where x_m is the midpoint location and h is the half-offset (the half distance from the source to the receiver). As a result of the seismic reflection experiment the traces as a function of the traveltime t , the midpoint x_m and the half-offset h (so-called "prestack seismic data") $P(t, x_m, h)$ are obtained.

1.2 Common-midpoint stack

Stacking of seismic traces, with the goal of improving the signal-to-noise ratio, dates back to the early 1950s. Its development is closely related to the possibility to digitize the analog signals. In 1956, Mayne patented the common-midpoint (CMP) stacking¹. He introduced the midpoint-offset coordinates (1.1) and proposed to collect traces with the same midpoint x_m into the common-midpoint (CMP) gathers. The stacking of traces in the CMP gather yields the stacked trace associated with the midpoint location. This stacked trace approximates the trace that would be recorded if the source and the receiver are located in the midpoint position. Since the useful signals are stacked "in phase" and the noise is often uncorrelated (Sengbush, 1983), the stacked trace has an improved signal-to-noise (S/N) ratio. Theoretically, while stacking, the S/N ratio increases by the square root of the number of traces in the CMP gather (Mayne, 1962). Implementation of the stacking procedure for each midpoint gives the CMP-stacked section (zero-offset section).

The geometry of the CMP gather and the raypath associated with the plane horizontal reflector are presented in Figure 1.2a. Due to the difference in the raypaths, the traveltime t_0 of the zero-offset ray² is not equal to the traveltime $t(h)$ of the ray from the remote source to receiver. The dependence of traveltime with the offset is called "moveout". The difference between $t(h)$ and t_0 is called "moveout correction". Stacking of the seismic traces in the CMP gather requires the moveout approximation $t = \tau(t_0, h)$. With the introduced notations, the CMP stacked section $S(t_0, x_m)$ can be described as:

$$S(t_0, x_m) = \int P(\tau(t_0, h), x_m, h) dh. \quad (1.2)$$

Below, I discuss several moveout approximations used in the CMP processing.

1.2.1 Normal moveout

The moveout approximation that accounts for the difference of the source-receiver distance is called "normal moveout" (NMO). The NMO equation reads:

$$t^2(h) = t_0^2 + \frac{4h^2}{v_{\text{NMO}}^2}. \quad (1.3)$$

This approximation was derived for different earth models:

- **Constant velocity model with a single horizontal plane reflector** (Figure 1.2a). This case was considered by Green (1938) for measuring the average velocity above the reflector. In this case, the stacking velocity v_{NMO} is equal to the velocity of the layer v .

¹Originally, Mayne called his method the "common reflection point horizontal stacking".

²The ray whose source and receiver are located at the midpoint x_m . Also called "central ray" or "normal incidence ray".

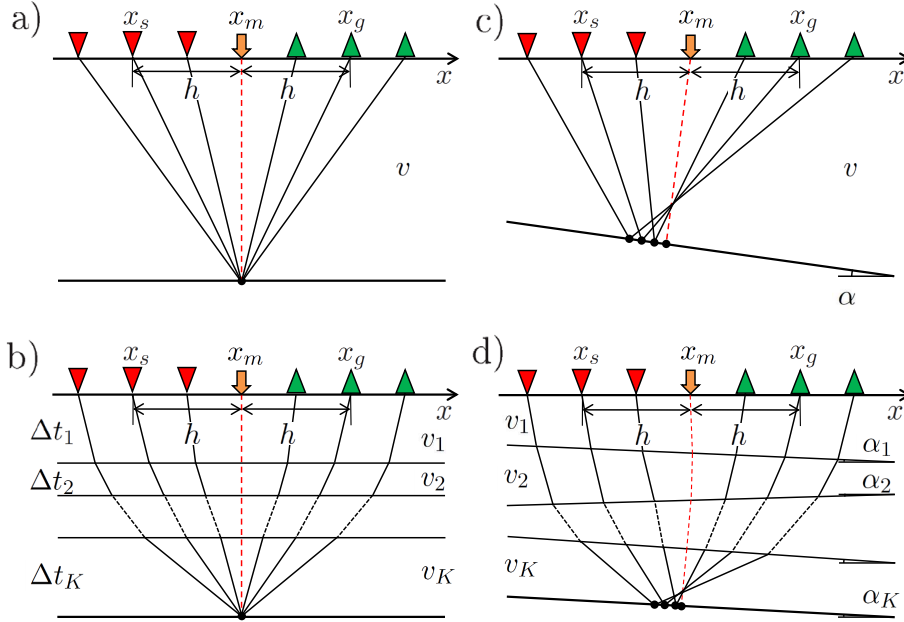


Figure 1.2: Illustration of the simple earth structure models: the plane horizontal reflector (a), the plane dipping reflector (c), the system of horizontal layers (b) and the system of dipping layers (d). The red dashed line indicates the trajectory of the normal incidence ray.

- **Horizontally layered model** (Figure 1.2b). The traveltime approximation for this case have been obtained independently by [Dix \(1955\)](#) and [Dürbaum \(1954\)](#). They showed that in this case the NMO velocity is equal to the root-mean-square (RMS) velocity:

$$v_{\text{RMS}} = \sqrt{\frac{1}{t_0} \sum_{k=1}^K \Delta t_k v_k^2}. \quad (1.4)$$

Here v_k is the interval velocity of the k th layer and Δt_k is the two-way traveltime in the layer k . In this case the NMO (1.3) is a small-offset approximation ([Castle, 1994](#)). [Bolshykh \(1956\)](#) and [Taner and Koehler \(1969\)](#) presented the long-offset moveout approximations using the Taylor series expansion:

$$t^2(h) = c_1 + c_2 h^2 + c_3 h^4 + c_4 h^6 + \dots \quad (1.5)$$

They showed that the first two coefficients of (1.5) coincide with the NMO (1.3) approximation and the next coefficients are the complex functions depending on the interval velocities. [Taner and Koehler \(1969\)](#) also provided the recursive formulas to obtain all coefficients of the series.

- **Constant velocity model with a single dipping plane reflector** (Figure 1.2c). [Levin \(1971\)](#) considered this oversimplified case for understanding the dependence of the stacking velocities on the dip of the reflector α . He found that the NMO equation (1.3) is still valid and the stacking velocity is the same as or higher than

the velocity of the layer v :

$$v_{\text{NMO}} = v / \cos \alpha. \quad (1.6)$$

For this simple model the assumption that the traces in the CMP gather image the same point in depth is violated. Hence, the effect of the reflection-point dispersal occurs. To correct for this effect a dip-moveout (DMO) correction was introduced. For the review of different DMO methods, see [Hale \(1991\)](#) and references therein.

- **System of dipping layers** (Figure 1.2d). [Hubral and Krey \(1980\)](#) proved that the NMO approximation (1.3) is valid in this general case.

[Fomel and Stovas \(2010\)](#) fairly noticed that the hyperbolic behaviour of the moveout is always valid around the zero offset, "thanks to source-receiver reciprocity³ and first-order Taylor series expansion". However, except for a few special cases, the moveout shows a nonhyperbolic behaviour at large offsets.

In summary, the stacked section is obtained as follows. The prestack data are sorted in the CMP gathers (see Figure 1.3a). In the CMP gather each time sample is considered as t_0 (see Figure 1.3b). The NMO (1.3) is calculated for a set of the NMO velocities from the initially defined range. The objective function that measures the similarity of traces, e.g., semblance ([Taner and Koehler, 1969](#)), is estimated for each of these NMO velocities. The stacking velocity is the one that maximizes the value of the objective function. The procedure provides the stacked section, the stacking velocity section and the semblance section. Interpretation of the stacking velocities is performed with the chosen model of the subsurface.

1.2.2 Shifted hyperbola

In the NMO equation (1.3), the inhomogeneity of the overburden is accounted by the NMO velocity. In the presence of inhomogeneity, the NMO velocity becomes an effective velocity, since it depends on the velocities of the layers. Hence, the conventional NMO (1.3) describes the moveout in the effective medium.

[de Bazelaire \(1988\)](#) suggested an alternative idea based on the theory of geometrical optics. He proposed to replace the inhomogeneous medium by the so-called "optical medium" – the homogeneous medium with the constant near-surface velocity v_0 . In the optical medium, the moveout $t(h)$ is described by the shifted-hyperbola⁴:

$$(t - t_0 + t_p)^2 = t_p^2 + \frac{4h^2}{v_0^2}. \quad (1.7)$$

³The traveltime of the monotypic wave is invariant with respect to the source-receiver change. Mathematically, it means that the traveltime is an even function of the offset $t(-h) = t(h)$ and the first derivative of the traveltime with respect to the offset is equal to zero: $\frac{\partial t}{\partial h} = 0$.

⁴A similar approximation was proposed by [Malovichko \(1978\)](#) for the case of the horizontally layered structure.

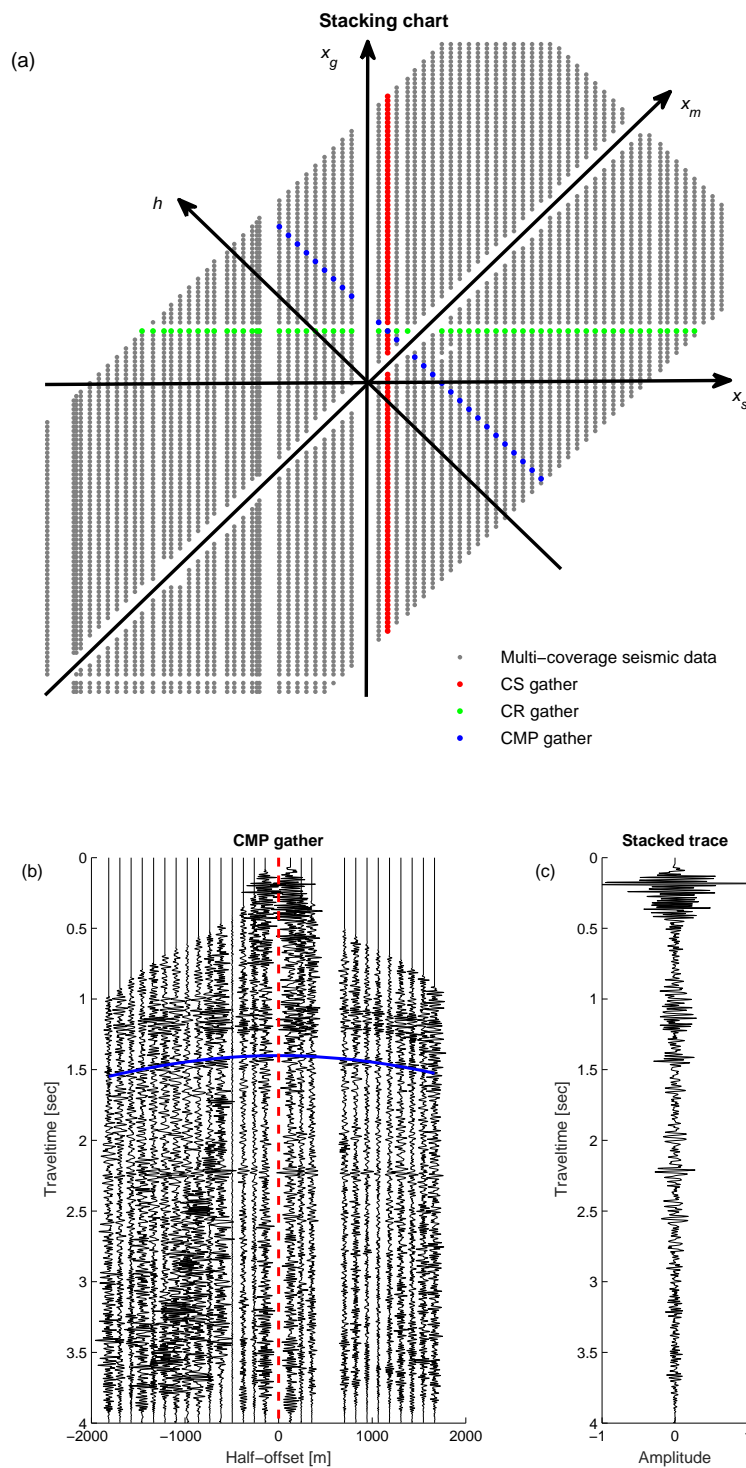


Figure 1.3: (a) Illustration of the geometry of the typical stacking chart. (b) Example of the CMP gather. Stacking is performed along the NMO trajectory (bold blue curve). The procedure provides the stacked trace (c) associated with the zero-offset ray (red dashed line).

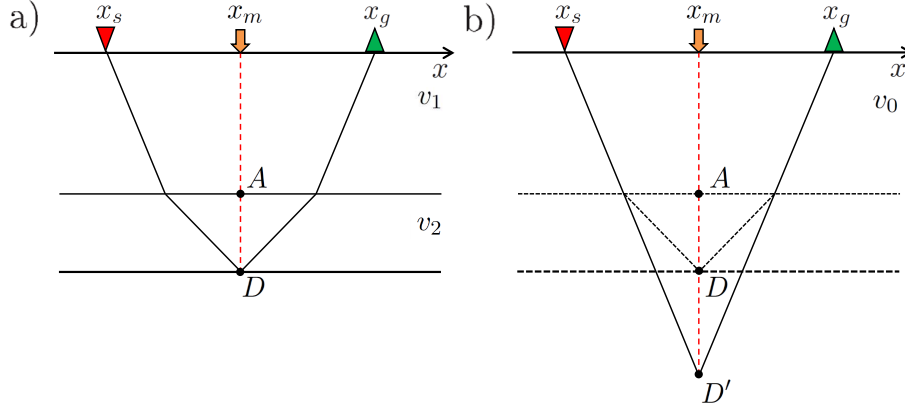


Figure 1.4: The ray scheme for the shifted hyperbola. The actual raypath of the reflected ray (a) in the inhomogeneous model and its equivalent raypath in the optical analog (b). The center of the hyperbola is shifted to the point D' .

Here, t_0 is the two-way traveltimes along the actual raypath $X_m D$ in the inhomogeneous medium and t_p is the two-way traveltimes along the equivalent raypath $X_m D'$ in the optical medium (see Figure 1.4).

In the shifted hyperbola (1.7), the inhomogeneity of the medium is compensated by the so-called focusing time t_p . Thus, both NMO and the shifted hyperbola utilize the concept of auxiliary constant velocity medium, but NMO is formulated for the effective auxiliary medium and the shifted hyperbola for the optical auxiliary medium. One can say that NMO and the shifted hyperbola are the same stacking operator formulated in the different (effective or optical) domains, or utilized the different mechanisms (velocity-shift or time-shift) to account for the inhomogeneity.

1.2.3 3D normal moveout

Subsurface geological features of interest in hydrocarbon exploration are three-dimensional in nature (Yilmaz, 2001). The 3D seismic survey data are used to obtain the true and precise 3D seismic image of the subsurface.

In the 3D seismic surveys, the sources and the receivers are distributed in the measurement surface. In this case, the midpoint x_m and the half-offset h become two-dimensional vectors:

$$\mathbf{x}_m = \frac{\mathbf{x}_g + \mathbf{x}_s}{2}, \quad \mathbf{h} = \frac{\mathbf{x}_g - \mathbf{x}_s}{2}, \quad (1.8)$$

where $\mathbf{x}_s \equiv \{x_s, y_s\}$ and $\mathbf{x}_g \equiv \{x_g, y_g\}$ denote the source and the receiver locations. Traces with the same midpoint locations \mathbf{x}_m are gathered in the CMP bins. The traces of the CMP bin are stacked along the hyperbolic trajectories:

$$t^2(|\mathbf{h}|, \xi) = t_0^2 + \frac{4|\mathbf{h}|^2}{v_{\text{NMO}}^2(\xi)} \quad (1.9)$$

with the NMO velocity depending on the direction of the profile line ξ (Levin, 1971):

$$\frac{1}{v_{\text{NMO}}^2(\xi)} = \frac{\cos^2 \xi}{v_1^2} + \frac{\sin^2 \xi}{v_2^2}. \quad (1.10)$$

Equation (1.10) is known as the NMO velocity ellipse. Alternatively, the 3D NMO (1.9) may be presented in the notations of Grechka and Tsvankin (1999):

$$t^2(\mathbf{h}) = t_0^2 + 4\mathbf{h}^T \mathbf{W} \mathbf{h}, \quad (1.11)$$

where the elements of the symmetric matrix \mathbf{W} are the inverse values of the squared stacking velocities.

1.2.4 Converted waves

The converted PS waves are commonly used to obtain valuable information about S-wave velocities. Extensions of the NMO equation (1.3) for converted waves were proposed by Fromm et al. (1985); Tessmer and Behle (1988); Tessmer et al. (1990); Iverson et al. (1989). The shifted hyperbola moveout approximation for converted waves was formulated by Slotboom (1990). The detailed review of the meaning of converted waves, the difficulties in their processing and the existing moveout approximations are given in Section 4.1.

1.2.5 Common-offset stack

In the common-offset case, the source and receiver locations of the central ray do not coincide. Stacking of seismic traces having the common-offset distances was patented by Harris (1968). For a more detailed discussion of the common-offset stack the reader is referred to Section 5.1.

1.3 Multidimensional stacking

At the beginning of the 1980s, several authors (e.g., Naess, 1982; Buchanan et al., 1983) have pointed out that since traces in the CMP gather do not reflect from one point on the reflector but rather from the segment of the reflector, it is possible to use traces in the neighboring CMP gathers for stacking. Thus, to obtain the stacked trace at the central (imaging) point x_0 , one must consider the traces whose sources and receivers are in a certain vicinity of the central point. In such a situation, the midpoints x_m of the traces being stacked do not coincide with the central point x_0 . The difference between the midpoint x_m and the central point x_0 is called the midpoint displacement:

$$m \equiv x_m - x_0. \quad (1.12)$$

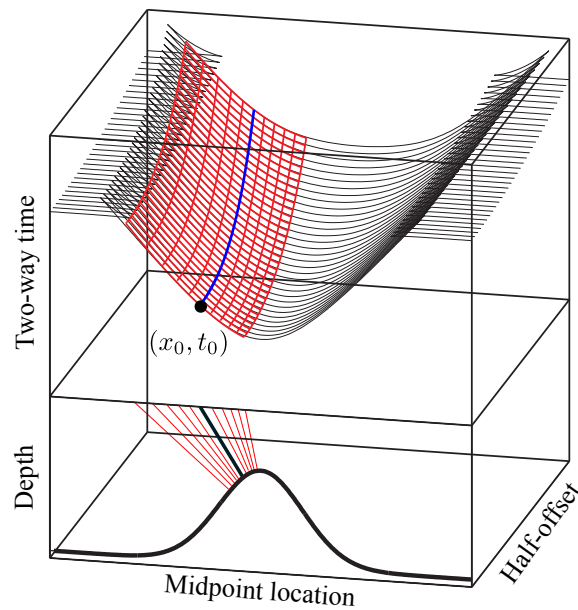


Figure 1.5: The multidimensional (CRS or MF) stacking uses all available traces in the vicinity of the central point x_0 . The multidimensional stacking is performed both in the midpoint and in the half-offset directions, i.e., along the moveout surface $t = \tau(t_0, m, h)$ (red surface). Stacking in both directions significantly increases the amount of stacked traces in comparison to the conventional CMP stacking (bold blue curve). Figure adapted from Müller (1999).

The stacked section $S(t_0, x_0)$ is obtained by stacking the prestack seismic data $P(t, x_m, h)$ both in the midpoint displacement m and the half-offset h directions (see Figure 1.5):

$$S(t_0, x_0) = \iint P(\tau(t_0, m, h), x_0 + m, h) dm dh. \quad (1.13)$$

This procedure requires the moveout approximation $t = \tau(t_0, m, h)$. Since the stacking (1.13) is performed in two dimensions, the procedure is called "multidimensional stacking". As it is apparent from Figure 1.5, the multidimensional stacking significantly increases the stacking fold. Hence, it is particularly useful for data with a low signal-to-noise ratio or acquisitions with a low fold.

Two competing multidimensional stacking techniques appeared almost simultaneously at the end of the 20th century: the common-reflection-surface (CRS) stack (Mann et al., 1999; Jäger et al., 2001) and the Multifocusing (MF) stack (Gelchinsky et al., 1999). Although originated from different theories, both techniques propose the moveout approximations formulated in terms of kinematic wavefield parameters of Hubral (1983) and valid for arbitrary velocity models. Both techniques perfectly handle reflection events, however the MF stack produces better stacked sections due to its ability to properly handle diffraction events (see, e.g., Landa, 2007).

In order to improve the performance of the conventional CRS stack, two alternative approaches have recently been proposed: the implicit CRS (i-CRS) stack (Schwarz et al., 2014) and the non-hyperbolic CRS (n-CRS) stack (Fomel and Kazinnik, 2013). Because MF, i-CRS and n-CRS describe the traveltime of reflected/diffracted event as a sum of two square roots, I will call them "double-square-root-based" (DSR-based) stacking operators. In this section, I will briefly describe these four stacking operators, mention their relations and existing extensions.

1.3.1 Common-reflection-surface stack

The CRS stacking operator⁵ is a natural extension of the NMO equation (1.3) for the multidimensional case. The CRS stacking operator can be derived from the paraxial ray theory for the most general 3D common-offset (CO) case. Here, in contrast, I will start from the most intuitive 2D zero-offset (ZO) case, and later discuss extensions to the 3D and CO cases.

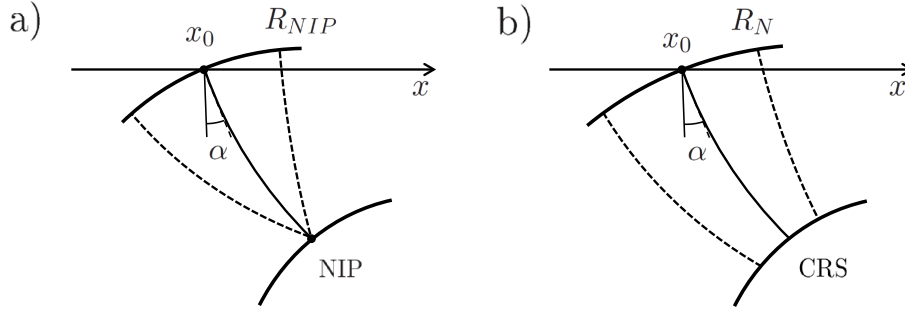


Figure 1.6: Illustration of the kinematic wavefield attributes: α is the dip angle of the zero-offset ray, R_{NIP} is the radius of curvature of the NIP wave (a) and R_N is the radius of curvature of the normal wave (b).

1.3.1.1 2D zero-offset CRS stacking operator

The multidimensional moveout approximation $t = \tau(t_0, m, h)$ may be considered as a truncated Taylor series expansion:

$$t(m, h) = t_0 + \underbrace{\frac{\partial t}{\partial m}}_w m + \underbrace{\frac{\partial t}{\partial h}}_{=0} h + \underbrace{\frac{1}{2} \frac{\partial^2 t}{\partial m^2}}_N m^2 + \underbrace{\frac{\partial^2 t}{\partial h \partial m}}_{=0} mh + \underbrace{\frac{1}{2} \frac{\partial^2 t}{\partial h^2}}_M h^2. \quad (1.14)$$

Due to the reciprocity principle, the first derivative of the traveltimes with respect to the half-offset and the mixed partial derivative are equal to zero. After giving the notations for the non-zero coefficients of the series (1.14), the moveout approximation reads:

$$t(m, h) = t_0 + wm + Nm^2 + Mh^2. \quad (1.15)$$

The last formula is called the parabolic traveltimes approximation. The hyperbolic traveltimes approximation can be immediately obtained by squaring both sides of the parabolic traveltimes formula (1.15) and neglecting the terms of higher order than the second:

$$t^2(m, h) = [t_0 + wm]^2 + 2t_0[Nm^2 + Mh^2]. \quad (1.16)$$

According to numerous investigations (e.g. Ursin, 1982; Mann et al., 1999), the hyperbolic stacking operators better fit the reflection events than the parabolic stacking operators. For a CMP gather, the hyperbolic stacking operator (1.16) reduces to the NMO approximation (1.3).

The paraxial ray theory (Schleicher et al., 1993; Tygel et al., 1997) gives a physical interpretation of the coefficients w^6 , M , N :

$$w = -\frac{2 \sin \alpha}{v_0}, \quad M = \frac{\cos^2 \alpha}{v_0 R_{NIP}}, \quad N = \frac{\cos^2 \alpha}{v_0 R_N}. \quad (1.17)$$

⁵The multidimensional moveout approximation $t = \tau(t_0, m, h)$ is often referred to as "stacking operator".

⁶Note that the sign of the first order derivative w depends on the definition of the coordinate system. The negative sign is chosen here to be consistent with the coordinate systems described in the further chapters.

Here, v_0 denotes the near-surface velocity, α is the dip angle of the zero-offset ray, R_{NIP} and R_{N} are the radii of curvature of the two fundamental waves: the normal-incidence-point (NIP) wave and the normal (N) wave (see Figure 1.6). The NIP wave is a hypothetical wave generated by the fictitious point source placed in the NIP of the zero-offset ray, and the normal wave is a hypothetical wave arising from the fictitious exploding reflector experiment (Hubral, 1983).

The formula (1.16) together with interpretation of the coefficients (1.17) is known as the 2D zero-offset common-reflection-surface (2D ZO CRS) stacking operator. The 2D ZO CRS stacking operator may also be derived by means of the geometrical (model-based) approach of Höcht et al. (1999).

The 2D ZO CRS stacking operator is the core for the CRS stack. Müller (1999); Jäger et al. (2001); Mann (2002) explained in detail the theory and the application of the CRS stack and proposed a pragmatic search of the stacking parameters ($\alpha, R_{\text{NIP}}, R_{\text{N}}$). Mann et al. (1999) showed successful implementation of the idea to the 2D field data.

The CRS stack provides the stacked section, the semblance section and the stacking parameters. The stacking parameters are used in many applications, e.g., the velocity model building (the NIP-wave tomography, Duvencek, 2004; Della Moretta et al., 2006), the prestack data enhancement and interpolation (Baykulov and Gajewski, 2009; Höcht et al., 2009), the diffraction imaging and separation (Dell and Gajewski, 2011; Bakhtiari Rad et al., 2015) and the multiple suppression (Dümmong and Gajewski, 2008). Baykulov et al. (2011) summarized the CRS based workflow.

The CRS stack is a topic of the ongoing research. Of prime interest are the advanced search strategies of the stacking parameters (e.g., by means of global optimization methods, Garabito et al., 2012; Walda and Gajewski, 2015a) and the conflicting dip problem (Müller, 2009; Soleimani et al., 2009; Walda and Gajewski, 2015b).

1.3.1.2 3D zero-offset CRS stacking operator

In the 3D case, the midpoint displacement m and the half-offset h become two-dimensional vectors \mathbf{m} and \mathbf{h} :

$$\mathbf{x}_m = \frac{\mathbf{x}_g + \mathbf{x}_s}{2}, \quad \mathbf{h} = \frac{\mathbf{x}_g - \mathbf{x}_s}{2}, \quad \mathbf{m} = \mathbf{x}_m - \mathbf{x}_0, \quad (1.18)$$

the first-order derivative w transforms to the two-dimensional vector \mathbf{w} , and the second-order derivatives M and N transform to the symmetric 2×2 matrices \mathbf{M} and \mathbf{N} .

The 3D zero-offset common-reflection-surface (3D ZO CRS) stacking operator reads:

$$t^2(\mathbf{m}, \mathbf{h}) = \left[t_0 + \mathbf{w}^T \mathbf{m} \right]^2 + 2t_0 \left[\mathbf{m}^T \mathbf{N} \mathbf{m} + \mathbf{h}^T \mathbf{M} \mathbf{h} \right]. \quad (1.19)$$

The coefficients \mathbf{w} , \mathbf{M} and \mathbf{N} are related to the kinematic wavefield attributes as follows:

$$\mathbf{w} = -\frac{2 \sin \alpha}{v_0} \begin{pmatrix} \cos \beta \\ \sin \beta \end{pmatrix}, \quad \mathbf{M} = \frac{1}{v_0} \mathbf{R} \mathbf{K}_{\text{NIP}} \mathbf{R}^T, \quad \mathbf{N} = \frac{1}{v_0} \mathbf{R} \mathbf{K}_{\text{N}} \mathbf{R}^T. \quad (1.20)$$

Here, v_0 denotes the near-surface velocity, α and β are the dip and the azimuthal angles of the zero-offset ray, \mathbf{K}_{NIP} and \mathbf{K}_{N} are the symmetric 2×2 curvature matrices of the NIP and the normal waves in the ray-centered coordinate system, and \mathbf{R} is the upper left 2×2 part of the 3×3 rotation matrix $\hat{\mathbf{R}}$ that accounts for the transformation from the ray-centered to the general Cartesian coordinate system:

$$\hat{\mathbf{R}} = \hat{\Phi} \hat{\Theta}, \quad \hat{\Phi} = \begin{pmatrix} \cos \beta & -\sin \beta & 0 \\ \sin \beta & \cos \beta & 0 \\ 0 & 0 & 1 \end{pmatrix}, \quad \hat{\Theta} = \begin{pmatrix} \cos \alpha & 0 & \sin \alpha \\ 0 & 1 & 0 \\ -\sin \alpha & 0 & \cos \alpha \end{pmatrix}. \quad (1.21)$$

The 3D ZO CRS stacking operator (1.19) contains eight stacking parameters: $\alpha, \beta, \mathbf{K}_{\text{NIP}}$ and \mathbf{K}_{N} . The theory and the implementation of the 3D ZO CRS stacking operator are minutely discussed in Müller (2003).

1.3.1.3 Common-offset CRS stacking operator

Zhang et al. (2001) presented the common-offset CRS (CO CRS) stacking operator. This general operator has five stacking parameters in the 2D case and thirteen parameters in the 3D case. A more detailed discussion of the 3D CO CRS stacking operator is presented in Section 5.2.

1.3.1.4 CRS stacking operator for converted waves

A 2D CRS-based strategy for converted waves was proposed by Bergler et al. (2002). They used the CO CRS stacking operator that accounts for the asymmetric PS raypath. Based on the example of the 2D synthetic dataset, Bergler et al. (2002) showed that the proposed strategy improves the quality of the stacked section in the presence of noise and extracts reliable kinematic wavefield attributes.

1.3.2 Double-square-root-based stacking operators

Along with reflections, the seismic wavefield contains diffractions. Diffractions appear at the termination of reflectors (e.g., at faults) and at the inhomogeneities of the subsurface. Diffractions allow to obtain correctly migrated images of the subsurface; they are especially important for determining the shape of the salt bodies. Diffractions are used to obtain velocity model (e.g., by means of the NIP-wave tomography Duvencck, 2004; Bauer et al., 2016b) and to analyze the migration velocity (Fomel et al., 2007). Furthermore, processing

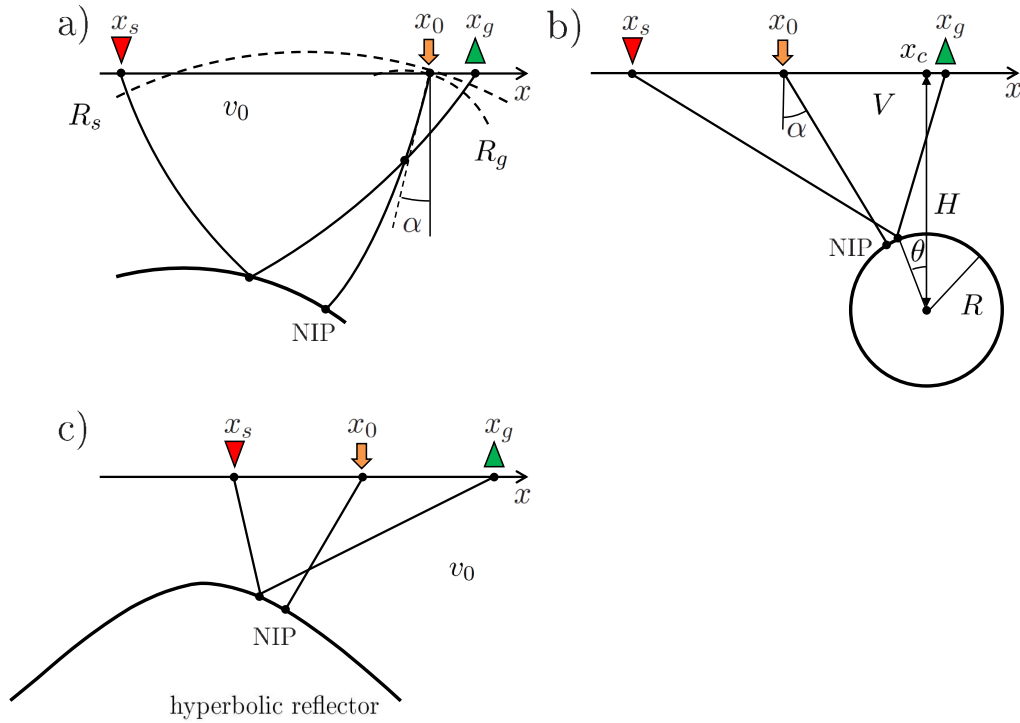


Figure 1.7: (a) In MF, the intersection point of the central ray and the paraxial ray is considered as the virtual seismic source. This virtual seismic source and its corresponding mirror image generate two wavefronts: the source-related wavefront with the radius of curvature R_s and the receiver-related wavefront with the radius of curvature R_g . (b) i-CRS is based on the problem of reflection from the circular reflector in the homogeneous velocity model. (c) n-CRS solves the problem of finding the reflection point from the hyperbolic reflector in the homogeneous velocity model.

of diffractions can lead to the recovery of details smaller than the seismic wavelength (Khaidukov et al., 2004).

The conventional CRS stacking operator, being the second order moveout approximation, cannot properly approximate the traveltimes of the diffraction events. Hence, several alternative stacking operators were proposed to fit both reflection and diffraction events.

1.3.2.1 Multifocusing

Multifocusing (MF) is a stacking technique proposed by Gelchinsky et al. (1999). It generalizes the ideas of the homeomorphic imaging (Gelchinsky, 1989). The MF moveout

approximation is a double-square-root formula, that is traditionally expressed in terms of the source and the receiver displacements:

$$\Delta x_s = x_s - x_0, \quad \Delta x_g = x_g - x_0. \quad (1.22)$$

The MF moveout approximation reads:

$$t(\Delta x_s, \Delta x_g) = t_0 + \Delta t_s + \Delta t_g, \quad (1.23)$$

where

$$\Delta t_i = \frac{\sqrt{R_i^2 + 2R_i\Delta x_i \sin \alpha + \Delta x_i^2} - R_i}{v_0}, \quad i = s, g; \quad (1.24)$$

R_s and R_g are the curvature radii of two waveforms (see Figure 1.7a)

$$R_s = \frac{1 + \sigma}{1/R_N + \sigma/R_{\text{NIP}}}, \quad R_g = \frac{1 - \sigma}{1/R_N - \sigma/R_{\text{NIP}}}; \quad (1.25)$$

and σ is so-called focusing parameter:

$$\sigma = \frac{\Delta x_s - \Delta x_g}{\Delta x_s + \Delta x_g + 2(\Delta x_s \Delta x_g / R_{\text{NIP}}) \sin \alpha}. \quad (1.26)$$

MF has a very close relationship with the shifted hyperbola of [de Bazelaire \(1988\)](#). Both methods use the time-shift mechanism to account for the overburden inhomogeneity. For the CMP gather, the MF moveout formula (1.23) reduces to the shifted hyperbola moveout approximation (1.7).

Originally, the focusing parameter (1.26) was derived under the assumption of plane dipping reflector in a homogeneous medium. Hence, the MF moveout approximation (1.23) is often called "planar multifocusing". An alternative formulation, so-called "spherical multifocusing", was proposed by [Landa et al. \(2010\)](#). It is based on the analytical expression for the traveltime of the wave, reflected from the circular reflector in a homogeneous medium.

To my knowledge extension of the MF stacking operator to the 3D case was not presented so far. An attempt to propose the 3D MF stacking operator was made by [Landa et al. \(2010\)](#). They considered spherical reflector in a homogeneous medium. However, this oversimplified model cannot adequately describe existing 3D effects (see Section 2.4 for more details). The 3D MF formula exists only for purely diffracted events, when $R_s = R_g = R_{\text{NIP}}$ (see, e.g., [Berkovitch et al., 2009, 2012](#)). The successful implementation of the 3D MF for the diffraction imaging was reported by [Rauch-Davies et al. \(2013\)](#).

The 2D common-offset MF (2D CO MF) stacking operator was presented by [Berkovitch et al. \(2011\)](#). In the CO case, the moveout is still described by the double-square-root expression. [Berkovitch et al. \(2011\)](#) showed that CO MF allow to enhance strongly non-hyperbolic events and to construct the reliable velocity model by the prestack stereotomography.

1.3.2.2 Implicit CRS

In order to improve the quality of the conventional CRS stack, [Vanelle et al. \(2010\)](#) have revisited the model of [Landa et al. \(2010\)](#) - the circular reflector with the origin at the point (x_c, H) and the radius R in the homogeneous isotropic medium with the velocity V (see Figure 1.7b). In this model, the traveltime of the ray propagated from the source x_s through the arbitrary point on reflector (defined by the angle θ) to the receiver x_g is equal:

$$t(\Delta x_s, \Delta x_g) = t_s + t_g, \quad (1.27)$$

where

$$t_i = \frac{\sqrt{(\Delta x_i - \Delta x_c - R \sin \theta)^2 + (H - R \cos \theta)^2}}{V}, \quad \Delta x_c = x_c - x_0, \quad i = s, g. \quad (1.28)$$

According to Fermat's principle, the ray takes the path that minimizes the traveltime, i.e., the condition $\frac{\partial t}{\partial \theta} = 0$ must fulfill. This condition leads to the implicit equation for the angle θ :

$$\tan \theta = \frac{m - \Delta x_c}{H} + \frac{h}{H} \frac{t_s - t_g}{t_s + t_g}. \quad (1.29)$$

The last equation may be solved iteratively with the initial value of θ corresponding to the NIP (see [Vanelle et al., 2010](#)).

In order to extend this model-based approach to the inhomogeneous medium, [Schwarz \(2011\)](#) expanded the square roots of (1.27) into the Taylor series and matched the coefficients with the respective counterparts in the parabolic CRS stacking operator (1.15). The obtained system of equations has a unique solution:

$$\begin{aligned} V &= \frac{v_{\text{NMO}}}{\sqrt{1 + (v_{\text{NMO}}^2/v_0^2) \sin^2 \alpha}}, \\ x_c &= x_0 - \frac{R_N \sin \alpha}{\cos^2 \alpha (1 + [v_{\text{NMO}}^2/v_0^2] \sin^2 \alpha)}, \\ H &= \frac{v_0 R_N}{v_{\text{NMO}} \cos^2 \alpha (1 + [v_{\text{NMO}}^2/v_0^2] \sin^2 \alpha)}, \\ R &= \frac{(v_0 R_N / v_{\text{NMO}} \cos^2 \alpha) - (v_{\text{NMO}} t_0 / 2)}{\sqrt{1 + (v_{\text{NMO}}^2/v_0^2) \sin^2 \alpha}}, \end{aligned} \quad (1.30)$$

where the NMO velocity is equal to

$$v_{\text{NMO}} = \sqrt{\frac{2v_0 R_{\text{NIP}}}{t_0 \cos^2 \alpha}}. \quad (1.31)$$

The traveltime formula (1.27) with the coefficients (1.30) was called the implicit CRS (i-CRS) stacking operator.

[Schwarz et al. \(2014\)](#) summarized the method and compared i-CRS with the conventional CRS and MF. They found that i-CRS provides higher accuracy than the MF method,

especially in the presence of strong inhomogeneity. In order to explain this result, Schwarz et al. (2015) investigated the mechanisms by which MF and i-CRS account for inhomogeneity of the overburden: while MF uses the time-shift mechanism, i-CRS inherits the velocity-shift mechanism, typical for CRS. Schwarz et al. (2015) also proposed a recipe how to transform time-shifts to velocity-shifts and vice versa. With this recipe, one can obtain the time-shifted version of the i-CRS operator and the velocity-shifted version of MF. Schwarz et al. (2015) concluded that i-CRS and MF "are essentially equivalent, when the same auxiliary medium for both operators is considered".

Vanelle et al. (2012a) proposed the 2D i-CRS stacking operator for converted waves (2D i-CRS-PS, see Section 4.2.4 for more details). However, extension of the i-CRS method to the 3D case and to the common-offset case was not presented so far.

1.3.2.3 Non-hyperbolic CRS

Another simple model, that consists of the hyperbolic reflector in the constant-velocity medium (see Figure 1.7c), was analyzed by Fomel and Stovas (2010). They derived an analytical expression for the reflection traveltime in this simple model. Based on this analytical expression, Fomel and Kazinnik (2013) proposed the non-hyperbolic common reflection surface (n-CRS) stacking operator:

$$t(m, h) = \sqrt{\frac{F(m) + \chi h^2 + \sqrt{F(m-h)F(m+h)}}{2}}, \quad (1.32)$$

where

$$F(m) = (t_0 + wm)^2 + 2t_0Nm^2, \quad (1.33)$$

$$\chi = 2t_0(2M - N) + w^2, \quad (1.34)$$

and w , M , N are the CRS parameters (1.17).

Obviously, the n-CRS stacking operator is mathematically more complicated than the MF and i-CRS formulas. In order to better understand the structure of the n-CRS formula (1.32), I propose the following reformulation (see Appendix C.1):

$$t(m, h) = \sqrt{\left[\underbrace{\frac{1}{2}\sqrt{F(m-h)}}_{t_s} + \underbrace{\frac{1}{2}\sqrt{F(m+h)}}_{t_g} \right]^2 + \underbrace{2t_0(M-N)h^2}_{\Delta t_{sg}}}. \quad (1.35)$$

In the case of diffractions, coefficients M and N are equal and n-CRS transforms to the purely DSR formula.

Fomel and Kazinnik (2013) presented the formal extension of the n-CRS stacking operator to the 3D case (3D n-CRS, see Appendix C.2). However, they could not find a geometrical interpretation of the obtained traveltime approximation.

Table 1.1: Evolution of stacking operators

Stack	Stacking operator	Extensions
CMP	$t = \sqrt{f_{\text{NMO}}(t_0, h)}$	3D, PS, CO
CRS	$t = \sqrt{f_{\text{CRS}}(t_0, h, m)}$	3D, PS, CO
MF	$t = t_0 + \underbrace{\sqrt{f_{\text{MF}}^s(h, m)}}_{\Delta t_s} + \underbrace{\sqrt{f_{\text{MF}}^g(h, m)}}_{\Delta t_g}$	
i-CRS	$t = \underbrace{\sqrt{f_{\text{iCRS}}^s(t_0, h, m)}}_{t_s} + \underbrace{\sqrt{f_{\text{iCRS}}^g(t_0, h, m)}}_{t_g}$?
n-CRS	$t = \sqrt{\left[\underbrace{\sqrt{f_{\text{nCRS}}^s(t_0, h, m)}}_{t_s} + \underbrace{\sqrt{f_{\text{nCRS}}^g(t_0, h, m)}}_{t_g} \right]^2 + \underbrace{f_{\text{nCRS}}^{sg}(t_0, h)}_{\Delta t_{sg}}}$	

Walda et al. (2016) made a fair comparison of the CRS, MF, i-CRS and n-CRS stacking operators. In order to reveal the full potential of the DSR-based stacking operators, they carefully accounted for the conflicting dips problem and used a global optimization scheme to estimate the wavefield attributes. As well they compared stacking operators in the same (time-shifted or velocity-shifted) domain. Based on the marine field data, they found that all DSR-based stacking operators give superior results compared to the conventional CRS. Also they did not observe significant differences between the DSR-based stacking operators. A comparison of the computational efficiency showed that the most efficient DSR-based stacking operator is the n-CRS with only 5% increase in the computational time compared to the conventional CRS.

1.4 Conclusions

The stacking theory has come a long way from the CMP stack over the multidimensional CRS stack to the double-square-root-based MF, i-CRS and n-CRS stacks. Over the years, stacking operators have evolved and become more and more complicated (see Table 1.1). For the purpose of simplicity, the new stacking techniques are usually proposed for the simplest 2D zero-offset case. Later they are extended to three important cases: the 3D case, the case of converted waves (PS) and the case of common-offset geometry (CO).

The classical CMP stack and the CRS stack have extensions for all these special cases. However, the extension of the MF/i-CRS/n-CRS stacking operators to the 3D/PS/CO cases have not been fully understood yet. Existing in the literature extensions (2D CO MF, 2D i-CRS-PS and 3D n-CRS) still remain a room for further studies. To date a number of interesting questions are still open: how to derive the 3D n-CRS stacking operator, how to extend the 2D i-CRS/MF stacking operators to the 3D case, how to construct the n-CRS

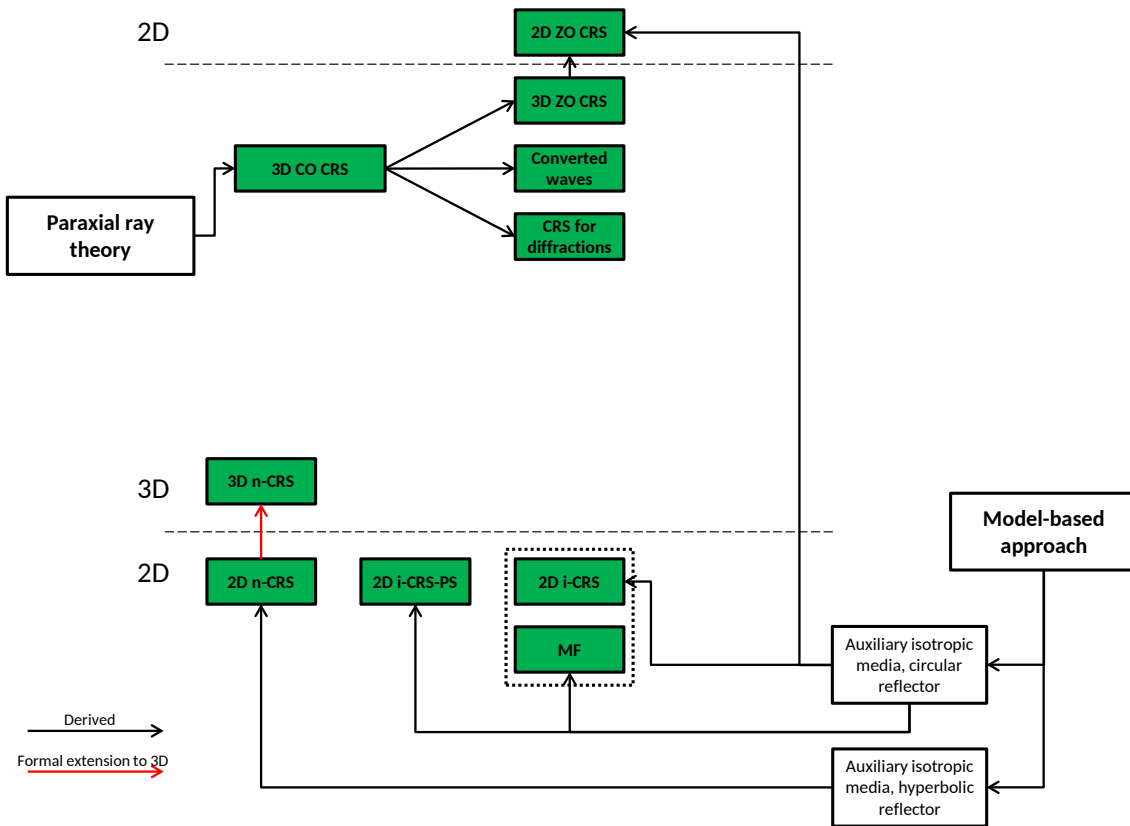


Figure 1.8: Classification of the multidimensional stacking operators. The paraxial ray theory is the origin for the 3D CO CRS stacking operator which may be used for stacking of converted waves. The model-based approach is used for the derivation of the DSR-based stacking operators. The most popular model - the spherical reflector in the homogeneous medium - leads to the MF and i-CRS stacking operators. The dashed line indicates that MF and i-CRS represent almost the same stacking operator formulated in different domains.

stacking operator for the case of converted waves?

Another important issue is the origin of the stacking operators. While the CRS stacking operator is based on the paraxial ray theory, all DSR-based stacking operators are derived from the model-based approach (see Figure 1.8). However, the 2D ZO CRS stacking operator can also be derived from the model-based approach of Höcht et al. (1999). The question naturally arises whether it is possible to derive the DSR-based stacking operators from the paraxial ray theory.

In the next four chapters, I will try to find the answers to these questions.

Chapter 2

Theory of 3D DSR-based stacking operators

The geometrical approach is usually used for the derivation of the 2D DSR-based stacking operators. The key element of the derivation is a simplified model: an analytical reflector in a homogeneous isotropic medium (auxiliary medium). The straightforward extension of this approach to the 3D case does not lead to good results since the wavefronts have complicated shape in the 3D case.

In this chapter, I propose the 3D simplified model which consists of the auxiliary anisotropic medium and the specially oriented analytical reflector. Based on this model, I extend the existing DSR-based stacking operators to the 3D case.

2.1 Introduction

Stacking of seismic traces is a basic step in the seismic processing workflow (Yilmaz, 2001). It represents a convenient and efficient way to obtain a simulated zero-offset (ZO) volume and to extract surface-based kinematic wavefield attributes which may be used in the subsequent imaging steps. The quality of the ZO volume and the wavefield attributes significantly depends on the chosen stacking operator. The double-square-root-based (DSR-based) stacking operators produce images of the subsurface superior than the one obtained by the conventional common-reflection-surface (CRS) stacking operator (Landa, 2007; Schwarz et al., 2014). A variety of DSR-based stacking operators exists in the 2D case. The most common are Multifocusing (MF) (Gelchinsky et al., 1999; Landa et al., 1999; Tygel et al., 1999), non-hyperbolic CRS (n-CRS) (Fomel and Kazinnik, 2013) and implicit CRS (i-CRS) (Vanelle et al., 2010; Schwarz, 2011).

Nowadays, the 3D seismic surveys have become a standard exploration and exploitation tool (Vermeer, 2002). The 3D seismic surveys allow to obtain a true and precise image of

the subsurface (French, 1974). While the 3D CRS stacking operator exists in the literature (see Müller, 2003), the 3D versions of the DSR-based stacking operators (except the formal extension of n-CRS) were not presented so far. Hence, it is important to extend the DSR-based stacking operators to the 3D case.

The geometrical (model-based) approach is commonly used for the derivation of the DSR-based stacking operators. The derivation is usually based on a simplified model of the subsurface: an analytical reflector in an auxiliary constant-velocity medium. The simplified model is related to "reality" (a curved reflector below an inhomogeneous overburden) through the two hypothetical experiments providing two eigen-wavefronts (Hubral, 1983). This allows to obtain the DSR-based traveltime approximations with the same wavefield attributes used in the conventional CRS stacking operator.

This chapter re-examines the geometrical approach in the 2D case and proposes its extension to the 3D case in order to obtain the 3D DSR-based stacking operators. The chapter has the following structure. Section (2.2) gives a statement of the problem and explains the main ideas behind the derivation of the 2D DSR-based stacking operators. The next three sections introduce the components of the 3D simplified model: the special ray-centered coordinate system (Section 2.3), the auxiliary anisotropic medium (Section 2.4) and the curved reflector (Section 2.5). The 3D simplified model (Section 2.6) depends only on the traveltime of the central ray, the near-surface velocity and the kinematic wavefield attributes. In the 3D simplified model, the traveltime of the reflected wave can be presented either by the implicit DSR formula, similar to i-CRS (Section 2.7), or by the approximate explicit DSR formula, similar to n-CRS (Section 2.8). Final Section (2.9) concludes the results of this chapter and highlights the links between the obtained operators.

2.2 Statement of the problem

In the reflection seismic experiment, the seismic wave, emitted from the source, propagates in the inhomogeneous subsurface. This wave reflects from the inhomogeneities in the subsurface, returns back to the measurement surface and is recorded by receivers. In the 2D case, the sources and the receivers are located on the seismic profile. The central ray originates from the central (imaging) point x_0 , reflects at the normal-incidence-point (NIP) and returns back to x_0 with the traveltime t_0 (see Figure 2.1a). The stacking operators describe the traveltime t of the paraxial ray, whose source position x_s and receiver position x_g are located in the vicinity of the central point x_0 .

The derivation of the 2D DSR-based stacking operators requires several assumptions. Both i-CRS and n-CRS as well as MF utilize the concept of straight rays and locally approximate the wavefront elements by circles. Hence, it is usual to replace the complex inhomogeneous overburden by the homogeneous medium (so-called auxiliary medium). It is also common to approximate the reflector by an algebraic curve. For example, the circular reflector is used in the derivation of i-CRS, and n-CRS is based on the reflection from the specially oriented hyperbola. The auxiliary medium and the analytical reflector form a simplified

model, appealing for the geometrical interpretation (see Figure 2.1b).

As mentioned in the previous chapter, the 2D stacking operators can be formulated either for the “optical” or for the “efficient” auxiliary medium (see Sections 1.2.2 and 1.3.2.2). In fact, the difference between these two auxiliary media is only in the value of the velocity, which is either equal to the near-surface velocity v_0 (in the optical medium) or to the effective velocity (in the effective medium). Since formulation in the optical domain is more intuitive and leads to considerably simpler formulas, in the following I will use the optical auxiliary medium.

The relationship between the inhomogeneous medium with the curved reflector and the simplified model is established upon consideration of two hypothetical experiments: the normal-incidence-point (NIP) experiment and the normal experiment.

In the NIP experiment, a fictitious source \mathcal{S} is placed at the reflection point of the central ray (NIP). The source \mathcal{S} generates the wavefront with the radius of curvature R_{NIP} at the central point (see Figure 2.1c). The circular approximation of the wavefront is applicable in the vicinity of the central point. In the optical auxiliary medium of constant velocity v_0 , an identical wavefront may be generated by an image source \mathcal{S}^* located at the center of curvature of the NIP wavefront. The position of the image source \mathcal{S}^* is determined by the emergence angle of the central ray α and the radius of curvature R_{NIP} . Note that the two-way traveltimes along the central ray in the optical auxiliary medium

$$t_p = \frac{2R_{\text{NIP}}}{v_0} \quad (2.1)$$

is generally not equal to the two-way traveltimes t_0 in the inhomogeneous medium.

In the normal experiment, the fictitious exploding reflector is considered (see Figure 2.1d). Similarly to the NIP experiment, the wavefront of the normal wave can be approximated by the circular wavefront with the radius of curvature R_N at the central point. It is apparent from Figure 2.1d that the identical wavefront is generated by the circular reflector with the origin at the center of curvature of the normal wavefront \mathcal{O}^* and the radius R :

$$R = R_N - R_{\text{NIP}}. \quad (2.2)$$

Thus, the simplified model is defined by the near-surface velocity v_0 and the surface-based wavefield attributes: the emergence angle of the central ray α , and the curvatures of the fundamental waves R_{NIP} and R_N .

In the simplified model, the traveltimes of the ray from the source at x_s to the circular reflector ($x_{ref}(\vartheta), z_{ref}(\vartheta)$) parameterized by the variable ϑ to the receiver at x_g is equal:

$$t(\vartheta) = \frac{\sqrt{(x_s - x_{ref}(\vartheta))^2 + z_{ref}^2(\vartheta)}}{v_0} + \frac{\sqrt{(x_g - x_{ref}(\vartheta))^2 + z_{ref}^2(\vartheta)}}{v_0}. \quad (2.3)$$

According to Fermat’s principle, the reflected ray prefers the path, which minimizes the traveltimes $t(\vartheta)$. Hence, the value of the variable $\vartheta = \vartheta_r$ defining the reflection point

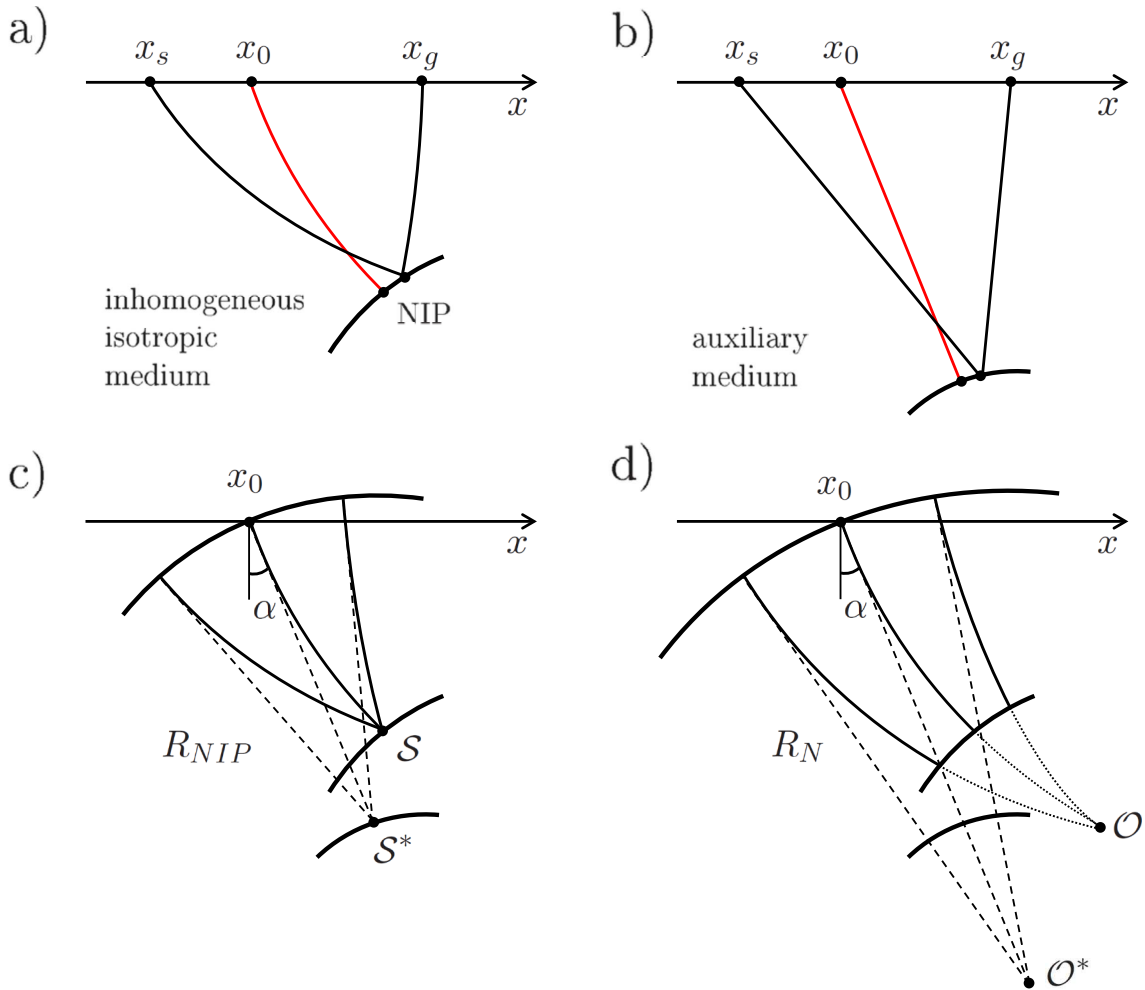


Figure 2.1: Illustration of the 2D seismic reflection experiment (a). The central ray (red) and the paraxial ray (black) propagate in the inhomogeneous isotropic medium. In order to find the traveltime of the paraxial ray, the inhomogeneous medium and the curved reflector are simplified by the constant-velocity medium and the circular reflector (b). The parameters of such simplified model are linked with the curvatures of the NIP (c) and normal (d) waves.

coordinates (x_r, z_r) can be found by minimizing the traveltime $t(\vartheta)$:

$$\frac{\partial t}{\partial \vartheta} = 0, \quad \rightarrow \quad \vartheta = \mathcal{F}(\vartheta, v_0, x_s, x_g, x_0, \alpha, R_{\text{NIP}}, R_N). \quad (2.4)$$

The resulting implicit equation can be iteratively solved to obtain ϑ_r . Substitution of ϑ_r into the equation (2.3) yields the traveltime of the reflected ray in the simplified model.

Finally, the traveltime of the reflected wave in the inhomogeneous medium is obtained after subtraction of the time shift $t_p - t_0$ from the traveltime of the reflected ray in the simplified model:

$$t = \frac{\sqrt{(x_s - x_r)^2 + z_r^2}}{v_0} + \frac{\sqrt{(x_g - x_r)^2 + z_r^2}}{v_0} - (t_p - t_0). \quad (2.5)$$

The above strategy reproduces the derivation of the time-shifted version of the 2D i-CRS stacking operator (Schwarz, 2011).

The objective of this chapter is to apply the similar strategy in the 3D case in order to find the 3D DSR-based stacking operators. This will obviously require:

1. the image source \mathcal{S}^* in the 3D auxiliary medium, defined by the curvature of the NIP wavefront (similar to 2.1);
2. the link between the curvature of the reflector and the curvatures of the NIP and normal wavefronts in the 3D case (similar to 2.2);
3. the expression for the traveltime of the reflected ray (similar to 2.3);
4. the system of equations defining the reflection point coordinates (similar to 2.4).

Moreover, the 3D DSR-based stacking operators have to be compatible with the conventional 3D CRS stacking operator (1.19) and have to use the same wavefield attributes (1.20) as the conventional 3D CRS.

2.3 Coordinate system

To provide a mathematical formalism of the problem, I establish two coordinate systems: the general Cartesian coordinate system \mathcal{L} related to the measurement surface and the special ray-centered coordinate system \mathcal{L}' related to the central ray (see Figure 2.2a).

The general Cartesian coordinate system \mathcal{L} is chosen so that the seismic source $\hat{\mathbf{x}}_s$, the receiver $\hat{\mathbf{x}}_g$ and the central point $\hat{\mathbf{x}}_0$ are located in the plane $z = 0$. The positive z -axis points downwards, thereby z may be referred to as "depth".

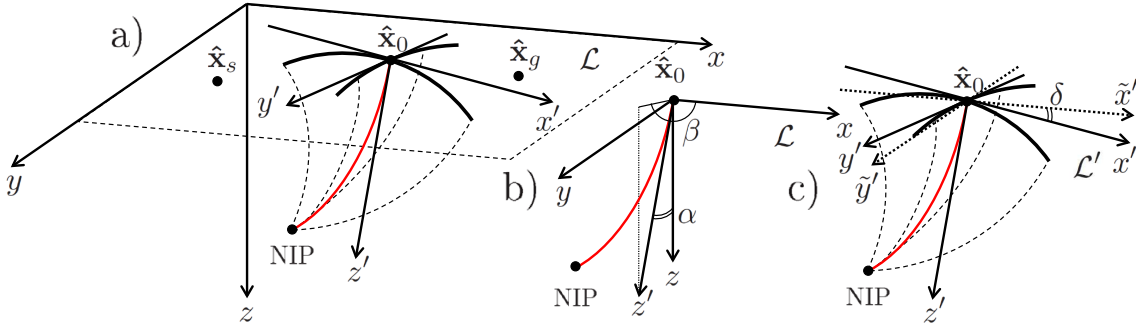


Figure 2.2: Seismic measurements are related to the general Cartesian coordinate system \mathcal{L} (a). However, the derivation of the 3D DSR-based stacking operators requires the special ray-centered coordinate system \mathcal{L}' . The origin of the system \mathcal{L}' coincides with the central point $\hat{\mathbf{x}}_0$. It's z' -axis is tangential to the central ray and the x' and y' -axes align the principal directions of curvature of the NIP wavefront. The direction of z' -axis is defined by the emergence angles α and β of the central ray (b). In the standard ray-centered coordinate system $\tilde{\mathcal{L}}$, \tilde{x}' and \tilde{y}' -axes do not coincide with the principal directions of the NIP wavefront. Hence, the additional rotation for the angle δ is performed (c).

The system \mathcal{L}' is a special ray-centered coordinate system whose x' and y' -axes coincide with the principal directions of curvature of the NIP wavefront. Like the standard ray-centered coordinate system, the system \mathcal{L}' originates at the central point $\hat{\mathbf{x}}_0$, and it's z' -axis is tangential to the central ray at $\hat{\mathbf{x}}_0$.

The relationship between the general Cartesian coordinates $\hat{\mathbf{x}}$ and the special ray-centered coordinates $\hat{\mathbf{x}}'$ is given by equation:

$$\hat{\mathbf{x}}' = \hat{\mathbf{R}}_z^T(\delta) \underbrace{\hat{\mathbf{R}}_y^T(\alpha) \hat{\mathbf{R}}_z^T(\beta)}_{\hat{\mathbf{R}}^T} (\hat{\mathbf{x}} - \hat{\mathbf{x}}_0). \quad (2.6)$$

In this equation, α and β are the polar and azimuthal angles of the central ray, and δ is the angle between the principal curvature direction and the x -axis of the standard ray-centered coordinate system (see Figure 2.2b). The matrices $\hat{\mathbf{R}}_y$ and $\hat{\mathbf{R}}_z$ are the basic rotation matrices:

$$\hat{\mathbf{R}}_y(\theta) = \begin{pmatrix} \cos \theta & 0 & \sin \theta \\ 0 & 1 & 0 \\ -\sin \theta & 0 & \cos \theta \end{pmatrix}, \quad \hat{\mathbf{R}}_z(\theta) = \begin{pmatrix} \cos \theta & -\sin \theta & 0 \\ \sin \theta & \cos \theta & 0 \\ 0 & 0 & 1 \end{pmatrix}. \quad (2.7)$$

The matrix $\hat{\mathbf{R}}^T \equiv \hat{\mathbf{R}}_y^T(\alpha) \hat{\mathbf{R}}_z^T(\beta)$ accounts for the transformation from the general Cartesian to the standard ray-centered coordinate system. The matrix $\hat{\mathbf{R}}_z^T(\delta)$ makes an additional rotation about z' -axis to align x' and y' -axes with the principal directions of curvature of the NIP wavefront.

The obvious advantage of the coordinate system \mathcal{L}' over the standard ray-centered system

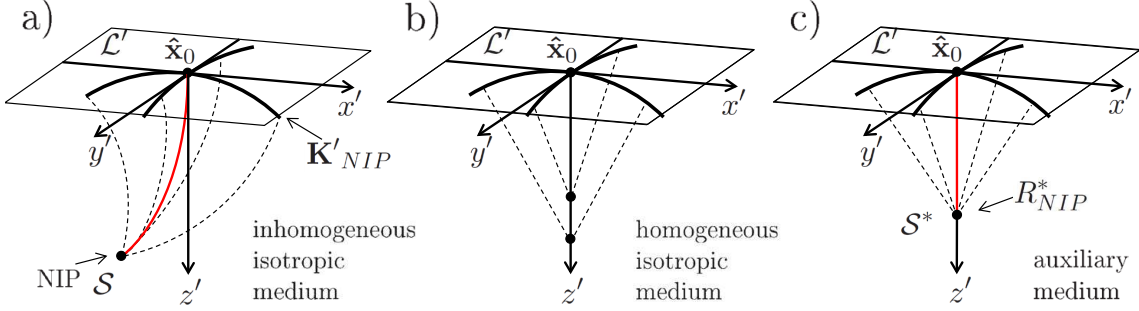


Figure 2.3: Illustration of the NIP experiment in the 3D case. The fictitious source \mathcal{S} in the inhomogeneous medium generates the wavefront with the curvature \mathbf{K}'_{NIP} (a). In the case of the auxiliary *isotropic* medium (b), the NIP wavefront does not "focus" in one point. Consideration of the auxiliary *anisotropic* medium (c) overcomes this problem.

is that in the \mathcal{L}' system the matrix of curvature of the NIP wave \mathbf{K}'_{NIP} is diagonal:

$$\mathbf{K}'_{NIP} = \begin{pmatrix} k'_{NIP}{}^{11} & 0 \\ 0 & k'_{NIP}{}^{22} \end{pmatrix}. \quad (2.8)$$

2.4 Auxiliary anisotropic medium

As discussed before, all DSR-based stacking operators describe the moveout in the auxiliary medium of constant velocity. It is also important to note that the 2D auxiliary medium is not only homogeneous but also isotropic, i.e. the velocity is direction-independent.

In the 2D case, the circular wavefront approximation is valid, because the arbitrary wavefront is locally defined by one curvature. However, in the 3D case, an arbitrary wavefront has two principal curvatures and, hence, could not be accurately approximated by the spherical wavefront. In the 3D case, the homogeneous isotropic medium does not "focus" the arbitrary wavefront (see Figure 2.3b). Thus, I propose to consider a homogeneous anisotropic medium. In the homogeneous anisotropic medium, the wavefronts have a complicated shape, since the velocity varies with the direction. Hence it is possible to find the homogeneous anisotropic medium that "focus" the wavefront of the arbitrary curvature in one point (see Figure 2.3c).

The wavefront propagation in a general homogeneous anisotropic medium is governed by 21 density normalized elastic parameters. However, the number of independent parameters may be significantly reduced when the wavefronts with the certain symmetry properties are required. In the system \mathcal{L}' , the local quadratic approximation of the arbitrary wavefront has two orthogonal symmetry planes: $x' = 0$ and $y' = 0$ (see Figures 2.3a,c). Since the wavefront approximation is only of interest in the half-space $z' > 0$, there is an additional symmetry plane $z' = 0$. Given the above mentioned symmetries, the general anisotropy

degenerates to the orthorhombic anisotropy.

The orthorhombic anisotropy media is defined by 9 density normalized elastic parameters. However, the propagation of quasi-compressional (qP) waves in the degenerate orthorhombic (ellipsoidal) medium is governed by only three density normalized elastic parameters. The group velocity of qP-waves in the weakly anisotropic ellipsoidal medium is equal to (Daley and Krebs, 2005, p. 5 eq. 21):

$$\frac{1}{\zeta^2(\Theta, \Phi)} = \frac{\sin^2 \Theta \cos^2 \Phi}{A_{11}} + \frac{\sin^2 \Theta \sin^2 \Phi}{A_{22}} + \frac{\cos^2 \Theta}{A_{33}}. \quad (2.9)$$

Here Θ and Φ are the group polar and azimuthal angles defining the direction of the ray. Density normalized elastic parameters A_{11} , A_{22} and A_{33} define the group velocity in x' , y' and z' directions, respectively.

In order to investigate the link between the density normalized elastic parameters and the principal curvatures of the NIP wavefront, I consider the NIP experiment. In the NIP experiment the fictitious source \mathcal{S} is placed at the reflection point of the central ray (see Figure 2.3a). The wavefront generated by the source \mathcal{S} arrives at the central point $\hat{\mathbf{x}}'_0$ at the time $\frac{t_0}{2}$ with the curvature \mathbf{K}'_{NIP} . The identical wavefront may be generated by the image source \mathcal{S}^* at the point $(0, 0, R^*_{\text{NIP}})$ in the auxiliary anisotropic medium.

The depth of the image source R^*_{NIP} and the parameters of the auxiliary anisotropic medium A_{11} , A_{22} , A_{33} are uniquely determined from the condition that the traveltimes, the slowness vector and the curvature of the NIP wavefront at the central point $\hat{\mathbf{x}}'_0$ are the same both in the inhomogeneous medium and in the auxiliary medium. Indeed:

- from the condition of the slowness equality, the group velocity along z' -axis in the auxiliary medium is equal to the velocity v_0 at the central point in the inhomogeneous medium:

$$A_{33} = v_0^2; \quad (2.10)$$

- from the condition of the traveltimes equality, the depth of the image source \mathcal{S}^* is equal:

$$R^*_{\text{NIP}} = \frac{t_0 v_0}{2}; \quad (2.11)$$

- from the condition of the curvature equality, the parameters A_{11} , A_{22} are equal (see Appendix A.2 for details):

$$\frac{1}{A_{11}} = \frac{t_0}{2v_0} k'^{11}_{\text{NIP}}, \quad \frac{1}{A_{22}} = \frac{t_0}{2v_0} k'^{22}_{\text{NIP}}. \quad (2.12)$$

Hence, in the 3D case, the complex inhomogeneous overburden may be replaced by the auxiliary anisotropic medium with parameters:

$$\frac{1}{A_{11}} = \frac{t_0}{2v_0} k'^{11}_{\text{NIP}}, \quad \frac{1}{A_{22}} = \frac{t_0}{2v_0} k'^{22}_{\text{NIP}}, \quad \frac{1}{A_{33}} = \frac{1}{v_0^2}. \quad (2.13)$$

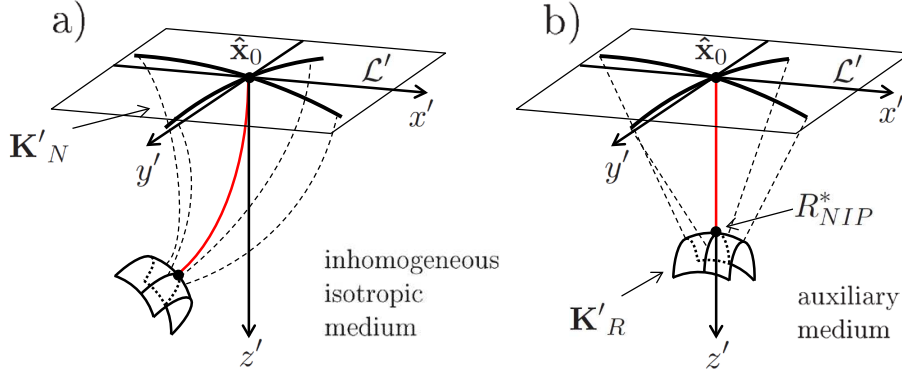


Figure 2.4: Illustration of the normal experiment in the 3D case. The exploding reflector in the inhomogeneous medium generates the wavefront with the curvature \mathbf{K}'_N (a). The similar wavefront may be generated by the analytical reflector with the curvature \mathbf{K}'_R in the auxiliary medium.

The parameters (2.13) depend on the traveltime of the central ray t_0 , the near-surface velocity v_0 and the curvature of the NIP wavefront. Hence they are fixed for a given central ray. Note that, unlike the 2D case, the traveltimes along the central ray coincide in the auxiliary anisotropic medium and in the inhomogeneous medium.

2.5 Curvature of reflector

In the 2D case, the arbitrary reflector can be locally approximated by an analytic curve in the vicinity of the NIP. For example, the circular reflector is used in the derivation of the i-CRS formula, and the n-CRS formula is based on the reflection from the specially oriented hyperbola. These simplifications are possible, because the front of the hypothetical normal wave has one curvature in the 2D case. However, in the 3D case, both the reflector and the normal wavefront are described by 2×2 symmetric curvature matrices (see Figure 2.4a). As shown in the previous section, the inhomogeneous medium may be replaced by the auxiliary anisotropic medium with parameters depending on the curvature of the NIP wavefront. The aim of this section is to find the reflector that generates the normal wavefront with the desired curvature in the auxiliary medium.

When the inhomogeneous overburden is replaced by the auxiliary medium, the central ray becomes the straight line coinciding with the z' -axis and the NIP is located at the depth R^*_{NIP} (see Figure 2.4b). Like in the inhomogeneous isotropic medium, in the auxiliary medium the reflector passes through the NIP and is perpendicular to the central ray at the NIP. The curvature of the reflector at the NIP is determined by the curvature matrix \mathbf{K}'_R .

In the 3D case, there are many surfaces with the curvature \mathbf{K}'_R at the apex. For example,

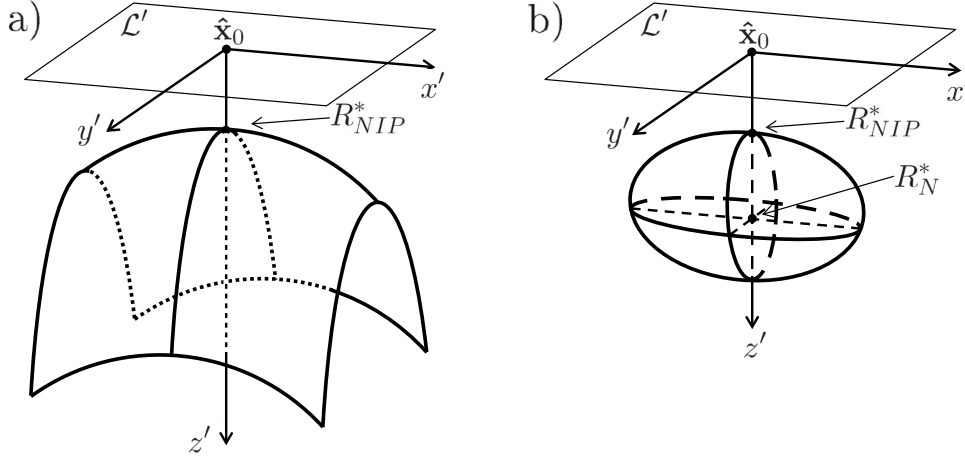


Figure 2.5: Two different ways to approximate the reflection surface: (a) by the paraboloid, and (b) by the ellipsoid. Both reflectors have the same curvature \mathbf{K}'_R at the apex point R_{NIP}^* .

the reflector can be approximated by the paraboloid (see Figure 2.5a):

$$f(\mathbf{x}') = R_{NIP}^* + \frac{1}{2} \mathbf{x}'^T \mathbf{K}'_R \mathbf{x}', \quad (2.14)$$

or by the ellipsoid (see Figure 2.5b and Appendix B.1). Although the ellipsoidal reflector is a restricted case (both principal curvatures have positive signs), this type of reflector is of special interest because of the ability to fit point diffractors. Despite the actual form of the reflector, the curvature of the normal wave depends only on the curvature of the reflector at the NIP. In order to find the relationship between curvatures \mathbf{K}'_R and \mathbf{K}'_N , I consider the normal experiment.

In the normal experiment (see Figure 2.4b), the wavefront, originated from the reflector, propagates through the auxiliary medium and arrives at the central point $\hat{\mathbf{x}}_0$ with the curvature \mathbf{K}'_N . Suppose that the reflector is defined by the function f of the lateral coordinates (e.g., by the equation 2.14). Then, it is possible to compute a unit normal vector at each point on the reflector. The normal vector, being also normal to the wavefront, defines the direction of the phase velocity propagation. The directions of the group and phase velocity propagation generally do not coincide in an anisotropic media and have a complicated relation. However, in the auxiliary (ellipsoidal) anisotropic medium, there is an explicit relation between the group and phase angles (see e.g. Daley and Krebs, 2005). The group angles define the direction and the value of the group velocity ζ according to the equation (2.9).

Therefore, for each point on the reflector $\hat{\mathbf{x}}'_{ref}$ it is possible to construct the normal ray. This ray crosses the surface $z' = 0$ at the intersection point $\hat{\mathbf{x}}'_{int}$:

$$\begin{pmatrix} x'_{int} \\ y'_{int} \\ 0 \end{pmatrix} = \begin{pmatrix} x'_{ref} \\ y'_{ref} \\ f(\mathbf{x}'_{ref}) \end{pmatrix} + t \begin{pmatrix} \zeta_1(\mathbf{x}'_{ref}) \\ \zeta_2(\mathbf{x}'_{ref}) \\ \zeta_3(\mathbf{x}'_{ref}) \end{pmatrix}. \quad (2.15)$$

The z' -component of this three-component equation gives the traveltime to the intersection point as a function of \mathbf{x}'_{ref} :

$$t = -\frac{f(\mathbf{x}'_{ref})}{\zeta_3(\mathbf{x}'_{ref})}. \quad (2.16)$$

Substitution of (2.16) into the x' and y' -components of the equation (2.15) yields the dependence of the intersection point \mathbf{x}'_{int} on the reflector point \mathbf{x}'_{ref} . In the vicinity of the central ray, this dependence can be linearized, and the inverse relation can be established (see Appendix A.3 for details):

$$\mathbf{x}'_{ref} \approx \left[\mathbf{I} + \mathbf{K}'_{NIP}{}^{-1} \mathbf{K}'_R \right]^{-1} \mathbf{x}'_{int}. \quad (2.17)$$

With the last relation it is possible to find the traveltime of the normal wave as a function of \mathbf{x}'_{int} (see Appendix A.3 for details):

$$t^2(\mathbf{x}'_{int}) = \frac{t_0^2}{4} + \frac{t_0}{2v_0} \mathbf{x}'_{int}{}^T \left[\mathbf{K}'_R{}^{-1} + \mathbf{K}'_{NIP}{}^{-1} \right]^{-1} \mathbf{x}'_{int}. \quad (2.18)$$

The comparison of this traveltime with the hyperbolic expression (see Appendix A.1)

$$t^2(\mathbf{x}') = \frac{t_0^2}{4} + \frac{t_0}{2v_0} \mathbf{x}'^T \mathbf{K}'_N \mathbf{x}' \quad (2.19)$$

gives the desired link between the curvatures:

$$\mathbf{K}'_N{}^{-1} = \mathbf{K}'_R{}^{-1} + \mathbf{K}'_{NIP}{}^{-1}. \quad (2.20)$$

Thus, in the 3D auxiliary anisotropic medium, the reflector with the curvature

$$\mathbf{K}'_R = \left[\mathbf{K}'_N{}^{-1} - \mathbf{K}'_{NIP}{}^{-1} \right]^{-1} \quad (2.21)$$

generates the normal wavefront with the curvature \mathbf{K}'_N . Another important result follows immediately from (2.17) and (2.21):

$$\mathbf{x}'_{ref} \approx \left[\mathbf{I} - \mathbf{K}'_{NIP}{}^{-1} \mathbf{K}'_N \right] \mathbf{x}'_{int}. \quad (2.22)$$

This means that the approximate position of the reflection point may be determined in terms of the surface-based kinematic wavefield attributes.

2.6 3D simplified model

In summary, the inhomogeneous medium with the curved reflector may be replaced by the auxiliary anisotropic medium with the analytical reflector of curvature \mathbf{K}'_R (see Figure 2.6). The analytical reflector (2.21) and the auxiliary medium (2.13) in the special ray-centered coordinate system (2.6) form the simplified model. The simplified model depends on the

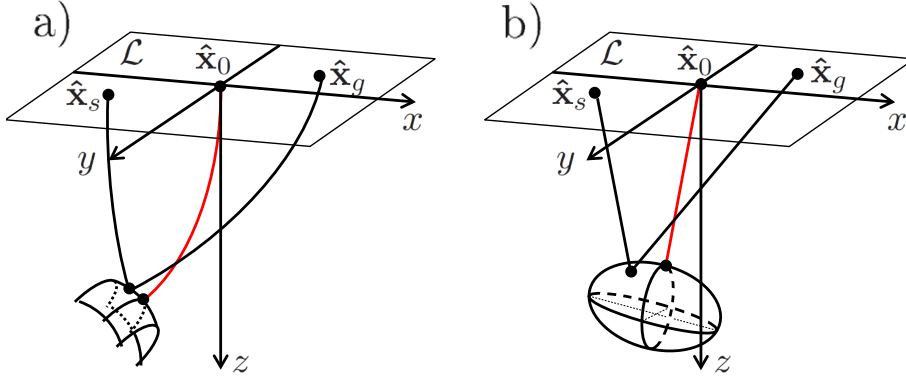


Figure 2.6: Similar to the 2D case, in the 3D case, the inhomogeneous overburden with the curved reflector (a) can be replaced by the simplified model (b). In the simplified model the rays are straight lines, and the reflector has a simple shape. Hence, the traveltimes of the paraxial ray can be found based on the geometrical relations.

traveltimes of the central ray, the near-surface velocity and the surface-based kinematic wavefield attributes.

By definition, the simplified model satisfies the hypothetical NIP and normal experiments. Since the NIP and normal waves are the eigen-waves (Hubral, 1983), the arbitrary reflected wave, in some sense, can be represented by the superposition of these eigen-waves. Thus, the simplified model may be used to predict the traveltimes of the paraxial ray.

2.7 Implicit stacking operator (3D i-CRS)

As discussed previously, it is possible to replace the curved reflector and the inhomogeneous overburden with a simplified model. The surface-based kinematic wavefield attributes define the simplified model that consists of the special coordinate system \mathcal{L}' , the auxiliary medium and the reflector in the parametric form:

$$\hat{\mathbf{x}}'_{ref}(\vartheta, \varphi) \equiv (x'_{ref}(\vartheta, \varphi), y'_{ref}(\vartheta, \varphi), z'_{ref}(\vartheta, \varphi)). \quad (2.23)$$

In this section, I discuss how to find the traveltimes of the paraxial ray in the simplified model.

Consider an arbitrary point on the reflector. The traveltimes from the source location $\hat{\mathbf{x}}'_s$ to this arbitrary point and from this point to the receiver location $\hat{\mathbf{x}}'_g$ is obviously equal:

$$t(\vartheta, \varphi) = \frac{\sqrt{X_s'^2 + Y_s'^2 + Z_s'^2}}{\zeta_s(\Theta_s, \Phi_s)} + \frac{\sqrt{X_g'^2 + Y_g'^2 + Z_g'^2}}{\zeta_g(\Theta_g, \Phi_g)}, \quad (2.24)$$

where the following notations are used:

$$X'_i = x'_{ref} - x'_i, \quad Y'_i = y'_{ref} - y'_i, \quad Z'_i = z'_{ref} - z'_i, \quad i = s, g, \quad (2.25)$$

and ζ_s, ζ_g denote the group velocities. Substituting the relations for the group angles:

$$\sin^2 \Theta_i = \frac{X_i'^2 + Y_i'^2}{X_i'^2 + Y_i'^2 + Z_i'^2}, \quad \sin^2 \Phi_i = \frac{Y_i'^2}{X_i'^2 + Y_i'^2}, \quad i = s, g, \quad (2.26a)$$

$$\cos^2 \Theta_i = \frac{Z_i'^2}{X_i'^2 + Y_i'^2 + Z_i'^2}, \quad \cos^2 \Phi_i = \frac{X_i'^2}{X_i'^2 + Y_i'^2}, \quad i = s, g, \quad (2.26b)$$

and the definition of the group velocity (2.9) into (2.24) yields the compact DSR formula for the travelttime:

$$t(\vartheta, \varphi) = \sqrt{\frac{X_s'^2}{A_{11}} + \frac{Y_s'^2}{A_{22}} + \frac{Z_s'^2}{A_{33}}} + \sqrt{\frac{X_g'^2}{A_{11}} + \frac{Y_g'^2}{A_{22}} + \frac{Z_g'^2}{A_{33}}}. \quad (2.27)$$

Note that the resulting travelttime formula (2.27) is given as a function of the parameters ϑ and φ . The parameters ϑ_r, φ_r defining the reflection point of the paraxial ray $\hat{\mathbf{x}}'_r$ can be determined using Fermat's principle. According to Fermat's principle, the paraxial ray takes the path of the least travelttime. Hence, the parameters ϑ_r, φ_r may be found by solving the following system of nonlinear equations:

$$\begin{cases} \frac{\partial t}{\partial \vartheta} = 0, \\ \frac{\partial t}{\partial \varphi} = 0. \end{cases} \quad (2.28)$$

The travelttime formula (2.27) and the solution of the system (2.28) form the 3D implicit CRS stacking operator¹ (3D i-CRS). Below, I present two iterative approaches to solve the system (2.28). The choice of the approach depends on the type of parameterization of the reflector surface.

2.7.1 Linearized iterative approach

In this approach, the parameters ϑ and φ denote the lateral coordinates x' and y' , and the reflection surface is described by the continuous and twice differentiable function f of the lateral coordinates:

$$z'_{ref} = f(x', y'). \quad (2.29)$$

I assume that the reflection point of the paraxial ray is close to the reflection point of the central ray. Hence the reflection point displacements

$$\Delta x'_r \equiv x'_r - x'_{r0}, \quad \Delta y'_r \equiv y'_r - y'_{r0} \quad (2.30)$$

¹This name was given since the obtained stacking operator is "ideologically" close to the 2D implicit CRS stacking operator.

are small, compared to the typical scale of the problem. With this assumption, the system of equations (2.28) can be linearized:

$$\begin{cases} A_x + A_{xx}\Delta x'_r{}^{(j)} + A_{xy}\Delta y'_r{}^{(j)} = 0, \\ A_y + A_{yx}\Delta x'_r{}^{(j)} + A_{yy}\Delta y'_r{}^{(j)} = 0. \end{cases} \quad (2.31)$$

Here $\Delta x'_r{}^{(j)}$ and $\Delta y'_r{}^{(j)}$ are the updates of the reflection point coordinates at the j -th iteration

$$\Delta x'_r{}^{(j)} \equiv x'_r{}^{(j)} - x'_r{}^{(j-1)}, \quad \Delta y'_r{}^{(j)} \equiv y'_r{}^{(j)} - y'_r{}^{(j-1)}. \quad (2.32)$$

The coefficients A_x and A_y denote the first-order partial derivatives of the traveltime (2.27) with respect to the lateral coordinates of the reflection point, and the coefficients A_{xx} , A_{xy} , A_{yx} and A_{yy} are equal to the corresponding second-order partial derivatives. The coefficients are minutely discussed in Appendix B.2.

At the first iteration, the coefficients are estimated at the reflection point of the central ray. The linearized system (2.31) gives the first approximation of the reflection point coordinates $(x'_r{}^{(1)}, y'_r{}^{(1)})$. The next approximation $(x'_r{}^{(2)}, y'_r{}^{(2)})$ may be found by solving the system (2.31) with the coefficients taken at the point $\mathbf{x}'_r{}^{(1)}$. Accordingly, for the j -th iteration step, the coefficients are estimated at the point $(x'_r{}^{(j-1)}, y'_r{}^{(j-1)})$. Finally, after n iterations, I obtain the lateral coordinates of the reflection point $(x'_r{}^{(n)}, y'_r{}^{(n)})$ and get the traveltime according to the formula (2.27).

Note that the algorithm, described here is a generalization of the approach presented by [Abakumov et al. \(2013\)](#) for the case of the inhomogeneous overburden.

2.7.2 Trigonometric iterative approach

Alternatively, the reflector surface can be parameterized by polar angles. In this parameterization ϑ and φ denote the polar and azimuthal angles. In this case, the system of nonlinear equations (2.28) may be presented in the following way:

$$\tan \varphi = \mathcal{F}_1(\vartheta, \varphi, t_0, v_0, \mathbf{x}_s, \mathbf{x}_g, \mathbf{x}_0, \alpha, \beta, \mathbf{K}_{\text{NIP}}, \mathbf{K}_N) \quad (2.33a)$$

$$\tan \vartheta = \mathcal{F}_2(\vartheta, \varphi, t_0, v_0, \mathbf{x}_s, \mathbf{x}_g, \mathbf{x}_0, \alpha, \beta, \mathbf{K}_{\text{NIP}}, \mathbf{K}_N) \quad (2.33b)$$

The functions \mathcal{F}_1 and \mathcal{F}_2 are defined in Appendix B.3.

The angles ϑ and φ can be obtained iteratively with the equations (2.33). At the first iteration, I choose $\vartheta^{(0)}$ and $\varphi^{(0)}$ corresponding to the reflection point of the central ray:

$$\vartheta^{(0)} = 0, \quad \varphi^{(0)} = 0.$$

The equation (2.33a) gives an update $\varphi^{(1)}$. This updated value is used in the equation (2.33b) for $\vartheta^{(1)}$. The iterations are repeated until the convergence is achieved. Finally, after n iterations, I obtain the values $\vartheta^{(n)}$ and $\varphi^{(n)}$ and substitute them into the equation

(2.27) to get the traveltime of the reflected wave. The described approach is based on the method proposed by Schwarz et al. (2012) for the 2D i-CRS stacking operator.

Note that both iterative approaches potentially allow to find the traveltime of the reflected wave in the simplified model with any desired precision.

2.8 Explicit stacking operators

The recently introduced 3D i-CRS stacking operator is much more complicated than the conventional 3D CRS stacking operator, and hence its implementation into the CRS code is rather challenging. In this section, I propose alternative explicit stacking operators in order to achieve a good tradeoff between the accuracy and the efficiency of the implementation.

The idea here is to find an explicit approximation of the reflection point coordinates instead of solving the system (2.28). For a given simplified model, the reflection point of the paraxial ray depends only on the coordinates of source and receiver, or alternatively, on the offset \mathbf{h}' and the midpoint displacement \mathbf{m}' . The approximate location of the reflection point may be presented as a Taylor series expansion around the reflection point of the central ray:

$$\mathbf{x}'_r \approx \mathbf{x}'_{r_0} + \mathbf{B}_{\mathbf{h}'}\mathbf{h}' + \mathbf{B}_{\mathbf{m}'}\mathbf{m}' + \dots \quad (2.34)$$

Here $\mathbf{B}_{\mathbf{h}'}$ and $\mathbf{B}_{\mathbf{m}'}$ are 2×2 matrices describing the shift of the reflection point in the case of CMP and zero-offset acquisitions, respectively. The matrix $\mathbf{B}_{\mathbf{h}'}$ is equal to zero due to the reciprocity principle. The matrix $\mathbf{B}_{\mathbf{m}'}$ is equal to (see equation 2.22):

$$\mathbf{B}_{\mathbf{m}'} = \left[\mathbf{I} - \mathbf{K}'_{\text{NIP}}{}^{-1} \mathbf{K}'_{\text{N}} \right]. \quad (2.35)$$

2.8.1 3D DSR stacking operator

Substituting the approximation for \mathbf{x}'_r (2.34) into the traveltime formula (2.27) and omitting the terms of higher order than the second yield the 3D DSR stacking operator (see Appendix C.3 for detailed derivation):

$$t(\mathbf{m}, \mathbf{h}) = \frac{1}{2} \sqrt{\left[t_0 + \mathbf{w}^T \Delta \mathbf{x}_s \right]^2 + 2t_0 \left[\mathbf{m}^T \mathbf{N} \mathbf{m} - 2\mathbf{m}^T \mathbf{N} \mathbf{h} + \mathbf{h}^T \mathbf{M} \mathbf{h} \right]} + \frac{1}{2} \sqrt{\left[t_0 + \mathbf{w}^T \Delta \mathbf{x}_g \right]^2 + 2t_0 \left[\mathbf{m}^T \mathbf{N} \mathbf{m} + 2\mathbf{m}^T \mathbf{N} \mathbf{h} + \mathbf{h}^T \mathbf{M} \mathbf{h} \right]}, \quad (2.36)$$

where $\Delta \mathbf{x}_s$ and $\Delta \mathbf{x}_g$ denote the source and receiver displacements:

$$\Delta \mathbf{x}_s \equiv \mathbf{m} - \mathbf{h}, \quad \Delta \mathbf{x}_g \equiv \mathbf{m} + \mathbf{h}. \quad (2.37)$$

The 3D DSR stacking operator (2.36) includes only CRS parameters (1.20), and can be easily implemented into the CRS software. It is numerically slightly more expensive than

the conventional 3D CRS stacking operator (1.19). In the special cases of the flat reflector and the point diffractor in the homogeneous medium, formula (2.36) gives exact traveltimes. For the dipping plane reflector in the homogeneous medium, formula (2.36) is a short-spread approximation.

2.8.2 3D n-CRS stacking operator

The 3D DSR stacking operator (2.36) can be transformed to the 3D n-CRS stacking operator (see Appendix C.4 for details):

$$t(\mathbf{m}, \mathbf{h}) = \sqrt{\left[\frac{1}{2} \sqrt{\hat{F}(\mathbf{m} - \mathbf{h})} + \frac{1}{2} \sqrt{\hat{F}(\mathbf{m} + \mathbf{h})} \right]^2 + 2t_0 \mathbf{h}^T (\mathbf{M} - \mathbf{N}) \mathbf{h}} \quad (2.38)$$

where

$$\hat{F}(\mathbf{m}) = (t_0 + \mathbf{w}^T \mathbf{m})^2 + 2t_0 \mathbf{m}^T \mathbf{N} \mathbf{m}. \quad (2.39)$$

This stacking operator is identical to one proposed by Fomel and Kazinnik (2013) for the 3D case.

2.9 Conclusions

Along this chapter I reviewed the geometrical approach which is the basis of the derivation of the 2D DSR stacking operators. Based on this review, I proposed a simplified model in the 3D case. The simplified model consists of the special ray-centered coordinate system, the auxiliary anisotropic medium and the analytical reflector. The model is fully defined by the traveltime of the central ray, the near-surface velocity and the surface-based wavefield attributes. By means of this model, I found implicit and explicit 3D stacking operators for the traveltime of the paraxial ray.

The 3D implicit stacking operator (3D i-CRS) includes the system of nonlinear equations defining the reflection point coordinates and the DSR expression for the traveltime, as a function of the reflection point. This stacking operator allows to find the traveltime in the simplified model with any desired precision. The accuracy of the 3D i-CRS approximation is only restricted by the applicability of the simplified model. In the 2D case, this approach reduces to the 2D i-CRS stacking operator.

The 3D explicit stacking operator (3D DSR) is based on the first-order approximation of the reflection point coordinates. It is the DSR formula of the second-order accuracy. The formula has the same set of parameters as the conventional 3D CRS stacking operator and is thereby ready for implementation into the CRS-based software. The 3D DSR stacking operator can be transformed to the 3D n-CRS stacking operator.

In the next chapter, I will investigate the domain of the applicability of the simplified model and the accuracy of the 3D stacking operators. I will discuss the implementation of

the new stacking operators into the CRS software and I will compare the performance of the new operators with the one of the conventional 3D CRS.

Chapter 3

Accuracy and implementation of 3D DSR-based stacking operators

How accurate is the 3D simplified model? What is the "best" 3D DSR-based stacking operator? How do the DSR-based stacking operators improve the quality of the stacked section? These and other intriguing questions naturally arise from the findings presented in the previous chapter. In this chapter, I will answer these questions based on several numerical examples.

3.1 Applicability of the simplified model

In the simplified model, the traveltime of the reflected ray could be found with any desired precision. However, the simplified model correctly describes propagation of reflected rays only in the vicinity of the central ray. Hence, it is important to investigate the range of applicability of the simplified model.

In order to test the applicability of the simplified model, I consider the so-called Complex model (see Figure 3.1a). The Complex model consists of the analytical reflector below the inhomogeneous overburden with the velocity profile typical for the Gulf of Mexico. Such a model is complicated enough to possess all effects of the real 3D media and at the same time allows the numerical computation of traveltimes of reflected waves. The Complex model is characterized by the depth of the NIP point D , which in this case is approximately equal to 1 *km*.

A corresponding simplified model is shown in Figure 3.1b. The model consists of the homogeneous anisotropic auxiliary medium (blue layer in Figure 3.1b) and ellipsoidal or parabolic reflector (red surface). The simplified model is valid if the traveltime of the reflected ray in the simplified model t_{sm} is almost identical to the traveltime of the reflected ray in the Complex model t_{cm} .

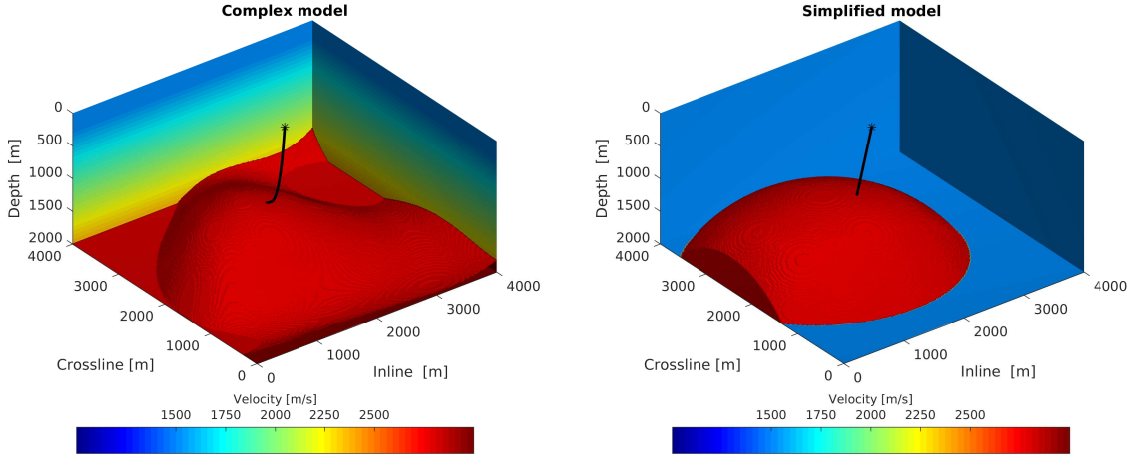


Figure 3.1: Illustration of the Complex model (a) and the corresponding simplified model (b). The Complex model consists of the constant velocity part ($v_0 = 1500 \text{ m/s}$, $z \leq 250 \text{ m}$) simulating the water layer, and the constant-gradient velocity part ($v = v_0 + \kappa(z - z_0)$, $z_0 = 250 \text{ m}$, $\kappa = 0.5 \text{ s}^{-1}$, $z > 250 \text{ m}$) simulating the sedimentary layer. The reflector (red surface) simulates the top of the salt body. The reflector is described by the fourth order polynomial function of lateral coordinates. The black line indicates the trajectory of the central ray. The depth of the NIP point is approximately equal to 1.0 km . The simplified model (b) is constructed for the particular central ray.

The CMP and ZO experiments could be used to identify the range of applicability of the simplified model. These experiments allow to obtain the relative error of traveltimes in the simplified model

$$E = \frac{t_{sm} - t_{cm}}{t_{cm}} \cdot 100\% \quad (3.1)$$

as a function of the half-offset $\mathbf{h} = \{h_x, h_y\}$ and the midpoint displacement $\mathbf{m} = \{m_x, m_y\}$ (see Figure 3.2).

As follows from Figures 3.2a,c, the simplified model is valid for traces with offsets $|\mathbf{h}| < D$ and midpoint displacements $|\mathbf{m}| < D/2$ (relative error does not exceed 0.2% and 0.3%, respectively). There is no systematic difference between the ellipsoidal and parabolic reflector (compare images a, c with b, d in Figure 3.2), however the simplified model with the ellipsoidal reflector provides a slightly better result.

3.2 The most effective iterative approach

In Section 2.7, I proposed two iterative approaches to find the traveltime of the reflected wave in the simplified model: the trigonometric iterative approach (TIA, equations 2.33), which is the extension of the method proposed by Schwarz et al. (2012) to the 3D case, and the linearized iterative approach (LIA, equations 2.31). In this Section, I will investigate

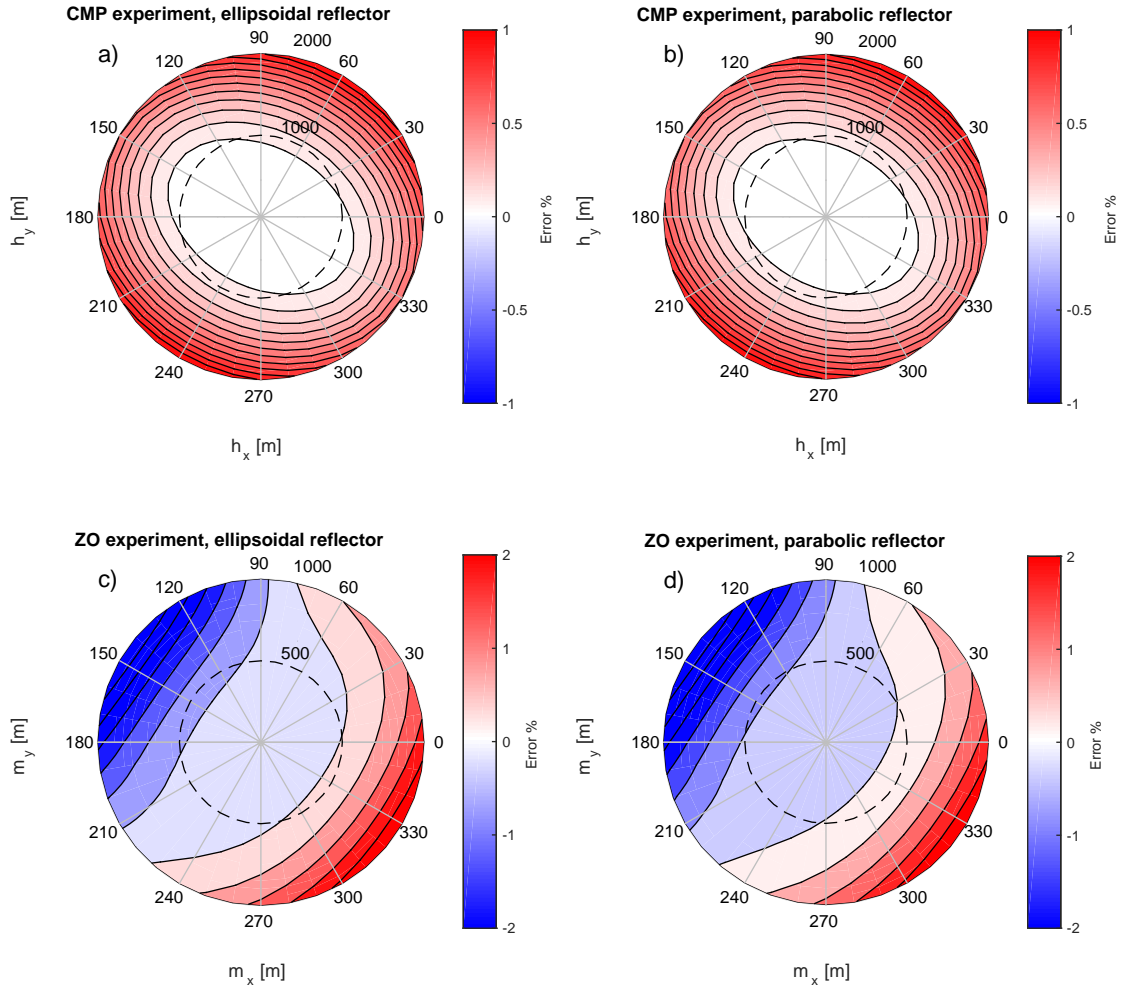


Figure 3.2: Relative errors (3.1) E of the traveltimes in the simplified model for the CMP and ZO experiments. In the CMP experiment (a,b), E is a function of $|\mathbf{h}|$ and azimuth angle $\xi_{\mathbf{h}}$: $0 \leq |\mathbf{h}| \leq 2000$ m, $0^\circ \leq \xi_{\mathbf{h}} \leq 360^\circ$, $|\mathbf{m}| = 0$. In the ZO experiment (c,d), E is a function of $|\mathbf{m}|$ and azimuth angle $\xi_{\mathbf{m}}$: $0 \leq |\mathbf{m}| \leq 1000$ m, $0^\circ \leq \xi_{\mathbf{m}} \leq 360^\circ$, $|\mathbf{h}| = 0$. Relative errors are computed for the simplified model with the ellipsoidal (a,c) and parabolic (b,d) reflectors.

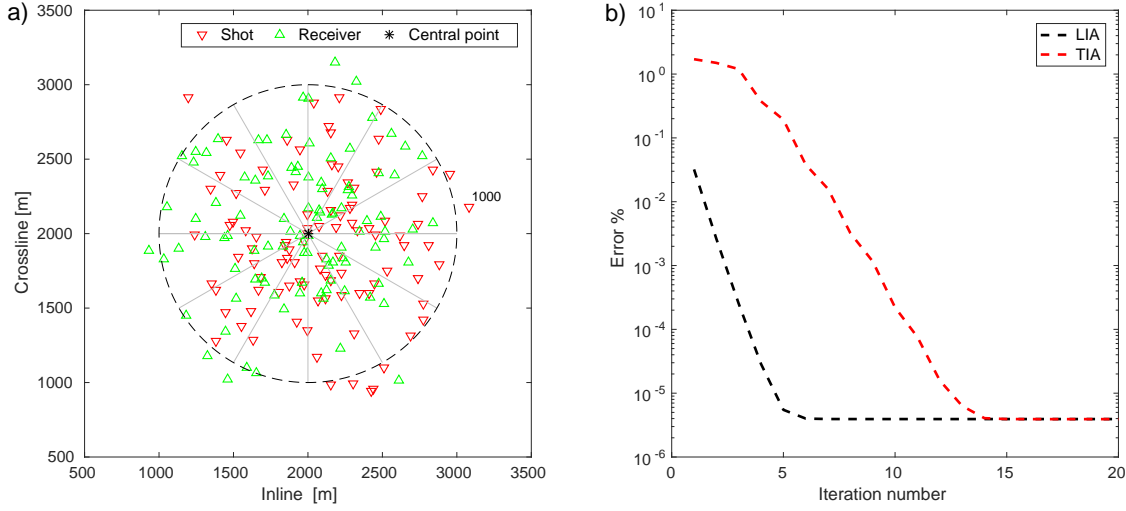


Figure 3.3: Illustration of the acquisition geometry: 100 randomly distributed source-receiver pairs in the vicinity of the central point (a). The RMS traveltime errors plotted as functions of the iteration number (b).

which of these approaches perform best in the 3D case.

In order to answer this question, I consider $N = 100$ randomly distributed source-receiver pairs (see Figure 3.3a) that satisfy the criteria of validity of the simplified model ($|\mathbf{h}| < D$, $|\mathbf{m}| < D/2$). The simplified model with the ellipsoidal reflector was chosen to compare the LIA and TIA methods.

For comparison, it is convenient to use the root-mean-square (RMS) traveltime error $\delta t_{\text{RMS}}(i)$ which is equal to

$$\delta t_{\text{RMS}}(i) = \sqrt{\frac{1}{N} \sum_{k=1}^N \left(\frac{t^k(i) - t_{ex}^k}{t_{ex}^k} \right)^2} \cdot 100\%, \quad (3.2)$$

where t_{ex}^k is the exact (computed numerically to very high precision) traveltime in the simplified model from the source at \mathbf{x}_s^k to the receiver at \mathbf{x}_g^k and $t^k(i)$ is the corresponding traveltime obtained by the TIA/LIA methods on the i -th iteration step.

The RMS traveltime errors as functions of the iteration number are shown in Figure 3.3b. As follows from the figure, LIA converges significantly faster than TIA (LIA requires only 5 iterations to reach the precision of the numerical computation, while TIA requires 14 iterations). In practice, 1-2 iterations are enough for LIA, while TIA requires more than 5 iterations.

Note that these results are only valid for the 3D case. Tests in the 2D case (and in the 3D case with a spherical reflector) do not reveal significant difference between both approaches.

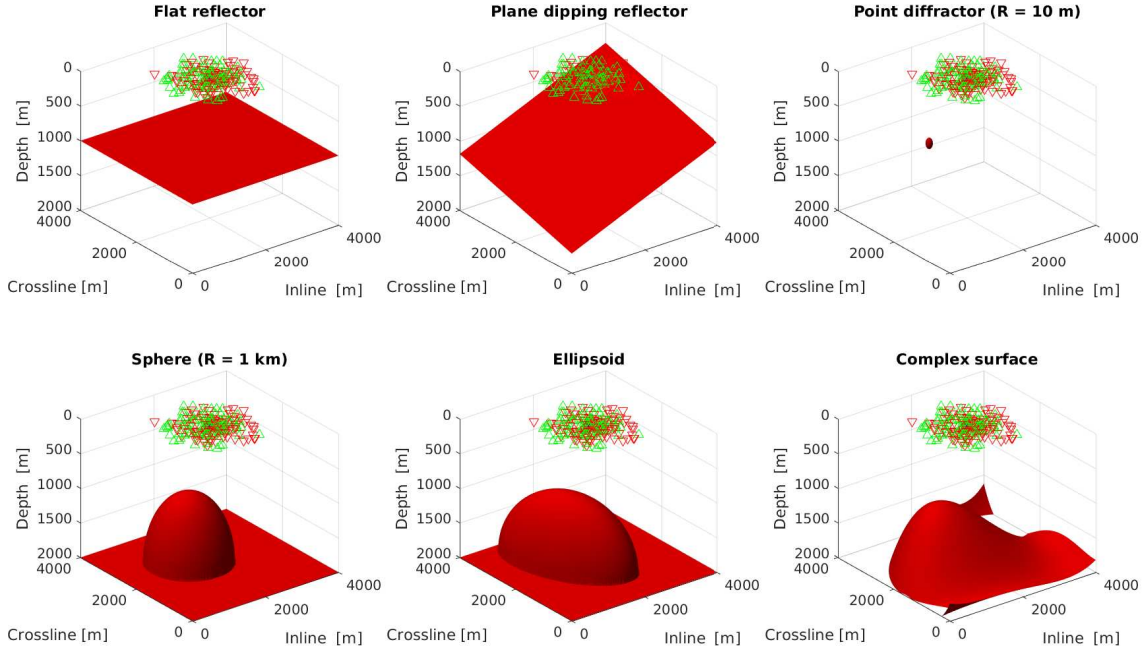


Figure 3.4: Illustration of six analytical reflectors.

3.3 The most accurate stacking operator

As one can conclude from the previous sections, the best realization of the 3D i-CRS stacking operator is the one with the ellipsoidal reflector and LIA. In this section, I will compare 3D CRS (1.19), 3D DSR (2.36), 3D n-CRS (2.38) and three different realizations of the 3D i-CRS stacking operator (I - LIA, parabolic reflector, II - LIA, ellipsoidal reflector, III - TIA, ellipsoidal reflector) to find “the most accurate” stacking operator.

I consider six different reflectors (see Figure 3.4): the flat reflector, the plane dipping reflector, the point diffractor¹, the sphere, the ellipsoid and the analytical reflector from the Complex model. Each of these reflectors is combined with three different overburden structures:

- **Const** - constant velocity overburden ($v_0 = 1500 \text{ m/s}$) simulating the water layer;
- **Grad** - constant-gradient velocity overburden ($v = v_0 + \kappa z$, $v_0 = 1500 \text{ m/s}$, $\kappa = 0.5 \text{ s}^{-1}$) simulating the sedimentary layer;
- **1-D** - overburden of complex structure that consists of the water layer (depth < 250 m) and the sedimentary layer (depth > 250 m).

All reflectors are chosen in such a way that the depth of the NIP point D is approximately equal to 1 km. Hence, previously used acquisition geometry (from Figure 3.3a) is applicable

¹The point diffractor is simulated by the spherical reflector with the radius $R = 10 \text{ m}$.

for all 18 models. For each stacking operator the RMS travelt ime error (3.2) is computed (see Table 3.1).

Table 3.1: RMS travelt ime errors

Reflector	Velocity	CRS	DSR	n-CRS	i-CRS ^I	i-CRS ^{II}	i-CRS ^{III}
Flat reflector	Const	<u>0.000</u>	0.000	0.000	0.000	0.000	—
	Grad	<u>0.058</u>	0.058	0.058	0.059	0.059	—
	1-D	<u>0.050</u>	0.050	0.050	0.050	0.050	—
Plane dipping reflector	Const	<u>0.000</u>	0.207	0.000	0.001	0.001	—
	Grad	<u>0.184</u>	0.232	0.191	0.189	0.189	—
	1-D	<u>0.183</u>	0.225	0.190	0.188	0.188	—
Point diffractor (R=10m)	Const	0.878	0.005	0.002	0.001	<u>0.000</u>	0.000
	Grad	0.908	0.091	<u>0.089</u>	0.092	0.092	0.092
	1-D	0.905	0.085	<u>0.083</u>	0.086	0.085	0.085
Sphere (R=1km)	Const	0.241	0.087	0.043	0.007	<u>0.000</u>	0.000
	Grad	0.275	0.159	<u>0.098</u>	0.108	0.108	0.109
	1-D	0.273	0.153	<u>0.093</u>	0.104	0.104	0.105
Ellipsoid	Const	0.207	0.118	0.061	0.022	<u>0.022</u>	0.339
	Grad	0.167	0.123	<u>0.092</u>	0.095	0.096	0.621
	1-D	0.163	0.117	<u>0.086</u>	0.090	0.090	0.619
Complex surface	Const	0.192	0.067	<u>0.017</u>	0.049	0.048	0.048
	Grad	0.224	0.145	<u>0.108</u>	0.128	0.128	0.130
	1-D	0.223	0.144	<u>0.108</u>	0.128	0.128	0.130

As follows from the table, all stacking operators behave equally well for the flat reflector and the plane dipping reflector. An exception is the 3D DSR stacking operator which gives an approximate travelt ime in the case of the plane dipping reflector.

In the case of quadric surfaces (point diffractor, sphere, ellipsoid) 3D i-CRS (for the homogeneous overburden) and 3D n-CRS (for the inhomogeneous overburden) provide the most accurate result. For these models, all DSR-based stacking operators fit travelt imes of the reflected events significantly better than the conventional 3D CRS stacking operator.

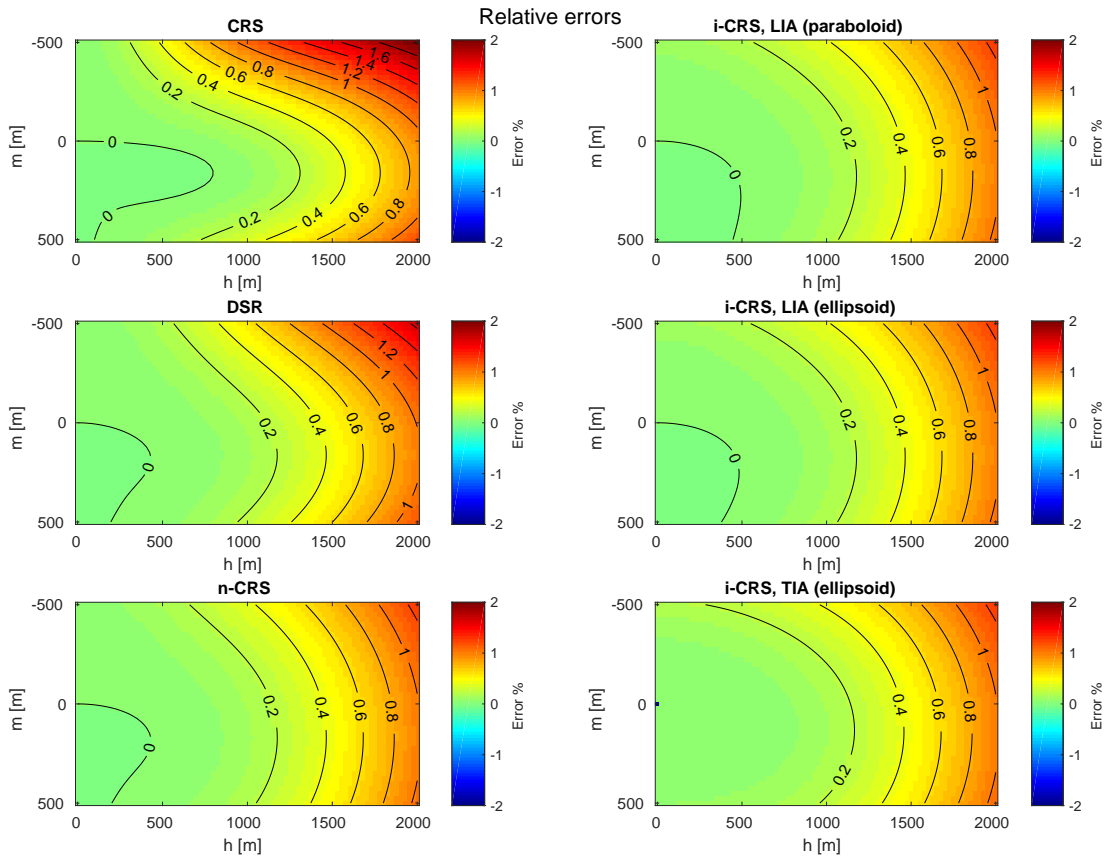


Figure 3.5: Relative errors of 3D CRS, 3D DSR, 3D n-CRS and 3D i-CRS stacking operators along the 2D profile.

For complex analytical reflector, 3D n-CRS remains the most accurate stacking operator even in the case of homogeneous overburden.

No significant differences were observed between different realizations of the i-CRS stacking operator. As expected, the realization II (LIA, ellipsoidal reflector) yields superior result over the other two realizations. The realization III (TIA, ellipsoidal reflector) could not be applied in the case of plane reflectors. As expected, for a given number of iterations (three iterations in this particular case) the realization III (TIA, ellipsoidal reflector) is less accurate than the realization II (LIA, ellipsoidal reflector).

For the Complex model, I additionally compute the relative errors of traveltimes along the 2D profile (see Figure 3.5). As expected, 3D n-CRS and different realizations of 3D i-CRS demonstrate comparable accuracy, which is much higher than the one of conventional 3D CRS.

The results of this section indicate that 3D n-CRS is "the most accurate" 3D DSR-based stacking operator.

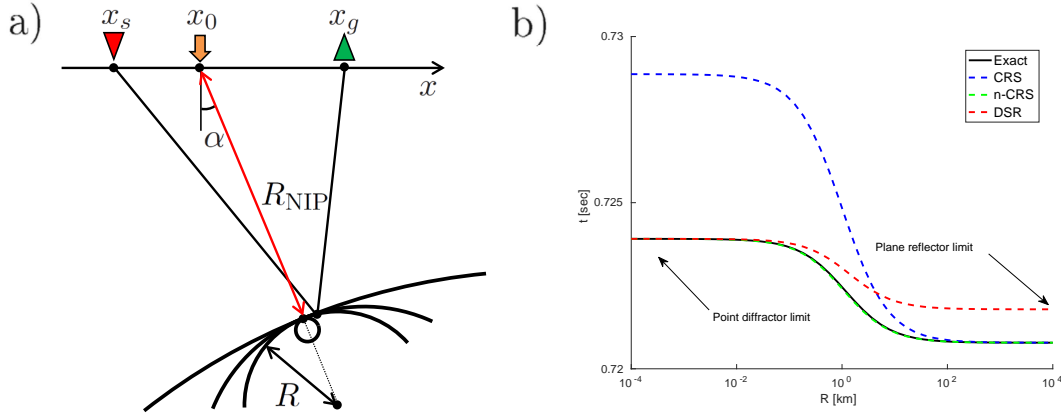


Figure 3.6: Illustration of the model with the reflector of varying curvature (a). The following model parameters are fixed and are equal: $R_{\text{NIP}} = 1.0 \text{ km}$, $\alpha = 30^\circ$, $m = 0.2 \text{ km}$, $h = 0.4 \text{ km}$, $v_0 = 3.2 \text{ km/s}$. The radius of curvature of the reflector R varies from 10^{-4} km to 10^4 km . Illustration of the corresponding exact traveltimes and CRS, DSR and n-CRS traveltimes approximations (b).

3.4 On the role of explicit stacking operators

In the previous sections, I investigated different realizations of the 3D i-CRS stacking operator. In this section, I would like to discuss relations between different explicit stacking operators – 3D CRS, 3D DSR and 3D n-CRS.

The tests in the previous section indicate that the CRS stacking operator is accurate for plane reflectors and is not accurate for point diffractors. On the contrary, the DSR stacking operator perfectly fits diffraction events and is a short-offset approximation in the case of the plane dipping reflector. As follows from the tests, n-CRS perfectly matches both cases.

For better understanding of these observations, I consider a circular reflector with varying radius of curvature R in the homogeneous medium (see Figure 3.6a). For a wide range of radii R (from 10^{-4} km , corresponding to the point diffractor limit, to 10^4 km , corresponding to the plane reflector limit) I computed CRS, DSR and n-CRS approximations and compared them with the exact (computed numerically) traveltime (see Figure 3.6b). Figure 3.6b illustrates the idea that CRS and DSR are two asymptotic solutions of the reflection traveltime. The n-CRS stacking operator, being accurate for the whole range of curvatures, sews both asymptotic solutions. This fact explains outstanding accuracy of the n-CRS stacking operator.

Further discussion about the link between the CRS and DSR stacking operators in the context of the paraxial ray theory will be given in Chapter 5.

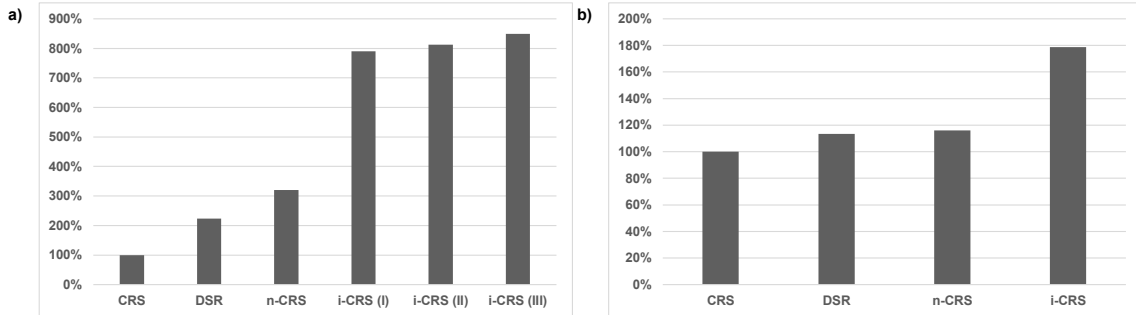


Figure 3.7: Relative computational difficulty of the 3D stacking operators (a) and the 3D CRS code with different 3D stacking operators (b). Conventional 3D CRS is taken as reference (100%).

3.5 Computational difficulty

As already mentioned in Section 2.8, computational difficulty of the new stacking operators is higher than the one of the conventional 3D CRS. The relative computational difficulty of the 3D stacking operators is shown in Figure 3.7a. In terms of computational difficulty, there is almost no difference between three realizations of the 3D i-CRS stacking operator, however all of them are about eight times more “expensive” than the conventional 3D CRS. As expected, explicit stacking operators are more efficient than implicit operators, taking only two (3D DSR) and three (3D n-CRS) times more computational time than the conventional 3D CRS.

In the 3D CRS code, the computation of the moveout takes about 10% of the total computation time. The 3D CRS code with explicit stacking operators requires slightly more computational time (approximately 13% and 16% more for 3D DSR and 3D n-CRS) than the code with the conventional 3D CRS stacking operator (see Figure 3.7b). The same code with the 3D i-CRS stacking operator is significantly more expensive (additionally 80% of the computation time). Hence, the 3D n-CRS stacking operator achieves the best trade-off between the accuracy and the computational difficulty.

3.6 Implementation into the CRS software

Xie and Gajewski (2016) have recently presented the 3D CRS software with automatic estimation of the stacking parameters by global optimization algorithm. The new software allows implementation of the 3D DSR-based stacking operators. The set of stacking parameters for 3D DSR and 3D n-CRS coincides with the one of conventional 3D CRS (\mathbf{w} , \mathbf{M} and \mathbf{N}). The stacking parameters for 3D i-CRS could be (\mathbf{w} , \mathbf{M} and \mathbf{K}'_R), where \mathbf{K}'_R is the curvature matrix of the reflector. Though the sets of parameters (\mathbf{w} , \mathbf{M} and \mathbf{N}) and (\mathbf{w} , \mathbf{M} and \mathbf{K}'_R) are linked, I expect that the parameter search in terms of (\mathbf{w} , \mathbf{M} and \mathbf{K}'_R) could get additional advantages.

3.7 Conclusions

In this chapter, I analyzed the different realizations of the 3D i-CRS stacking operator and compared accuracy of the 3D DSR-based stacking operators. I found that the trigonometric iterative approach, which is very efficient in the 2D case, does not properly work in the 3D case. The linearized iterative approach, which was proposed as an alternative to TIA, demonstrates significantly better results.

The accuracy tests demonstrated that 3D n-CRS and 3D i-CRS are the most accurate stacking operators. Taking into account the computational difficulty, I found 3D n-CRS to be the most promising 3D DSR-based stacking operator.

All 3D DSR-based stacking operators could be integrated into the CRS software with a global search of stacking parameters. Study of their impact on complex synthetic and field datasets will hopefully be a topic of future research.

Chapter 4

DSR-based stacking operators for converted waves

Converted PS waves have attracted considerable interest because they are commonly used to obtain valuable information about S-waves. However, the existing DSR-based stacking operators are not designed for converted waves.

In this chapter, I propose a double-square-root traveltime approximation (DSR-PS) for converted waves. This approximation is based on a fairly general assumption of constant ratio of P- and S-wave velocities. Furthermore, I demonstrate that a CRS-type traveltime approximation for converted waves may be derived from the new approximation. It enables to introduce a pragmatic search strategy for converted waves, similar to the one for monotypic waves. The DSR-PS stacking operator and the new pragmatic search strategy together form an efficient way to obtain high-quality stacked sections for PS converted waves.

4.1 Introduction

There are two types of body waves of different polarization in an isotropic medium: a compressional (or primary) P-wave and a shear S-wave. Originally, the reflection seismic imaging utilized only compressional PP reflected waves. However, the appearance of multicomponent surveys in the early 1980s ([Garotta, 1985](#)), gave rise to registration and processing of other types of reflected wavefields (PS, SP, SS). Thus, the multicomponent measurements made it possible to obtain S-wave information.

The shear waves contain important information about the properties of the subsurface and are widely used in seismic applications. For example, velocities of S-waves are used for the estimation of porosity and permeability, which are two important parameters for the reservoir characterization ([Nelson, 2001](#)). S-waves are needed for the detection of porous

zones (Coulombe et al., 1996) and for identification and quantification of seismic anisotropy (Tsvankin, 2012). Since the velocity of S-waves is typically half that of P-waves and the frequency content of P- and S-events is almost the same, the images, obtained by S-waves, have higher spatial resolution than the associated PP images (Stewart et al., 2002).

For many reasons, pure SS reflection experiments are rarely used in seismic exploration. This is mainly because the efficient sources of S-waves are expensive, SS reflections are typically noisy and SS listening times are about double or triple those of P-waves (Stewart et al., 2002). Moreover, SS surveys are not applicable in marine measurements. In contrast to SS, PS surveys are relatively inexpensive (Kendall and Davis, 1996) and they do not require special types of sources. Hence, converted PS reflections are an alternative to pure SS reflections.

The price we have to pay for this convenience is the asymmetry of the ray path of converted waves. According to Snell's law, the angle of incidence and the angle of reflection are not the same for PS reflections. Moreover, the idea of reciprocity (invariance of the moveout under the exchange of source and receiver positions), utilized in standard CMP-processing, is violated for converted waves (Thomsen, 1999). As a consequence, the traveltimes of the converted wave becomes asymmetric because it has a linear term of offset. For these reasons, the standard CMP-based processing is not applicable for converted waves.

The fundamentals of converted wave processing appeared at late 1980s - early 1990s. In order to overcome the conversion point dispersal, it was proposed to sort the traces into the common-conversion-point (CCP) gathers instead of conventional CMP gathers. The successful examples of stacking of converted waves in CCP gathers were demonstrated by Tessmer and Behle (1988), Tessmer et al. (1990) and Iverson et al. (1989). However, even for simple velocity models it is a complicated problem to find a CCP gather (e.g. Tessmer and Behle (1988); Thomsen (1999)).

With appearance of multiparameter stacking the problem of powerful stacking technique for converted waves arose again. A 2D CRS-based stacking operator for converted waves was presented by Bergler et al. (2002). In order to account for the asymmetric PS ray path, Bergler et al. (2002) used the common-offset (CO) CRS stacking operator. The disadvantage of this method is that the CO CRS operator uses five parameters that do not have a physically intuitive explanation. The 2D i-CRS stacking operator for converted waves was proposed by Vanelle et al. (2012a). To my knowledge, there are no MF or n-CRS extensions for converted waves. Hence, there is an interest to investigate the DSR-based stacking operators for converted waves.

The aim of this chapter is to obtain the DSR and n-CRS traveltimes approximations for converted waves valid for arbitrary observation geometry and arbitrary reflector curvature. To achieve this goal, I introduce the simplified model of subsurface (Section 4.2.2) and the special γ -CMP coordinates (Section 4.2.3) that accounts for the asymmetry of PS trajectories. With these tools, I derive the DSR-PS and n-CRS-PS stacking operators for converted waves, based on the geometrical approach (Section 4.2.4). The DSR-PS stacking operator may be transformed to the CRS-PS stacking operator, which is formally

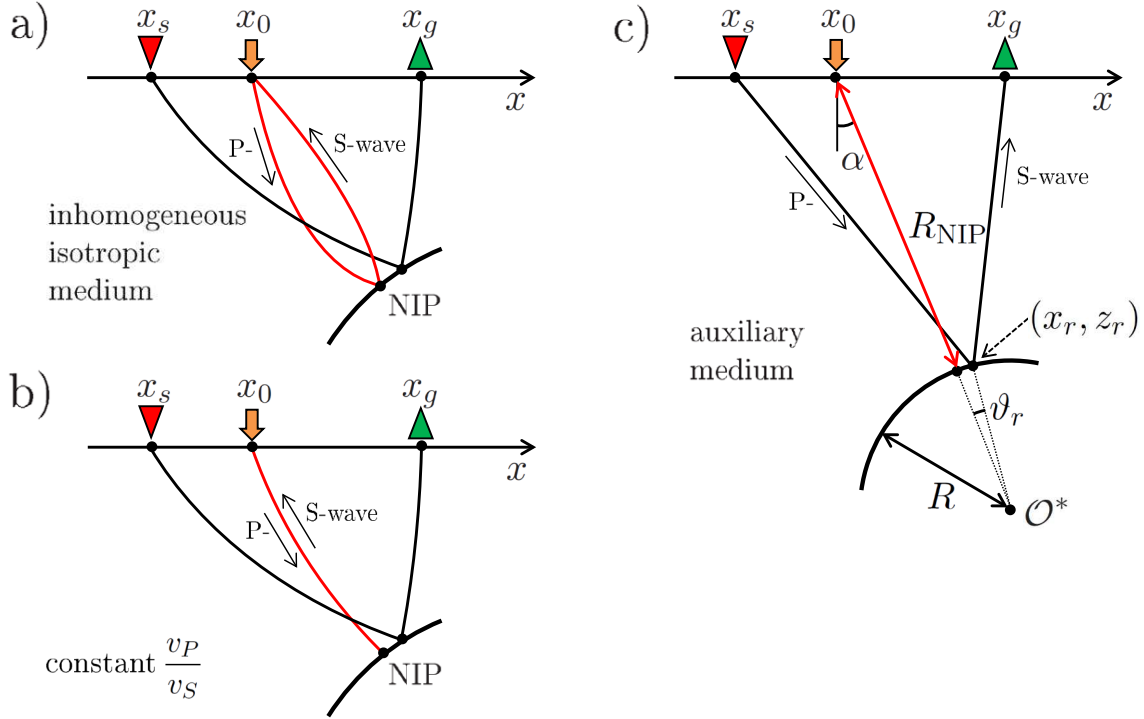


Figure 4.1: Illustration of the PS reflection experiment. The down- and upgoing segments of the central PS ray do not coincide in the arbitrary inhomogeneous medium (a). However, they have the same trajectories under the assumption of constant v_P/v_S ratio (b). This fact enables one to introduce a simplified model for PS waves (c).

similar to the ZO CRS operator (Section 4.2.5). Both DSR-PS and CRS-PS have clear extension to the 3D case (Section 4.2.7). The CRS-PS stacking operator makes it possible to formulate a pragmatic search strategy for converted waves (Section 4.3.2). For non-converted waves, this strategy transforms to the well-known pragmatic approach of Müller (1999). Finally, I present several numerical simulations that provide insight into the accuracy of the new approximations (Section 4.3.1), the accuracy of the estimated wavefield attributes (Section 4.3.3) and the quality of the resulted stacked sections (Section 4.3.4).

4.2 Theory

In this chapter, I assume that the ratio of compressional velocity v_p to shear velocity v_s is constant. For the most rocks this ratio varies from 1.6 to 2.0. Hence, the average value of 1.8 is relatively accurate (about 10% accuracy) for the most real rocks.

4.2.1 Statement of the problem

In the PS reflection experiment, the compressional P-wave, emitted by the source, propagates in the inhomogeneous medium. The P-wave partly "converts" to the S-wave upon reflection and returns back to the measurement surface (see Figure 4.1a). In the zero-offset case, the source and receiver locations of the central ray coincide at the central point x_0 . The traveltime of the central ray is equal t_0 . The problem is to find a traveltime t of the paraxial converted ray, whose source and receiver are located in the vicinity of central point x_0 at the positions x_s and x_g , respectively.

In an arbitrary inhomogeneous medium the trajectories of P- and S-segments of the central ray do not necessarily coincide. Therefore, these ray-segments should not be perpendicular to the reflector at the reflection point, and the incidence and the emergence angles of the central ray may differ considerably (see Figure 4.1a). However, under the assumption that the ratio of P- and S-wave velocities is constant, the trajectory of the central ray simplifies: down- and upgoing ray segments coincide, the central ray is perpendicular to the reflector and the incidence and the emergence angles are equal (see Figure 4.1b). This simplification enables to introduce the simplified model for converted waves.

4.2.2 Simplified model for converted waves

As discussed in Section 2.2, for monotypic reflected waves (PP or SS) it is possible to replace the inhomogeneous medium with the reflector of arbitrary shape by the so-called simplified model. In the 2D case, the simplified model consists of the circular reflector in the auxiliary medium of constant velocity. The parameters of the simplified model (the velocity v and the radius of a circular reflector R) are established upon the consideration of the hypothetical normal-incidence-point (NIP) and normal experiments.

Due to the constant velocity ratio, the curvatures of the NIP R_{NIP} and normal R_{N} wavefronts are identical both for P- and S-waves. These curvatures define effective velocities of P- and S-waves (v_P and v_S , respectively, $\gamma = v_P/v_S$) and the radius of circular reflector R :

$$R = R_{\text{N}} - R_{\text{NIP}}. \quad (4.1)$$

The effective velocity of a converted PS wave is determined by the condition that the traveltime of the central ray must coincide in the inhomogeneous and in the auxiliary media:

$$t_0 = \frac{2R_{\text{NIP}}}{v_{PS}}. \quad (4.2)$$

There is obviously an important relationship between the effective velocity of PS wave v_{PS} and the effective velocities of P- and S-waves:

$$\frac{2}{v_{PS}} = \frac{1}{v_P} + \frac{1}{v_S}. \quad (4.3)$$

The velocities v_P , v_S and the circular reflector form the simplified model for converted waves (see Figure 4.1c). The simplified model is determined by the traveltime of the

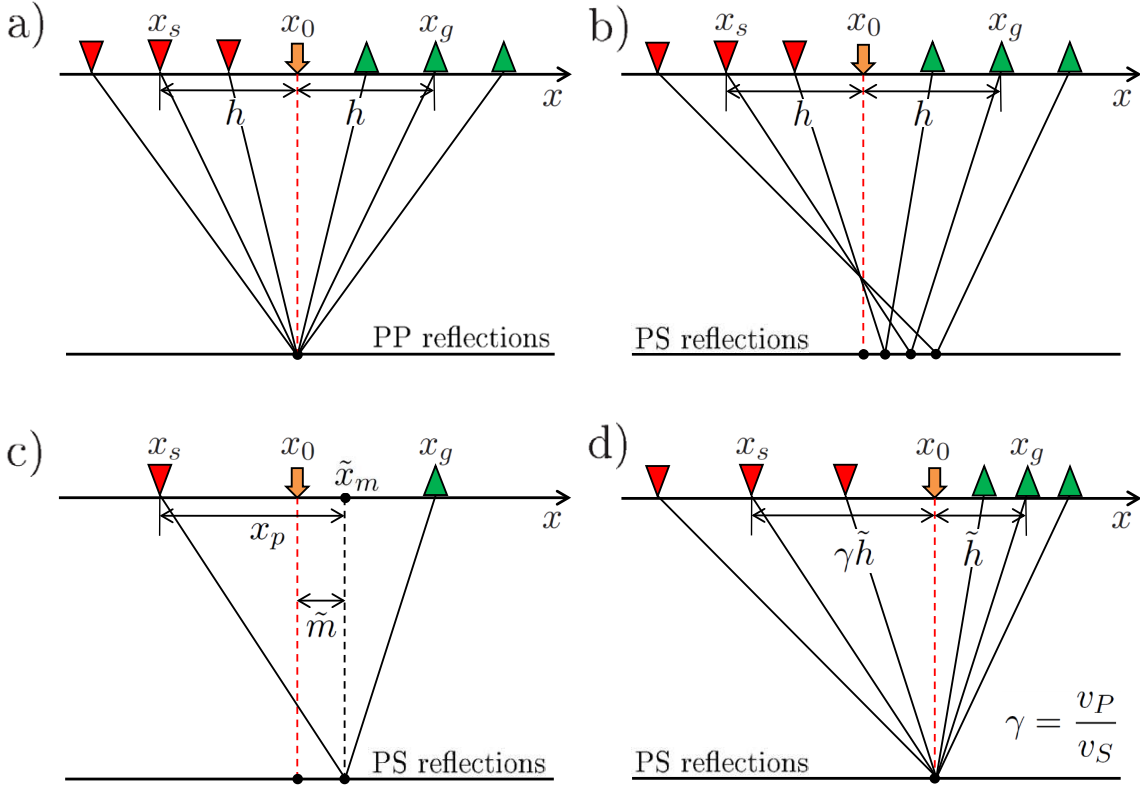


Figure 4.2: In the conventional CMP gather, sources and receivers are located symmetrically with respect to the central point (a). In the case of a horizontally layered medium, all reflection points of PP rays coincide with the NIP. In the case of converted waves (b), the reflection points of PS rays in the CMP gather are smeared. [Fromm et al. \(1985\)](#) found an approximation for the lateral position of the conversion point (c). Based of this idea, I propose to use γ -CMP gathers (d) for stacking PS converted waves.

central ray t_0 and the kinematic wavefield attributes: the emergence angle of the central ray α and the radii of NIP R_{NIP} and normal R_{N} waves. In the simplified model, the DSR stacking operator for converted waves can be derived using the geometrical approach.

4.2.3 γ -CMP coordinates

Before considering the stacking operators for converted waves, I will briefly describe the special coordinate system required to simplify the expressions of these operators.

Conventionally, the reflection data are sorted into the common-midpoint (CMP) gathers ([Mayne, 1962](#)). The CMP gathers are popular because for horizontally layered media, the PP reflections in the CMP gather image the same point in depth (see Figure 4.2a). However, since the path of the converted wave is asymmetric, the PS reflections in the CMP gather come from different points in the subsurface (i.e., the effect of the conversion-

point dispersal occurs (see Figure 4.2b)). Hence, successful stacking of converted waves can not be achieved using the CMP gathers and requires special common conversion point (CCP) gathers (Tessmer and Behle, 1988).

For constant v_P , v_S velocities and a flat horizontal reflector, Fromm et al. (1985) found the approximate position of the conversion point \tilde{x}_m (see Figure 4.2c):

$$\tilde{x}_m = x_s + x_p, \quad x_p = \frac{\gamma(x_g - x_s)}{1 + \gamma}, \quad \gamma = v_P/v_S. \quad (4.4)$$

Following this idea, I introduce the γ -CMP coordinates \tilde{m} and \tilde{h} :

$$\tilde{x}_m \equiv \frac{\gamma x_g + x_s}{1 + \gamma}, \quad \tilde{m} \equiv \tilde{x}_m - x_0, \quad \tilde{h} \equiv \frac{x_g - x_s}{1 + \gamma}. \quad (4.5)$$

With the γ -CMP coordinates, I can express the source and receiver displacements as:

$$\Delta x_s = \tilde{m} - \gamma \tilde{h}, \quad \Delta x_g = \tilde{m} + \tilde{h}. \quad (4.6)$$

Traces having the same value of \tilde{m} are collected in the γ -CMP gather (see Figure 4.2d). The γ -CMP gather can be considered as the first linear approximation of the CCP gather. Note that in the particular case of monotypic waves ($\gamma = 1$), the γ -CMP coordinates (4.5) coincide with the standard CMP coordinates (1.1).

4.2.4 DSR stacking operator for converted waves

In the simplified model (see Figure 4.1c), the traveltime of a PS wave from the source at x_s to the reflector to the receiver at x_g is equal:

$$t(\vartheta) = \frac{\sqrt{(x_s - x_{ref})^2 + z_{ref}^2}}{v_P} + \frac{\sqrt{(x_g - x_{ref})^2 + z_{ref}^2}}{v_S}. \quad (4.7)$$

Here, both the source and the receiver are at the depth $z = 0$, and the angle ϑ defines the point on the circular reflector $(x_{ref}(\vartheta), z_{ref}(\vartheta))$. As in the case of monotypic waves, the angle ϑ_r defining the conversion point (x_r, z_r) can be found either implicitly or explicitly.

The implicit stacking operator for converted waves was proposed by Vanelle et al. (2012a). The traveltime t must fulfill Fermat's principle, i.e., $\partial t / \partial \vartheta = 0$, which leads to an implicit equation for ϑ (see Vanelle et al. (2012a), eq. 13):

$$\tan \vartheta = \mathcal{F}(\vartheta, t_0, x_s, x_g, x_0, \text{model parameters}). \quad (4.8)$$

The equation (4.8) is solved iteratively with the initial value of ϑ corresponding to the conversion point of the central ray (NIP). The result ϑ_r is substituted into (4.7) to compute the traveltime of PS wave. With the 3D auxiliary anisotropic medium, proposed in Section 2.4, the extension of this method to the 3D case is straightforward.

In this section, I will present another approach, which is ideologically close to the 3D explicit DSR stacking operator (see Section 2.8). Assuming that the source and receiver displacements are much smaller than the characteristic distance of the problem (such as R_{NIP} or R_{N}), and using Snell's law, I obtain the following expression for the angle ϑ_r describing the reflection point (see Appendix D.1):

$$\sin \vartheta_r \approx \frac{\tilde{m}}{R_{\text{N}}} \cos \alpha. \quad (4.9)$$

Substituting the reflection point approximation (4.9) into the expression for PS travel-time (4.7) I obtain, after some algebraic manipulations, the explicit¹ DSR-PS stacking operator for converted waves (see Appendix D.2 for detailed derivation):

$$t(\tilde{m}, \tilde{h}) = \frac{1}{1+\gamma} \sqrt{\left[t_0 + \tilde{w} \Delta x_s \right]^2 + 2t_0 \left[\tilde{N} \tilde{m}^2 - 2\tilde{N} \tilde{m} (\gamma \tilde{h}) + \tilde{M} (\gamma \tilde{h})^2 \right]} \\ + \frac{\gamma}{1+\gamma} \sqrt{\left[t_0 + \tilde{w} \Delta x_g \right]^2 + 2t_0 \left[\tilde{N} \tilde{m}^2 + 2\tilde{N} \tilde{m} \tilde{h} + \tilde{M} \tilde{h}^2 \right]} \quad (4.10)$$

with parameters:

$$\tilde{w} = -\frac{2 \sin \alpha}{v_{\text{PS}}}, \quad \tilde{M} = \frac{\cos^2 \alpha}{v_{\text{PS}} R_{\text{NIP}}}, \quad \tilde{N} = \frac{\cos^2 \alpha}{v_{\text{PS}} R_{\text{N}}}. \quad (4.11)$$

The DSR-PS stacking operator (4.10) is valid for any general location of the source and receiver. If the radius of curvature R_{N} goes to infinity, I obtain the traveltime of a wave reflected from a plane interface; if I set $R_{\text{NIP}} = R_{\text{N}}$, I obtain (in the case of the homogeneous overburden) the exact solution for scattered PS waves. In the case $\gamma = 1$, I get the typical multi-parameter traveltime approximation like CRS, MF, n-CRS or i-CRS. Though DSR-PS was derived for a constant velocity overburden, it is applicable for any arbitrary velocity model. In that case, the wavefield attributes (α , R_{NIP} and R_{N}) lose their clear geometrical interpretation and become effective parameters.

4.2.5 CRS stacking operator for converted waves

The common-offset (CO) CRS stacking operator is commonly used to properly stack the converted PS reflections (Bergler et al., 2002). The CO CRS operator includes five stacking parameters and two a priori known near-surface velocities (Zhang et al., 2001). With the DSR-PS stacking operator it is possible to obtain an alternative CRS-type stacking operator for PS converted waves.

Indeed, using the Taylor series expansion of (4.10) and omitting the terms of higher order than the second I get the CRS-type formula (CRS-PS) for converted waves in γ -CMP coordinates (see Appendix D.3):

$$t^2(\tilde{m}, \tilde{h}) = \left[t_0 + \tilde{w} \tilde{m} \right]^2 + 2t_0 \left[\tilde{N} \tilde{m}^2 + \gamma \tilde{M} \tilde{h}^2 \right]. \quad (4.12)$$

¹Here and later, "DSR-PS" means "explicit DSR stacking operator for converted waves".

The CRS-PS stacking operator is identical to the ZO CRS expression (1.16) in the standard CMP coordinates and it reduces to ZO CRS in the case of monotypic waves. If the standard CMP coordinates are substituted in (4.12), I obtain the same five parameter expression that was derived by Vanelle et al. (2012b). It is also formally identical with the CO CRS of Zhang et al. (2001), but uses the same three parameters as ZO CRS.

As will be discussed later, CRS-PS (4.12) is a crucial element to establish the pragmatic search of wavefield attributes for converted waves.

4.2.6 n-CRS stacking operator for converted waves

As in the case of monotypic waves, the n-CRS stacking operator for converted waves (n-CRS-PS) may be obtained from the DSR stacking operator (see Appendix D.4). The 2D n-CRS-PS stacking operator reads:

$$t(m, h) = \sqrt{\left[\frac{1}{1+\gamma} \sqrt{\tilde{F}(\tilde{m} - \gamma\tilde{h})} + \frac{\gamma}{1+\gamma} \sqrt{\tilde{F}(\tilde{m} + \tilde{h})} \right]^2 + 2t_0\gamma(\tilde{M} - \tilde{N})\tilde{h}^2} \quad (4.13)$$

where

$$\tilde{F}(\tilde{m}) = (t_0 + \tilde{w}\tilde{m})^2 + 2t_0\tilde{N}\tilde{m}^2. \quad (4.14)$$

2D n-CRS-PS coincide with 2D DSR-PS in the point diffractor limit and with 2D CRS-PS in the plane-reflector limit. In the case of monotypic waves 2D n-CRS-PS reduces to the conventional n-CRS stacking operator (1.32).

4.2.7 Extension to the 3D case

In the 3D case, \tilde{m} and \tilde{h} become two-dimensional vectors $\tilde{\mathbf{m}}$ and $\tilde{\mathbf{h}}$. The parameter \tilde{w} , corresponding to the first-order derivative of traveltime with respect to \tilde{m} , transforms to the two-dimensional vector $\tilde{\mathbf{w}}$, and the second-order derivatives \tilde{M} and \tilde{N} transform to the symmetric 2×2 matrices $\tilde{\mathbf{M}}$ and $\tilde{\mathbf{N}}$. The parameters $\tilde{\mathbf{w}}$, $\tilde{\mathbf{M}}$ and $\tilde{\mathbf{N}}$ are related to the kinematic wavefield attributes as follows:

$$\tilde{\mathbf{w}} = -\frac{2 \sin \alpha}{v_{PS}} \begin{pmatrix} \cos \beta \\ \sin \beta \end{pmatrix}, \quad \tilde{\mathbf{M}} = \frac{1}{v_{PS}} \mathbf{R} \mathbf{K}_{\text{NIP}} \mathbf{R}^T, \quad \tilde{\mathbf{N}} = \frac{1}{v_{PS}} \mathbf{R} \mathbf{K}_{\text{N}} \mathbf{R}^T. \quad (4.15)$$

Extension of the DSR-PS, CRS-PS and n-CRS-PS stacking operators to the 3D case is straightforward:

- the 3D DSR-PS stacking operator:

$$t(\tilde{\mathbf{m}}, \tilde{\mathbf{h}}) = \frac{1}{1+\gamma} \sqrt{\left[t_0 + \tilde{\mathbf{w}}^T \Delta \mathbf{x}_s \right]^2 + 2t_0 \left[\tilde{\mathbf{m}}^T \tilde{\mathbf{N}} \tilde{\mathbf{m}} - 2\tilde{\mathbf{m}}^T \tilde{\mathbf{N}} (\gamma \tilde{\mathbf{h}}) + (\gamma \tilde{\mathbf{h}})^T \tilde{\mathbf{M}} (\gamma \tilde{\mathbf{h}}) \right]} + \frac{\gamma}{1+\gamma} \sqrt{\left[t_0 + \tilde{\mathbf{w}}^T \Delta \mathbf{x}_g \right]^2 + 2t_0 \left[\tilde{\mathbf{m}}^T \tilde{\mathbf{N}} \tilde{\mathbf{m}} + 2\tilde{\mathbf{m}}^T \tilde{\mathbf{N}} \tilde{\mathbf{h}} + \tilde{\mathbf{h}}^T \tilde{\mathbf{M}} \tilde{\mathbf{h}} \right]}, \quad (4.16)$$

- the 3D CRS-PS stacking operator:

$$t^2(\tilde{\mathbf{m}}, \tilde{\mathbf{h}}) = \left[t_0 + \tilde{\mathbf{w}}^T \tilde{\mathbf{m}} \right]^2 + 2t_0 \left[\tilde{\mathbf{m}}^T \tilde{\mathbf{N}} \tilde{\mathbf{m}} + \gamma \tilde{\mathbf{h}}^T \tilde{\mathbf{M}} \tilde{\mathbf{h}} \right]. \quad (4.17)$$

- the 3D n-CRS-PS stacking operator:

$$t(\tilde{\mathbf{m}}, \tilde{\mathbf{h}}) = \sqrt{\left[\frac{1}{1+\gamma} \sqrt{\tilde{\mathbf{F}}(\tilde{\mathbf{m}} - \gamma \tilde{\mathbf{h}})} + \frac{\gamma}{1+\gamma} \sqrt{\tilde{\mathbf{F}}(\tilde{\mathbf{m}} + \tilde{\mathbf{h}})} \right]^2 + 2t_0 \gamma \tilde{\mathbf{h}}^T (\tilde{\mathbf{M}} - \tilde{\mathbf{N}}) \tilde{\mathbf{h}}} \quad (4.18)$$

where

$$\tilde{\mathbf{F}}(\tilde{\mathbf{m}}) = (t_0 + \tilde{\mathbf{w}}^T \tilde{\mathbf{m}})^2 + 2t_0 \tilde{\mathbf{m}}^T \tilde{\mathbf{N}} \tilde{\mathbf{m}}. \quad (4.19)$$

Note that in the case of monotypic waves ($\gamma = 1$), the 3D DSR-PS stacking operator (4.16) is identical to the explicit 3D DSR stacking operator (2.36), the 3D CRS-PS stacking operator (4.17) is identical to the 3D CRS stacking operator (1.19) and the 3D n-CRS-PS stacking operator (4.18) is identical to the 3D n-CRS stacking operator (2.38).

4.3 Accuracy and implementation

In this section, I provide insight into the accuracy and the range of applicability of the new stacking operators. I begin with simple models like the constant velocity and the constant vertical gradient overburden over a circular reflector to demonstrate the accuracy of the traveltimes approximations and the coefficient determination. Using a more complex synthetic data set I show that the new traveltimes approximations also lead to high quality stack results.

4.3.1 Accuracy of the stacking operators for converted waves

Consider the model from Figure 4.1c with a circular reflector under a homogeneous overburden. For the monotypic reflections, the reflection point can be found by evaluating the roots of a fourth-order equation (Landa et al., 2010). For the converted waves, the exact solution requires solving a sixth-order algebraic equation (see Appendix E). I calculated

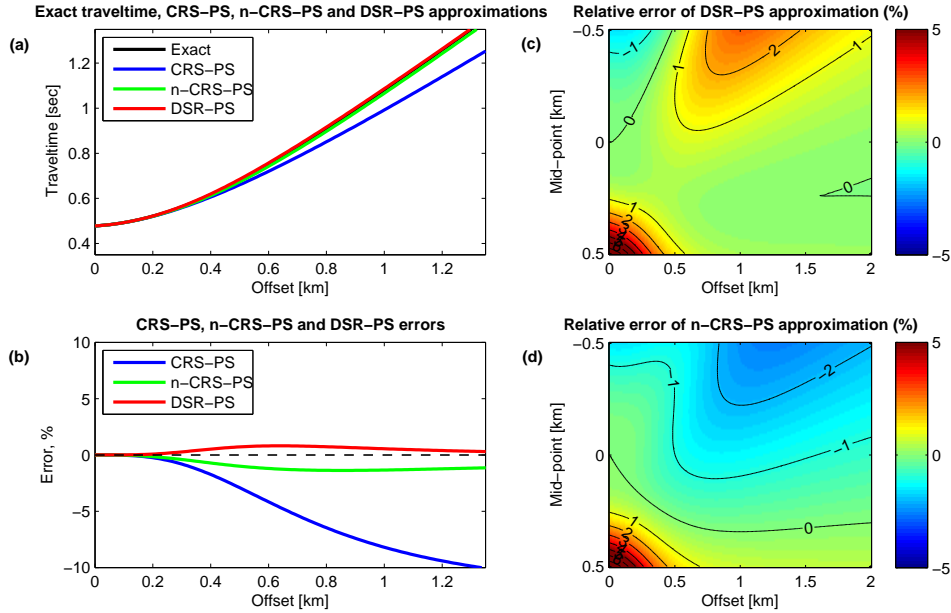


Figure 4.3: Accuracy of the stacking operators for converted waves. (a) Comparison of the reference traveltimes (black), CRS-PS (blue), n-CRS-PS (green) and DSR-PS (red) approximations. (b) Relative errors of the CRS-PS (blue), n-CRS-PS (green), and DSR-PS (red) approximations. Relative traveltimes errors of the DSR-PS (c) and n-CRS-PS (d) approximations.

Table 4.1: Parameters of the constant velocity model

Parameter	Value
α	30°
R_{NIP}	0.5 km
R_{N}	1.0 km
v_P	2.5 km/s
v_S	1.8 km/s

such solutions as reference traveltimes. For the accuracy studies I used a model with parameters listed in Table 4.1.

The accuracy of the DSR-PS and n-CRS-PS approximations can be compared not only with the reference traveltimes, but as well with the CRS approximation. The resulting DSR-PS, CRS-PS, n-CRS-PS approximations and the reference traveltimes in a (standard) CMP gather with a maximum offset of 1.35 km are presented in Figure 4.3a. These traveltimes approximations are compared to the reference traveltimes in Figure 4.3b, where relative errors are shown. I observe that both DSR-PS and n-CRS-PS approximations exhibit smaller errors for large offsets than the conventional CRS-PS.

For the CRS geometry, the resulting relative errors of the DSR-PS and n-CRS-PS approximations are shown in Figures 4.3c-d. In most regions, the error is less than 2%.

For the further tests, I will only use the DSR-PS approximation.

4.3.2 Pragmatic search strategy for converted waves

The stacking procedure consists of evaluating a measure of the coherency of the multi-coverage data along the traveltimes surfaces given by the DSR-PS operator (4.10) (or n-CRS-PS operator) for any possible combination of the wavefield parameters. The determination of the global maximum of the coherency turns out to be time consuming in a three-parametric search strategy. Therefore, I propose a pragmatic search strategy that helps to split the three-parametric search problem into four one-parametric searches and an optional three-parametric local optimization.

The CRS stack approach determines optimal values of wavefield attributes for a known near-surface velocity. For converted waves I additionally require that the near-surface velocity ratio is known. Using the CRS-PS stacking operator (4.12) I can formulate a pragmatic approach for converted waves similar to the one suggested by Müller (1999). It consists of the following steps:

- Step 1. Automatic γ -CMP search with $\tilde{m} = 0$:

$$t_{\gamma\text{-CMP}}^2 = t_0^2 + \frac{2t_0\gamma q}{v_{PS}}\tilde{h}^2, \quad q = \frac{\cos^2 \alpha}{R_{\text{NIP}}}. \quad (4.20)$$

Output: ZO section, combined parameter q .

- Step 2. Plane wave search in the γ -CMP stacked section with $\tilde{h} = 0$:

$$t_{\gamma\text{-PW}} = t_0 - \frac{2 \sin \alpha}{v_{PS}}\tilde{m}. \quad (4.21)$$

Output: emergence angle α .

- Step 3. Repeated γ -CMP search with $\tilde{m} = 0$. Fromm et al. (1985) showed that the traveltimes of converted waves expanded into a power series comprise terms of third order that depend on the emergence angle and R_{NIP} . Due to this fact, the determination of R_{NIP} from the combined parameter q and the angle α is not an accurate procedure. For these reasons an additional R_{NIP} search is required:

$$t = \frac{1}{1 + \gamma} \sqrt{\left[t_0 + \frac{2 \sin \alpha}{v_{PS}}(\gamma \tilde{h}) \right]^2 + \frac{2t_0 \cos^2 \alpha}{v_{PS} R_{\text{NIP}}}(\gamma \tilde{h})^2} \quad (4.22)$$

$$+ \frac{\gamma}{1 + \gamma} \sqrt{\left[t_0 - \frac{2 \sin \alpha}{v_{PS}}\tilde{h} \right]^2 + \frac{2t_0 \cos^2 \alpha}{v_{PS} R_{\text{NIP}}}\tilde{h}^2} \quad (4.23)$$

Output: radius of NIP wave R_{NIP} .

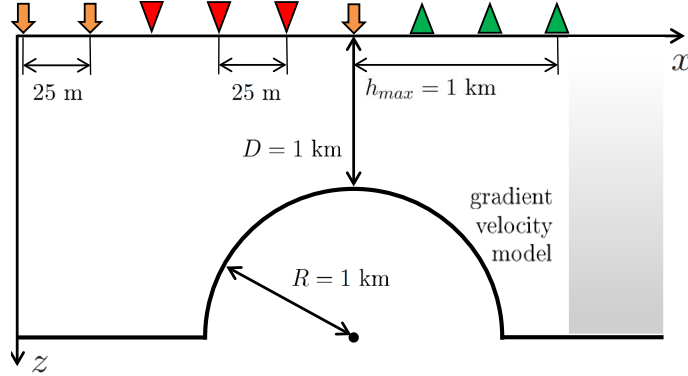


Figure 4.4: Illustration of the model with a constant vertical velocity gradient and a circular reflector.

- Step 4. Hyperbolic search in the ZO section with $\tilde{h} = 0$:

$$t_{\gamma\text{-HY}}^2 = \left[t_0 - \frac{2 \sin \alpha}{v_{PS}} \tilde{m} \right]^2 + \frac{2 t_0 \cos^2 \alpha}{v_{PS} R_N} \tilde{m}^2. \quad (4.24)$$

Output: radius of normal wave R_N .

After the determination of the wavefield attributes (α , R_{NIP} , R_N) the local optimization is carried out with the DSR-PS stacking operator (4.10). The final ZO section from the multi-coverage data is then constructed for the attributes of this optimization.

4.3.3 Accuracy of the wavefield attributes

In order to investigate the accuracy of the determined wavefield attributes, I choose a medium with a constant vertical velocity gradient, $v_P = v_0 + \kappa z$ and constant v_P/v_S ratio. The reflector is a circle with radius R and top at the depth D (see Figure 4.4).

The reflected PP and the converted PS wavefields were generated in Seismic Unix with the routines *susynlv* and *susynlvcw*, respectively. In order to make the data more realistic the seismic noise was added to all traces. The parameters of the datasets are summarized in Table 4.2.

The reference solutions for the wavefield attributes were generated by a numerical determination of the reflection and conversion points and a subsequent evaluation of results given in Vanelle (2002). Figure 4.5 illustrates the semblance, the emergence angle, R_{NIP} , $K_N = 1/R_N$ for PP as well as PS reflections, and in comparison to the reference values. The effective wavefield attributes display a similar behavior in comparison to the exact values. They may be used in NIP-wave tomography for converted waves (Vanelle and Gajewski, 2009).

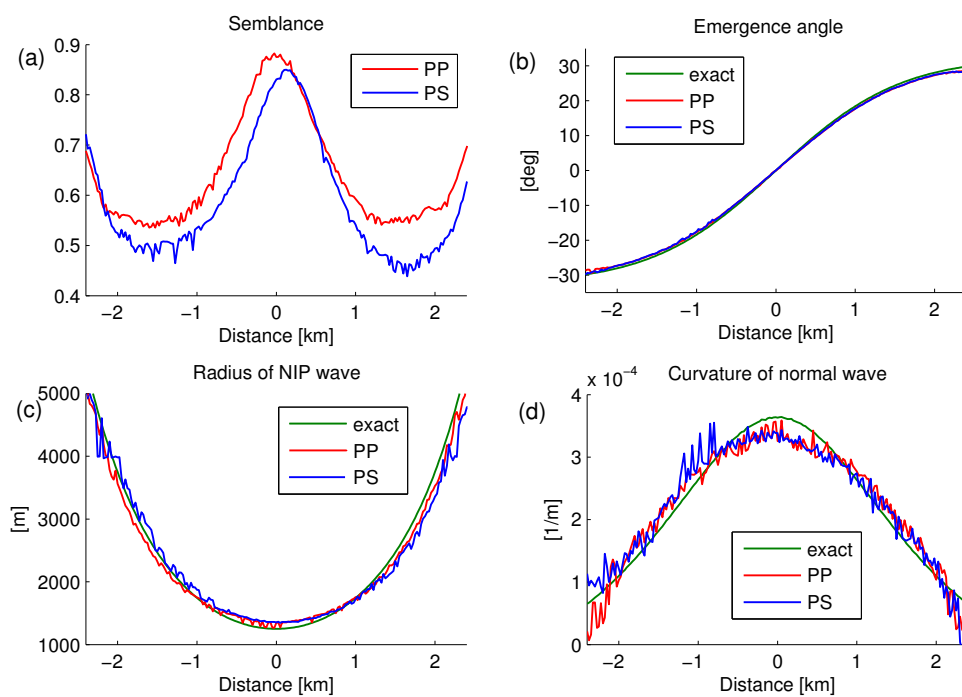


Figure 4.5: Semblance (a) and effective wavefield attributes (b)-(d), derived from converted (blue) and monotypic (red) waves by applying the DSR-PS operator. The effective wavefield attributes display a similar behavior in comparison to the exact values (green). The asymmetry in the semblance (a) may be explained by the asymmetry of the survey.

Table 4.2: Parameters of the constant-gradient velocity model

Parameter	Value
Near-surface velocity v_0	2.0 km/s
Vertical gradient κ	1.0 s^{-1}
v_P/v_S ratio γ	1.4
Radius of reflector R	1.0 km
Depth of reflector D	1.0 km
Number of CMPs	201
CMP sampling interval	25 m
CMP fold	81
Offset sampling interval	25 m
Signal to noise ratio	5.0

4.3.4 Complex synthetic data example

Finally, I have applied the DSR-PS stacking operator to a complex synthetic dataset. The NORSAR ray tracing package was used to generate synthetic seismograms for the model shown in Figure 4.6. The resulting PP and PS-stacked sections in Figure 4.7 exhibit similar quality. PS section can be interpreted on their own or together with P-wave sections. Events seen on one section are not seen on the other. Due to the asymmetry of the PS ray paths and stronger PS impedance contrast, I observe a better illumination of the distant part of the top reflector in the PS than in the PP stack. I conclude that joint interpretation of PP- and PS-stacked data using the DSR-PS/n-CRS-PS operators allow for a better understanding of the subsurface structure.

4.4 Conclusions

In this chapter I have investigated the extension of the DSR-based stacking operators for the case of converted waves. I have presented the new DRS-based traveltime expressions, the DSR-PS and n-CRS-PS approximations, for converted waves reflected from the curved interfaces. These approximations are natural generalizations of the earlier introduced explicit DSR and conventional n-CRS stacking operators. For converted waves the new operators are highly accurate.

Furthermore, I have found a CRS-type expression for converted waves. This hyperbolic operator is expressed in the γ -CMP coordinates and allows for a pragmatic search strategy for converted waves. Taken together, these findings provide a powerful and efficient tool for constructing the PS-stacked sections.

The most important limitation of this work is the assumption of the constant v_P/v_S ratio. Although this assumption does not hold in the "real world", it appears to be quite reasonable, because the variation of γ in most of rocks is limited. The assumption

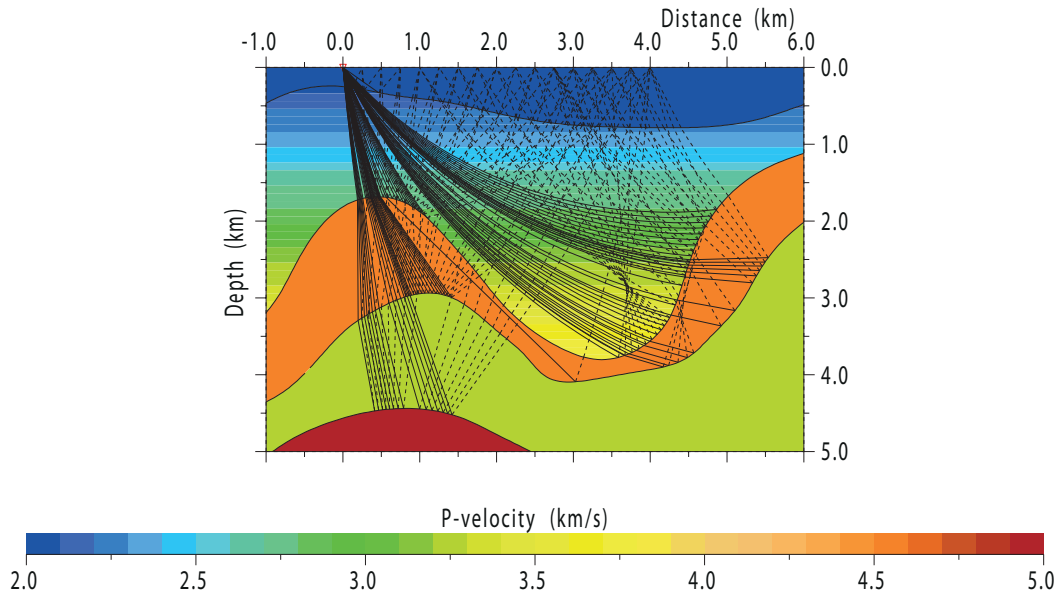


Figure 4.6: Complex velocity model consisting of a homogeneous low velocity near-surface layer, a second layer with a gradient velocity and three underlying constant velocity layers. The v_p/v_s ratio is $\gamma = 1.73$ in the near-surface layer and $\gamma = 1.80$ in the remaining model parts.

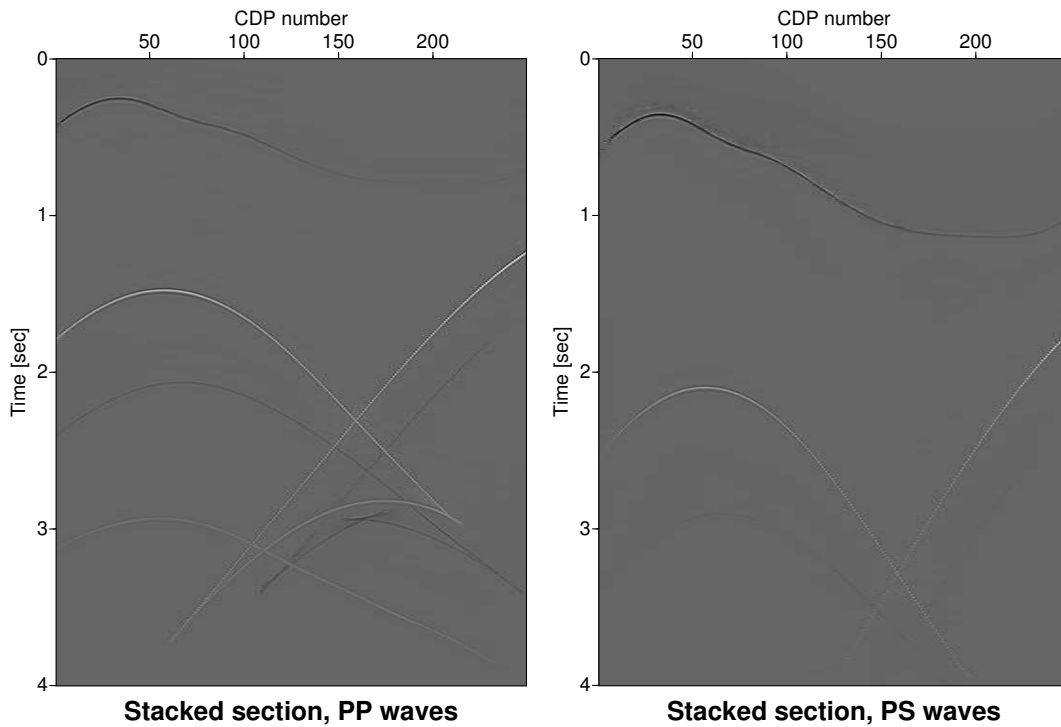


Figure 4.7: Stacked sections for PP (left) and PS (right) waves. Note the continuity of the top reflector in the PS section resulting from the asymmetric ray paths.

of the constant γ is not necessarily a restriction, because even in the case of the complex model with the non-constant value of γ , the proposed DSR-PS stacking operator provides high-quality PS images.

Monotypic and converted waves image different parts of the reflector because of the asymmetry of ray paths of converted waves and the difference in P- and S-wave impedance. The obtained PP and PS images and the corresponding wavefield attributes may be jointly interpreted to derive the true model of the subsurface. Hence, I believe that this work could be the starting point for stacking converted waves with the DSR-based stacking operators. However, further studies, which take the variation of γ into account and investigate the application of the method to field data, will need to be performed.

Chapter 5

Common-offset DSR stacking operator

“Is every accident just a higher-order design?”

– Terry Pratchett, *Night Watch*

In the previous chapters, I used a model-based approach to derive the DSR-based stacking operators. Another commonly used approach is based on the paraxial ray theory. The paraxial ray theory is valid for an arbitrary velocity model and, hence, the traveltime expressions, obtained from this theory, are considered to be velocity model independent.

In this chapter, based on paraxial ray theory, I obtain the DSR stacking operator for the most general common-offset (CO) case. This expression extends the range of applicability of the DSR stacking operators and demonstrates their close relationship with the standard CRS stacking operators. For a number of special cases, I find a good agreement with the previously obtained results.

5.1 Introduction

Seismic ray theory provides the trajectories of seismic rays as well as the kinematic and dynamic attributes along the ray. These dynamic attributes enable to predict the properties of rays in the paraxial vicinity of the reference (central) ray. The properties of these paraxial rays are determined by the surface-to-surface propagator matrix ([Červený, 2001](#)).

[Bortfeld \(1989\)](#) derived a parabolic approximation for the traveltime of a reflected paraxial ray that propagates in the so-called seismic system: a structure of homogeneous layers with curved continuous boundaries. [Hubral et al. \(1992\)](#) proved that the same traveltime

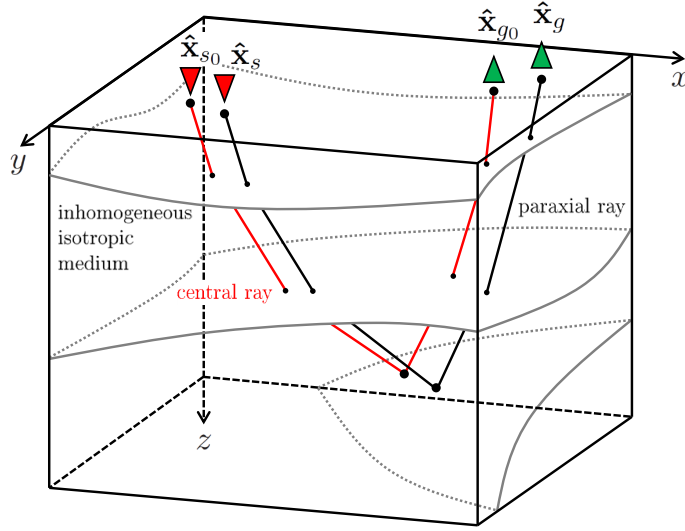


Figure 5.1: Illustration of the common-offset reflection experiment. The subsurface consists of inhomogeneous isotropic layers with smooth continuous interfaces.

approximation is valid in the inhomogeneous isotropic medium. Moser and Červený (2007) formulated the paraxial ray theory for the general anisotropic case. They argue, that even in an anisotropic inhomogeneous layered medium, the parabolic traveltime approximation of Bortfeld remains correct.

The hyperbolic traveltime approximations better fit the traveltime of reflected waves, than the parabolic approximations (Ursin, 1982; Mann et al., 1999). These hyperbolic traveltime approximations (e.g., CO CRS) are derived from parabolic approximations (Schleicher et al., 1993; Zhang et al., 2001). In this chapter, I show that it is possible to obtain a DSR stacking operator from the parabolic traveltime approximation of Bortfeld.

This chapter is structured as follows. Section 5.2 introduces the required notation and discusses the statement of the problem. I show how the parabolic traveltime approximation is derived from Hamilton's equation and paraxial ray theory. In Section 5.3 I discuss the link between the submatrices of the propagator matrix and the curvatures of wavefronts. This link allows me to split the terms of the parabolic traveltime formula in two groups and to present the traveltime in DSR form (CO DSR approximation). Section 5.4 investigates the relation between the new CO DSR stacking operator and the DSR operators, derived in the previous chapters. For this reason, I consider several special cases: a monotypic reflected wave in the ZO experiment, a converted reflected wave in the ZO experiment, and a diffracted wave in the CO experiment. In the conclusion 5.5 of this chapter I summarize the results and discuss the applicability of the DSR stacking operators to anisotropic media.

5.2 Traveltime approximation from paraxial ray theory

In this section I briefly review the basics of the paraxial ray theory and the traveltime approximation obtained from this theory.

Consider the central ray emitted from the source and, after reflection from the curved interface, recorded by the receiver (see Figure 5.1). In the general (common-offset) case, the source and the receiver locations do not necessarily coincide. Let me denote the traveltime along the central ray by t_0 . The question is, what is the traveltime t of the paraxial ray in the vicinity of the central ray?

Let me now introduce the notations necessary to formalize the problem. As discussed previously, in order to show the difference between 2D and 3D vectors, the 3D vectors are marked with a hat (e.g., $\hat{\mathbf{x}}_s$) while their horizontal projections do not have the hat (e.g., \mathbf{x}_s). In the following:

- $\hat{\mathbf{x}}_{s_0}$ and $\hat{\mathbf{x}}_{g_0}$ are the source and the receiver locations of the central ray;
- \mathbf{x}_0 and \mathbf{h}_0 are the midpoint and the half-offset of the central ray:

$$\mathbf{x}_0 = \frac{1}{2}(\mathbf{x}_{g_0} + \mathbf{x}_{s_0}), \quad \mathbf{h}_0 = \frac{1}{2}(\mathbf{x}_{g_0} - \mathbf{x}_{s_0}); \quad (5.1)$$

- $\hat{\mathbf{x}}_s$ and $\hat{\mathbf{x}}_g$ are the source and the receiver locations of the paraxial ray;
- \mathbf{x}_m and \mathbf{h}_m are the midpoint and the half-offset of the paraxial ray:

$$\mathbf{x}_m = \frac{1}{2}(\mathbf{x}_g + \mathbf{x}_s), \quad \mathbf{h}_m = \frac{1}{2}(\mathbf{x}_g - \mathbf{x}_s); \quad (5.2)$$

- $\Delta\mathbf{x}_s$ and $\Delta\mathbf{x}_g$ are the source and the receiver displacements:

$$\Delta\hat{\mathbf{x}}_s = \hat{\mathbf{x}}_s - \hat{\mathbf{x}}_{s_0}, \quad \Delta\hat{\mathbf{x}}_g = \hat{\mathbf{x}}_g - \hat{\mathbf{x}}_{g_0}; \quad (5.3)$$

- \mathbf{m} and \mathbf{h} are the midpoint and the half-offset displacements:

$$\begin{aligned} \mathbf{m} &= \mathbf{x}_m - \mathbf{x}_0 = \frac{1}{2}(\Delta\mathbf{x}_g + \Delta\mathbf{x}_s), \\ \mathbf{h} &= \mathbf{h}_m - \mathbf{h}_0 = \frac{1}{2}(\Delta\mathbf{x}_g - \Delta\mathbf{x}_s); \end{aligned} \quad (5.4)$$

- $\hat{\mathbf{p}}_{s_0}$ and $\hat{\mathbf{p}}_{g_0}$ are the slowness vectors of the central ray at the position of source and receiver;
- $\hat{\mathbf{p}}_s$ and $\hat{\mathbf{p}}_g$ are the slowness vectors of the paraxial ray at the position of source and receiver, and
- $\Delta\hat{\mathbf{p}}_s$ and $\Delta\hat{\mathbf{p}}_g$ are the deviations of the slowness vectors at the source and the receiver:

$$\Delta\hat{\mathbf{p}}_s = \hat{\mathbf{p}}_s - \hat{\mathbf{p}}_{s_0}, \quad \Delta\hat{\mathbf{p}}_g = \hat{\mathbf{p}}_g - \hat{\mathbf{p}}_{g_0}. \quad (5.5)$$

It is assumed that all source-receiver pairs are located on the measurement surface $z = 0$, and that the subsurface is an inhomogeneous isotropic layered medium with continuous curved reflectors.

With these notations I can find the traveltime of a paraxial ray t . According to Hamilton's equation (see e.g., [Bortfeld, 1989](#)) the differential dt of the traveltime of reflected wave is equal:

$$dt = \hat{\mathbf{p}}_g^T d\hat{\mathbf{x}}_g - \hat{\mathbf{p}}_s^T d\hat{\mathbf{x}}_s. \quad (5.6)$$

Since the vertical components of the displacement vectors (5.3) are equal to zero, the traveltime difference (5.6) depends only on two-component horizontal projections:

$$dt = \mathbf{p}_g^T d\mathbf{x}_g - \mathbf{p}_s^T d\mathbf{x}_s. \quad (5.7)$$

The paraxial ray theory (see, e.g., [Hubral, 1983](#); [Červený, 2001](#)) establishes the linear relationship between the displacements and the deviations of the slowness vectors at the source and the receiver:

$$\begin{pmatrix} \Delta\mathbf{x}_g \\ \Delta\mathbf{p}_g \end{pmatrix} = \bar{\bar{\mathbf{T}}} \begin{pmatrix} \Delta\mathbf{x}_s \\ \Delta\mathbf{p}_s \end{pmatrix}. \quad (5.8)$$

This relation is set up by the 4×4 surface-to-surface ray propagator matrix for the central ray:

$$\bar{\bar{\mathbf{T}}} = \begin{pmatrix} \mathbf{A} & \mathbf{B} \\ \mathbf{C} & \mathbf{D} \end{pmatrix}, \quad (5.9)$$

that consists of four 2×2 submatrices: \mathbf{A} , \mathbf{B} , \mathbf{C} and \mathbf{D} . The propagator matrix $\bar{\bar{\mathbf{T}}}$ has several important properties, including, among others, symplecticity (see e.g., [Červený, 2001](#)). Hence, there is an additional condition for these submatrices:

$$\mathbf{A}\mathbf{D}^T - \mathbf{B}\mathbf{C}^T = \mathbf{I}. \quad (5.10)$$

where \mathbf{I} is the identity matrix. The linear relationship (5.8) may be solved to get \mathbf{p}_s and \mathbf{p}_g :

$$\mathbf{p}_s = \mathbf{p}_{s_0} + \mathbf{B}^{-1}\Delta\mathbf{x}_g - \mathbf{B}^{-1}\mathbf{A}\Delta\mathbf{x}_s, \quad (5.11a)$$

$$\mathbf{p}_g = \mathbf{p}_{g_0} + \mathbf{C}\Delta\mathbf{x}_s + \mathbf{D}\mathbf{B}^{-1}\Delta\mathbf{x}_g - \mathbf{D}\mathbf{B}^{-1}\mathbf{A}\Delta\mathbf{x}_s. \quad (5.11b)$$

Substitution of (5.11) into (5.7), together with the symplecticity property (5.10) and integration yield the *parabolic traveltime approximation* for a paraxial ray:

$$t(\Delta\mathbf{x}_s, \Delta\mathbf{x}_g) = t_0 + \mathbf{p}_{g_0}^T \Delta\mathbf{x}_g - \mathbf{p}_{s_0}^T \Delta\mathbf{x}_s - \Delta\mathbf{x}_s^T \mathbf{B}^{-1} \Delta\mathbf{x}_g + \frac{1}{2} \Delta\mathbf{x}_s^T \mathbf{B}^{-1} \mathbf{A} \Delta\mathbf{x}_s + \frac{1}{2} \Delta\mathbf{x}_g^T \mathbf{D} \mathbf{B}^{-1} \Delta\mathbf{x}_g. \quad (5.12)$$

This formula was originally obtained by [Bortfeld \(1989\)](#) for a homogeneous layered medium and later extended by [Hubral et al. \(1992\)](#) to inhomogeneous isotropic media. Further investigations showed that the same parabolic traveltime approximation remains valid even in a general inhomogeneous anisotropic medium (see [Moser and Červený, 2007](#), eq. 72).

In practice, it is common to work in the midpoint-offset coordinates. The parabolic travelttime approximation (5.12) in the midpoint-offset coordinates reads:

$$t(\mathbf{m}, \mathbf{h}) = t_0 + \mathbf{p}_{g_0}^T \Delta \mathbf{x}_g - \mathbf{p}_{s_0}^T \Delta \mathbf{x}_s + \mathbf{m}^T (\mathbf{D}\mathbf{B}^{-1} - \mathbf{B}^{-1}\mathbf{A})\mathbf{h} + \frac{1}{2} \mathbf{h}^T (\mathbf{B}^{-1}\mathbf{A} + \mathbf{D}\mathbf{B}^{-1} + 2\mathbf{B}^{-1})\mathbf{h} + \frac{1}{2} \mathbf{m}^T (\mathbf{B}^{-1}\mathbf{A} + \mathbf{D}\mathbf{B}^{-1} - 2\mathbf{B}^{-1})\mathbf{m}. \quad (5.13)$$

The *hyperbolic travelttime approximation* can be immediately obtained by squaring both sides of the parabolic travelttime formula (5.13) and neglecting the terms of higher order than the second (Zhang et al., 2001):

$$t^2(\mathbf{m}, \mathbf{h}) = \left[t_0 + \mathbf{p}_{g_0}^T \Delta \mathbf{x}_g - \mathbf{p}_{s_0}^T \Delta \mathbf{x}_s \right]^2 + 2t_0 \left[\mathbf{m}^T (\mathbf{D}\mathbf{B}^{-1} - \mathbf{B}^{-1}\mathbf{A})\mathbf{h} + \frac{1}{2} \mathbf{h}^T (\mathbf{B}^{-1}\mathbf{A} + \mathbf{D}\mathbf{B}^{-1} + 2\mathbf{B}^{-1})\mathbf{h} + \frac{1}{2} \mathbf{m}^T (\mathbf{B}^{-1}\mathbf{A} + \mathbf{D}\mathbf{B}^{-1} - 2\mathbf{B}^{-1})\mathbf{m} \right]. \quad (5.14)$$

In the next section I shall consider an alternative transformation of the parabolic travelttime formula (5.13) leading to a DSR travelttime expression.

5.3 DSR approximation from paraxial ray theory

The submatrices \mathbf{A} , \mathbf{B} and \mathbf{D} from the parabolic travelttime approximation (5.13) are linked with the wavefront curvatures of the real and the hypothetical waves. These waves are the results of two real (common-shot (CS), common-receiver (CR)) and two hypothetical (common-midpoint (CMP) and common-offset (CO)) experiments (see Figure 5.2). Conventionally, the parabolic travelttime approximation (5.13) is expressed in the curvatures of the CS (\mathbf{K}_{CS}^g) and CMP ($\mathbf{K}_{\text{CMP}}^s, \mathbf{K}_{\text{CMP}}^g$) waves (see, e.g., Müller, 2003). On the contrary, I shall use the curvatures of the CMP ($\mathbf{K}_{\text{CMP}}^s, \mathbf{K}_{\text{CMP}}^g$) and CO ($\mathbf{K}_{\text{CO}}^s, \mathbf{K}_{\text{CO}}^g$) waves.

The link between the wavefront curvatures and the submatrices \mathbf{A} , \mathbf{B} and \mathbf{D} was discussed by Zhang et al. (2001). Müller (2003) also derived similar relations in the 3D case. Table 5.1 summarizes the results obtained in these studies.

Table 5.1: Wavefront curvatures in terms of the elements of the propagator matrix.

Experiment	CS	CMP	CO	CR
$\frac{1}{v_s} \mathbf{R}_s \mathbf{K}_l^s \mathbf{R}_s^T =$	-	$-\mathbf{B}^{-1}(\mathbf{I} + \mathbf{A})$	$\mathbf{B}^{-1}(\mathbf{I} - \mathbf{A})$	$-\mathbf{B}^{-1}\mathbf{A}$
$\frac{1}{v_g} \mathbf{R}_g \mathbf{K}_l^s \mathbf{R}_g^T =$	$\mathbf{D}\mathbf{B}^{-1}$	$(\mathbf{D} + \mathbf{I})\mathbf{B}^{-1}$	$(\mathbf{D} - \mathbf{I})\mathbf{B}^{-1}$	-

As it is apparent from Table 5.1, the curvature of the hypothetical downgoing CMP wave $\mathbf{K}_{\text{CMP}}^s$ at $\hat{\mathbf{x}}_{s_0}$ has the following relation with the submatrices \mathbf{A} and \mathbf{B} :

$$\frac{1}{v_s} \mathbf{R}_s \mathbf{K}_{\text{CMP}}^s \mathbf{R}_s^T = -\mathbf{B}^{-1}(\mathbf{I} + \mathbf{A}). \quad (5.15)$$

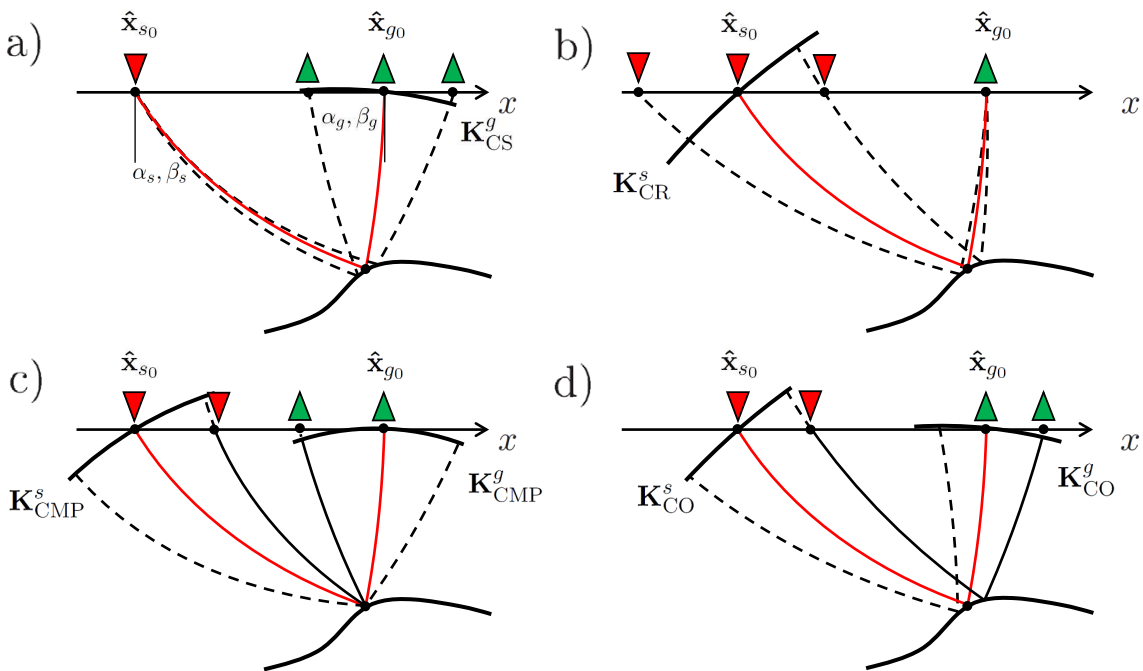


Figure 5.2: Illustration of the different acquisition geometries: a) common-shot, b) common-receiver, c) common-midpoint, and d) common-offset. According to [Hubral and Krey \(1980\)](#) the elements of the curvature matrices are positive/negative if the wavefront is fully behind/ahead its tangent plane. Hence, the wavefront curvatures of the downgoing waves at the source $\hat{\mathbf{x}}_{s_0}$ are negative and the corresponding emerging waves at the receiver $\hat{\mathbf{x}}_{g_0}$ are positive.

Here, v_s is a near-surface velocity at the source location $\hat{\mathbf{x}}_{s_0}$, and \mathbf{R}_s is the upper left (2×2) part of the rotation matrix that accounts for the transformation from the ray-centered to the general Cartesian coordinate system. \mathbf{R}_s is defined by the incidence polar α_s and azimuth β_s angles of the central ray. Quantities v_g , \mathbf{R}_g , α_g , β_g denote corresponding values at the receiver location $\hat{\mathbf{x}}_{g_0}$.

In order to express the traveltime approximation (5.13) in the terms of the curvatures of the CMP and CO waves, I use the following notations:

$$\begin{aligned} \mathbf{M}_s &= \frac{1}{v_s} \mathbf{R}_s \mathbf{K}_{\text{CMP}}^s \mathbf{R}_s^T, & \mathbf{N}_s &= \frac{1}{v_s} \mathbf{R}_s \mathbf{K}_{\text{CO}}^s \mathbf{R}_s^T, \\ \mathbf{M}_g &= \frac{1}{v_g} \mathbf{R}_g \mathbf{K}_{\text{CMP}}^g \mathbf{R}_g^T, & \mathbf{N}_g &= \frac{1}{v_g} \mathbf{R}_g \mathbf{K}_{\text{CO}}^g \mathbf{R}_g^T. \end{aligned} \quad (5.16)$$

Since there is a linear relation:

$$\mathbf{M}_g - \mathbf{N}_g = \mathbf{N}_s - \mathbf{M}_s, \quad (5.17)$$

only three variables among (5.16) are independent.

As it is apparent from Table 5.1, the sum and the difference of the CMP and CO curvatures are equal:

$$\begin{aligned} \mathbf{M}_g - \mathbf{M}_s &= \mathbf{B}^{-1} \mathbf{A} + \mathbf{D} \mathbf{B}^{-1} + 2\mathbf{B}^{-1}, & \mathbf{M}_g + \mathbf{M}_s &= \mathbf{D} \mathbf{B}^{-1} - \mathbf{B}^{-1} \mathbf{A}, \\ \mathbf{N}_g - \mathbf{N}_s &= \mathbf{B}^{-1} \mathbf{A} + \mathbf{D} \mathbf{B}^{-1} - 2\mathbf{B}^{-1}, & \mathbf{N}_g + \mathbf{N}_s &= \mathbf{D} \mathbf{B}^{-1} - \mathbf{B}^{-1} \mathbf{A}. \end{aligned} \quad (5.18)$$

The above equations allow to express the traveltime approximation (5.13) in terms of CMP and CO wavefronts:

$$\begin{aligned} t(\mathbf{m}, \mathbf{h}) &= t_0 + \mathbf{p}_{g_0}^T \Delta \mathbf{x}_g - \mathbf{p}_{s_0}^T \Delta \mathbf{x}_s + \mathbf{m}^T (\eta_1 (\mathbf{M}_g + \mathbf{M}_s) + \eta_2 (\mathbf{N}_g + \mathbf{N}_s)) \mathbf{h} \\ &\quad + \frac{1}{2} \mathbf{h}^T (\mathbf{M}_g - \mathbf{M}_s) \mathbf{h} + \frac{1}{2} \mathbf{m}^T (\mathbf{N}_g - \mathbf{N}_s) \mathbf{m} \end{aligned} \quad (5.19)$$

Since there is no unique representation for the "mixed" term, I used the linear combination of $\mathbf{M}_g + \mathbf{M}_s$ and $\mathbf{N}_g + \mathbf{N}_s$ with the weights η_1 , η_2 :

$$\eta_1 + \eta_2 = 1. \quad (5.20)$$

If I introduce the terms:

$$\mathbf{L}_s = \eta_1 \mathbf{M}_s + \eta_2 \mathbf{N}_s, \quad \mathbf{L}_g = \eta_1 \mathbf{M}_g + \eta_2 \mathbf{N}_g, \quad (5.21)$$

and represent the traveltime of the central ray as a sum of the traveltimes of the incident t_s and the reflected t_g ray segments, I can split the terms in (5.19) in two groups:

$$\begin{aligned} t(\mathbf{m}, \mathbf{h}) &= \underbrace{t_s - \mathbf{p}_{s_0}^T \Delta \mathbf{x}_s - \frac{1}{2} \mathbf{m}^T \mathbf{N}_s \mathbf{m} + \mathbf{m}^T \mathbf{L}_s \mathbf{h} - \frac{1}{2} \mathbf{h}^T \mathbf{M}_s \mathbf{h}}_{\text{source terms}} \\ &\quad + \underbrace{t_g + \mathbf{p}_{g_0}^T \Delta \mathbf{x}_g + \frac{1}{2} \mathbf{m}^T \mathbf{N}_g \mathbf{m} + \mathbf{m}^T \mathbf{L}_g \mathbf{h} + \frac{1}{2} \mathbf{h}^T \mathbf{M}_g \mathbf{h}}_{\text{receiver terms}}. \end{aligned} \quad (5.22)$$

Note that the hyperbolic CO CRS stacking operator can be obtained by squaring (5.22) and neglecting the terms of higher order than the second. Instead, I shall square and neglect the terms of higher order than the second in each group separately. The result is the common-offset DSR stacking operator:

$$t(\mathbf{m}, \mathbf{h}) = \sqrt{\left[t_s - \mathbf{p}_{s_0}^T \Delta \mathbf{x}_s \right]^2 + t_s \left[-\mathbf{m}^T \mathbf{N}_s \mathbf{m} + 2\mathbf{m}^T \mathbf{L}_s \mathbf{h} - \mathbf{h}^T \mathbf{M}_s \mathbf{h} \right]} + \sqrt{\left[t_g + \mathbf{p}_{g_0}^T \Delta \mathbf{x}_g \right]^2 + t_g \left[\mathbf{m}^T \mathbf{N}_g \mathbf{m} + 2\mathbf{m}^T \mathbf{L}_g \mathbf{h} + \mathbf{h}^T \mathbf{M}_g \mathbf{h} \right]}. \quad (5.23)$$

5.4 Special cases

The CO DSR stacking operator (5.23) uses exactly the same wavefield attributes as the CO CRS stacking operator. These attributes are the horizontal projections of the slowness vectors at the source \mathbf{p}_{s_0} and the receiver \mathbf{p}_{g_0} , and four symmetric 2×2 curvature matrices $\mathbf{K}_{\text{CMP}}^s, \mathbf{K}_{\text{CMP}}^g, \mathbf{K}_{\text{CO}}^s, \mathbf{K}_{\text{CO}}^g$ linked by equation (5.17). In total, CO DSR has 13 independent wavefield attributes in the 3D case and 5 independent wavefield attributes in the 2D case. Additionally, CO DSR requires the weights η_1 and η_2 and the traveltimes t_s and t_g . These additional parameters do not allow to formulate an efficient implementation of the CO DSR stacking operator. However, in several special cases, I can get relatively simple traveltimes approximations and compare them with existing results.

5.4.1 Zero-offset, monotopic waves

In the zero-offset case, the incident and the reflected ray coincide, hence:

$$v_s = v_g = v_0, \quad \alpha_s = \alpha_g = \alpha, \quad \beta_s = \beta_g = \beta, \quad t_s = t_g = \frac{t_0}{2}. \quad (5.24)$$

According to Hubral (1983), the curvatures of the CMP waves are equal to the curvature of the fictitious NIP wave and the curvatures of the CO waves are equal to the curvature of the normal wave:

$$\mathbf{K}_{\text{CMP}}^s = -\mathbf{K}_{\text{NIP}}, \quad \mathbf{K}_{\text{CMP}}^g = \mathbf{K}_{\text{NIP}}, \quad \mathbf{K}_{\text{CO}}^s = -\mathbf{K}_{\text{N}}, \quad \mathbf{K}_{\text{CO}}^g = \mathbf{K}_{\text{N}}. \quad (5.25)$$

With this simplifications, CO DSR (5.23) can be expressed in notations \mathbf{w} , \mathbf{M} and \mathbf{N} from (1.20). Indeed,

$$\mathbf{p}_{s_0} = -\frac{\mathbf{w}}{2}, \quad \mathbf{p}_{g_0} = \frac{\mathbf{w}}{2}, \quad \mathbf{M}_s = -\mathbf{M}, \quad \mathbf{M}_g = \mathbf{M}, \quad \mathbf{N}_s = -\mathbf{N}, \quad \mathbf{N}_g = \mathbf{N}. \quad (5.26)$$

and CO DSR transforms to:

$$t(\mathbf{m}, \mathbf{h}) = \frac{1}{2} \sqrt{\left[t_0 + \mathbf{w}^T \Delta \mathbf{x}_s \right]^2 + 2t_0 \left[\mathbf{m}^T \mathbf{N} \mathbf{m} - 2\mathbf{m}^T (\eta_1 \mathbf{M} + \eta_2 \mathbf{N}) \mathbf{h} + \mathbf{h}^T \mathbf{M} \mathbf{h} \right]} + \frac{1}{2} \sqrt{\left[t_0 + \mathbf{w}^T \Delta \mathbf{x}_g \right]^2 + 2t_0 \left[\mathbf{m}^T \mathbf{N} \mathbf{m} + 2\mathbf{m}^T (\eta_1 \mathbf{M} + \eta_2 \mathbf{N}) \mathbf{h} + \mathbf{h}^T \mathbf{M} \mathbf{h} \right]}. \quad (5.27)$$

If I set the weight $\eta_1 = 0$, this formula is identical to the 3D DSR stacking operator (2.36). Hence, I can conclude that in the zero-offset case the "mixed" term is determined only by the curvature of the CO wave.

5.4.2 Zero-offset, converted waves

Similar to Chapter 4, I will only consider the special case of a constant v_P/v_S ratio. In this case the incident and the reflected ray segments still coincide,

$$\alpha_s = \alpha_g = \alpha, \quad \beta_s = \beta_g = \beta, \quad (5.28)$$

however, the traveltimes of the ray segments and the near-surface velocities are different:

$$v_s = v_P, \quad v_g = v_S, \quad t_s = \frac{t_0}{1 + \gamma}, \quad t_g = \frac{\gamma t_0}{1 + \gamma}. \quad (5.29)$$

There is no more connection with the curvatures of the NIP and the normal waves. The DSR-PS formula is expressed in terms of the parameters $\tilde{\mathbf{w}}$, $\tilde{\mathbf{M}}$, $\tilde{\mathbf{N}}$ (4.15):

$$\mathbf{p}_{s_0} = -\frac{\tilde{\mathbf{w}}}{1 + \gamma}, \quad \mathbf{p}_{g_0} = \frac{\gamma \tilde{\mathbf{w}}}{1 + \gamma}, \quad (5.30)$$

$$\begin{aligned} \mathbf{M}_s &= \frac{2}{1 + \gamma} \mathbf{M}_s^*, & \mathbf{M}_g &= \frac{2\gamma}{1 + \gamma} \mathbf{M}_g^*, & \mathbf{M}_i^* &= \frac{1}{v_{PS}} \mathbf{R} \mathbf{K}_{\text{CMP}}^i \mathbf{R}^T, \\ \mathbf{N}_s &= \frac{2}{1 + \gamma} \mathbf{N}_s^*, & \mathbf{N}_g &= \frac{2\gamma}{1 + \gamma} \mathbf{N}_g^*, & \mathbf{N}_i^* &= \frac{1}{v_{PS}} \mathbf{R} \mathbf{K}_{\text{CO}}^i \mathbf{R}^T, \end{aligned} \quad i = s, g. \quad (5.31)$$

where i denotes either the source (s) or the receiver (g). Note, that the difference between \mathbf{M}^* and $\tilde{\mathbf{M}}$, and \mathbf{N}^* and $\tilde{\mathbf{N}}$ is only in the curvature matrix. Substitution of (5.30) and (5.31) into (5.23) gives:

$$\begin{aligned} t(\mathbf{m}, \mathbf{h}) &= \frac{1}{1 + \gamma} \sqrt{\left[t_0 + \tilde{\mathbf{w}}^T \Delta \mathbf{x}_s \right]^2 + 2t_0 \left[-\mathbf{m}^T \mathbf{N}_s^* \mathbf{m} + 2\mathbf{m}^T \mathbf{N}_s^* \mathbf{h} - \mathbf{h}^T \mathbf{M}_s^* \mathbf{h} \right]} \\ &\quad + \frac{\gamma}{1 + \gamma} \sqrt{\left[t_0 + \tilde{\mathbf{w}}^T \Delta \mathbf{x}_g \right]^2 + 2t_0 \left[\mathbf{m}^T \mathbf{N}_g^* \mathbf{m} + 2\mathbf{m}^T \mathbf{N}_g^* \mathbf{h} + \mathbf{h}^T \mathbf{M}_g^* \mathbf{h} \right]}. \end{aligned} \quad (5.32)$$

This expression is formally identical to the 3D DSR-PS stacking operator in standard CMP coordinates (D.36) (see Appendix D.5 for more details). A coefficient comparison in (5.32) and (D.36) establishes the link between the curvatures of the CMP and the CO waves and the curvatures of the NIP and the normal waves. As expected, the curvatures of CO experiment at the source and the receiver are equal to the curvature of the normal wave:

$$\mathbf{K}_{\text{CO}}^s = -\mathbf{K}_N, \quad \mathbf{K}_{\text{CO}}^g = \mathbf{K}_N, \quad (5.33)$$

and the curvatures of the CMP experiment are different:

$$\begin{aligned} \mathbf{K}_{\text{CMP}}^s &= -\left[\mathbf{K}_N + \left(\frac{2\gamma}{1 + \gamma} \right)^2 (\mathbf{K}_{\text{NIP}} - \mathbf{K}_N) \right], \\ \mathbf{K}_{\text{CMP}}^g &= \left[\mathbf{K}_N + \left(\frac{2}{1 + \gamma} \right)^2 (\mathbf{K}_{\text{NIP}} - \mathbf{K}_N) \right]. \end{aligned} \quad (5.34)$$

5.4.3 Common-offset, diffractions

In the case of a point diffractor, the curvatures of the CMP and CO waves coincide and become equal to the curvature of the NIP wave:

$$\mathbf{K}_{\text{CMP}}^s = -\mathbf{K}_{\text{NIP}}^s, \quad \mathbf{K}_{\text{CMP}}^g = \mathbf{K}_{\text{NIP}}^g, \quad \mathbf{K}_{\text{CO}}^s = -\mathbf{K}_{\text{NIP}}^s, \quad \mathbf{K}_{\text{CO}}^g = \mathbf{K}_{\text{NIP}}^g. \quad (5.35)$$

The CO DSR stacking operator (5.23) in this case simplifies to:

$$t(\mathbf{m}, \mathbf{h}) = \sqrt{\left[t_s - \mathbf{p}_{s_0}^T \Delta \mathbf{x}_s\right]^2 + \frac{t_s}{v_s} \left[\Delta \mathbf{x}_s^T \mathbf{R}_s \mathbf{K}_{\text{NIP}}^s \mathbf{R}_s^T \Delta \mathbf{x}_s\right]} + \sqrt{\left[t_g + \mathbf{p}_{g_0}^T \Delta \mathbf{x}_g\right]^2 + \frac{t_g}{v_g} \left[\Delta \mathbf{x}_g^T \mathbf{R}_g \mathbf{K}_{\text{NIP}}^g \mathbf{R}_g^T \Delta \mathbf{x}_g\right]}. \quad (5.36)$$

If I expand the square roots of (5.36), I obtain the same parabolic stacking operator, as used by Bauer et al. (2015) to enhance the diffraction events. Hence, the DSR formula (5.36) may be used for diffraction imaging in the CO domain in the similar way as it was presented by Bauer et al. (2016a).

5.4.4 Anisotropic media

Moser and Červený (2007) proved that the original parabolic traveltime approximation (5.13) is valid in the inhomogeneous anisotropic medium. Hence, I can argue that the DSR stacking operators, obtained in the previous chapters under the assumption of an inhomogeneous isotropic medium, are also valid in an anisotropic medium and have the same representations. This is because the explicit DSR stacking operators and the DSR-PS stacking operators are the special cases of the CO DSR stacking operator, derived from exactly the same parabolic traveltime approximation. In the case of an anisotropic medium, the parameters of the DSR stacking operators lose their clear physical interpretation and incorporate anisotropy effects.

5.5 Conclusions

In this chapter I have derived the CO DSR stacking operator from paraxial ray theory. This new formulation adds sufficiently to our understanding of the DSR stacking operators. In fact, it appears that the DSR stacking operators, derived from geometrical considerations, are just a reformulation of the well-known hyperbolic CRS stacking operator, derived from the paraxial ray theory. Both formulations have their advantages: while the double-square-root traveltime expression perfectly describes diffraction events, the hyperbolic CRS operator is exact for reflected waves from inclined flat surfaces. Since the original parabolic traveltime approximation is valid for inhomogeneous anisotropic layered media, the DSR stacking operators are also applicable in this general type of medium.

Moreover, I have found the CO DSR stacking operator for pure diffraction events. In my opinion, this DSR formulation is physically more intuitive than the parabolic traveltime formula. I think that this new DSR operator could further improve the enhancement of diffraction events.

Finally, a number of potential weaknesses of the CO DSR approximation has to be considered. The current formulation of the CO DSR stacking operator is challenging for implementation since it requires additional parameters: the traveltimes along the ray segments and the weight coefficients η_1 , η_2 , defining the "mixed" term. As was found in this work, in the ZO case, the "mixed" term depends only on the curvature of the normal wave. However, with the knowledge obtained so far, I cannot argue that this remains valid in the CO case. The solution of this problem gives a possibility for the efficient implementation of the CO DSR stacking operator.

Summary and Outlook

Several new multidimensional stacking operators have been suggested in this thesis (see Figure 5.3). Some of them are extensions of the already existing i-CRS and n-CRS stacking operators from the standard 2D case to the 3D case and to the case of converted PS waves. Another "family" of stacking operators, the DSR stacking operators, provides a completely novel representation of the traveltime of the reflected wave. Although they are not as accurate as i-CRS and n-CRS, they have a unique role among the DSR-based stacking operators, since they could be derived both from the model-based approach and from the paraxial ray theory.

Thus, the paraxial ray theory is the origin of two alternative representations of the traveltime of the reflected wave (3D CO CRS and 3D CO DSR). In some sense, these representations are asymptotic: while CRS perfectly describes the traveltime response from plane reflectors (reflector curvature is equal to zero), DSR is designed for the scattered waves from point diffractors (reflector curvature is equal to infinity). I have also shown that for every DSR operator there is a corresponding n-CRS stacking operator which "sews" both asymptotic solutions. As a result, n-CRS inherits from the paraxial ray theory a number of useful features, i.e., n-CRS stacking operators are valid for inhomogeneous anisotropic medium.

Several stacking operators have not been discussed in detail, but their derivation is possible based on the principles proposed in this work. For example, the derivation of 3D i-CRS stacking operator for converted waves is straightforward with the proposed auxiliary anisotropic medium. Also the n-CRS formula for the case of CO geometry could be immediately obtained from the CO DSR stacking operator. However, the model-based derivation of the CO stacking operators is still not fully understood.

Unfortunately, the 3D i-CRS stacking operator, which was the original objective of this research, turned out to be computationally very expensive. Nevertheless, the investigation of 3D i-CRS eventually led to the discovery of the auxiliary anisotropic medium. The auxiliary anisotropic medium incorporates properties of effective and optical auxiliary media and it is an essential element of the 3D simplified model.

Although all new stacking operators provide better accuracy than the conventional CRS stack (and, hence, can potentially be used for larger spreads), they are still the short-spread

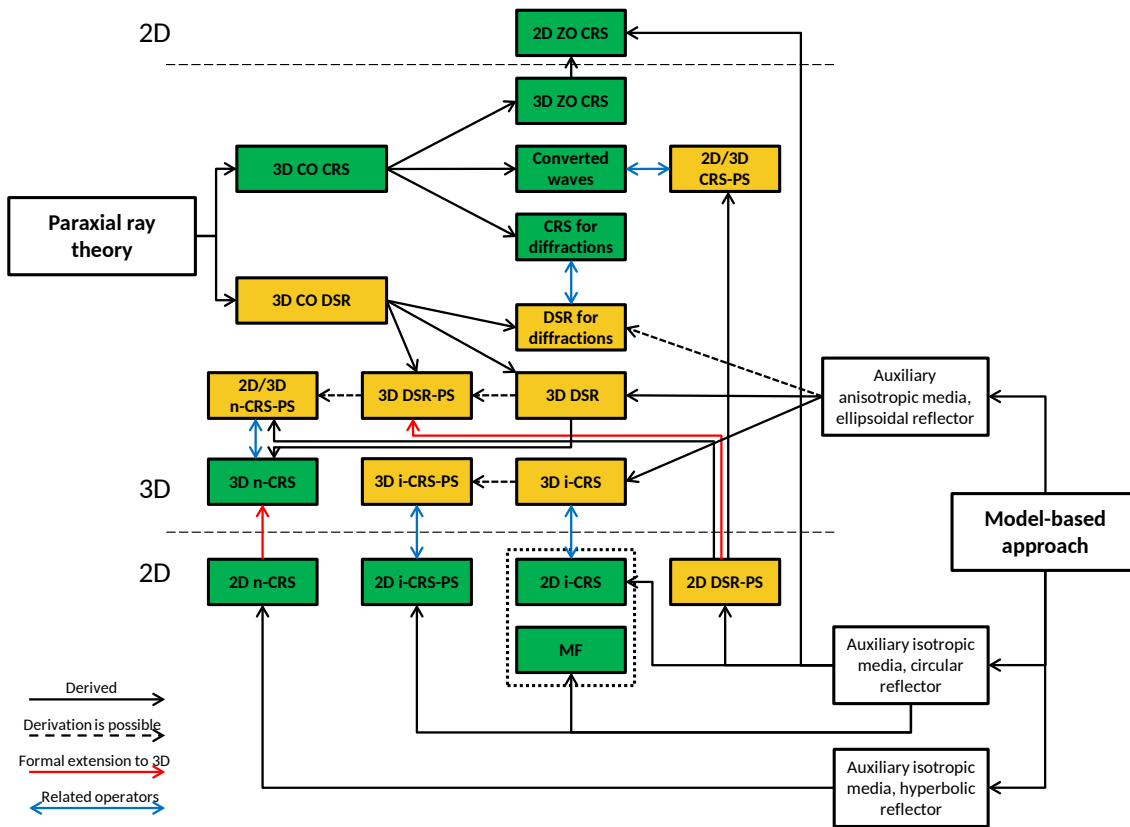


Figure 5.3: Classification of the new multidimensional stacking operators (compare with Figure 1.8). The new stacking operators (in yellow boxes) are derived from the paraxial ray theory and from the model-based approach. The black dashed arrow indicates that the derivation/extension of the stacking operator is possible, but not discussed in the thesis. The blue solid arrows show the related stacking operators.

approximations and could be applied only for "local" stacking. The CO DSR stacking operator is important for theory, however, it remains to be further clarified whether the effective implementation could be proposed for this stacking operator. It is also worth mentioning that although the PS stacking operators have been derived under the assumption of constant v_P/v_S ratio, they could be applied, with caution, to the complex media with non-constant v_P/v_S ratio.

In future, it will be of great interest to apply the new stacking operators to field data, especially for the 3D case and for the case of converted waves. The derivation of DSR and n-CRS stacking operators from the paraxial ray theory, as well as the formulation of the paraxial ray theory for the general anisotropic medium, opens up a lot of new opportunities. Future work should also find an interpretation of the stacking parameters in the presence of anisotropy and extend the existing applications (e.g. NIP wave tomography) to the case of anisotropic media.

Finally, I would like to make several recommendations. I found out that the explicit stacking operators (especially n-CRS) turned out to be the most efficient. If possible, I suggest to jointly interpret the PP and PS stacked sections as well as the related attributes. I also recommend to use the DSR-based stacking operators for diffraction imaging and enhancement.

Appendix A

Traveltime of NIP and normal waves

A.1 Traveltimes in inhomogeneous medium

In this section, I obtain the hyperbolic expressions for the traveltime of the NIP and normal waves in the 3D inhomogeneous medium.

In the special ray-centered coordinate system \mathcal{L}' , the NIP wavefront arrives at the central point $\hat{\mathbf{x}}'_0 = (0, 0, 0)$ at the time $\frac{t_0}{2}$ with the curvature \mathbf{K}'_{NIP} (see Section 2.3). The goal is to find the traveltime, needed for the NIP wavefront to reach the point $\hat{\mathbf{x}}' = (x', y', 0)$ in the vicinity of the central point.

In the vicinity of the central point, the traveltime of the NIP wave in the inhomogeneous medium may be presented as a truncated Taylor series expansion about $\mathbf{x}' = (x', y')$:

$$t(\mathbf{x}') = \frac{t_0}{2} + \frac{1}{2} \mathbf{x}'^T \frac{\partial^2 t}{\partial \mathbf{x}' \partial \mathbf{x}'} \mathbf{x}'. \quad (\text{A.1})$$

The second spatial derivatives of the traveltime in the ray-centered coordinate system are linked with the wavefront curvature (Červený, 2001), therefore:

$$\frac{\partial^2 t}{\partial \mathbf{x}' \partial \mathbf{x}'} = \frac{1}{v_0} \mathbf{K}'_{\text{NIP}}. \quad (\text{A.2})$$

The final formula for the traveltime of the NIP wave in the inhomogeneous medium is obtained by squaring (A.1) and omitting the terms of order higher than two:

$$t^2(\mathbf{x}') = \frac{t_0^2}{4} + \frac{t_0}{2v_0} \mathbf{x}'^T \mathbf{K}'_{\text{NIP}} \mathbf{x}'. \quad (\text{A.3})$$

Similar result may be obtained for the normal wave:

$$t^2(\mathbf{x}') = \frac{t_0^2}{4} + \frac{t_0}{2v_0} \mathbf{x}'^T \mathbf{K}'_{\text{N}} \mathbf{x}'. \quad (\text{A.4})$$

A.2 Travelttime of NIP wave in auxiliary medium

In this section, I obtain the travelttime of the NIP wave in the auxiliary anisotropic medium.

The NIP wave originates from the image source located at the point $(0, 0, R_{\text{NIP}}^*)$ in the auxiliary anisotropic medium (in the \mathcal{L}' system). The travelttime, needed for the NIP wavefront to reach the point $\hat{\mathbf{x}}' = (x', y', 0)$ in the vicinity of the central point is obviously equal:

$$t^2(\mathbf{x}') = \frac{R_{\text{NIP}}^{*2} + |\mathbf{x}'|^2}{\zeta^2}, \quad (\text{A.5})$$

where the group velocity ζ

$$\frac{1}{\zeta^2(\Theta, \Phi)} = \frac{\sin^2 \Theta \cos^2 \Phi}{A_{11}} + \frac{\sin^2 \Theta \sin^2 \Phi}{A_{22}} + \frac{\cos^2 \Theta}{A_{33}} \quad (\text{A.6})$$

depends on the group angles:

$$\sin^2 \Theta \cos^2 \Phi = \frac{x'^2}{R_{\text{NIP}}^{*2} + |\mathbf{x}'|^2}, \quad \sin^2 \Theta \sin^2 \Phi = \frac{y'^2}{R_{\text{NIP}}^{*2} + |\mathbf{x}'|^2}, \quad \cos^2 \Theta = \frac{R_{\text{NIP}}^{*2}}{R_{\text{NIP}}^{*2} + |\mathbf{x}'|^2}. \quad (\text{A.7})$$

Substitution the value of the group velocity (A.6) into the travelttime of the NIP wave in the auxiliary medium (A.5) yields:

$$t^2(\mathbf{x}') = \frac{R_{\text{NIP}}^{*2}}{A_{33}} + \mathbf{x}'^T \begin{pmatrix} \frac{1}{A_{11}} & 0 \\ 0 & \frac{1}{A_{22}} \end{pmatrix} \mathbf{x}'. \quad (\text{A.8})$$

By comparing the curvatures in the expressions (A.3) and (A.8), the parameters A_{11}, A_{22} of the auxiliary medium are found to be:

$$\frac{1}{A_{11}} = \frac{t_0}{2v_0} k'_{\text{NIP}}{}^{11}, \quad \frac{1}{A_{22}} = \frac{t_0}{2v_0} k'_{\text{NIP}}{}^{22}. \quad (\text{A.9})$$

A.3 Travelttime of normal wave in auxiliary medium

In this section, I obtain the travelttime of the normal wave in the auxiliary anisotropic medium.

Consider the parabolic reflector with the curvature \mathbf{K}'_{R} in the special ray-centered coordinate system \mathcal{L}' (see Section 2.3). The reflector is embedded in the auxiliary anisotropic medium (see Section 2.4 and Figure 2.4b).

The surface of the reflector $\hat{\mathbf{x}}'_{\text{ref}}$ is given by:

$$\hat{\mathbf{x}}'_{\text{ref}}(\mathbf{x}'_{\text{ref}}) = \begin{pmatrix} x'_{\text{ref}} \\ y'_{\text{ref}} \\ f(x'_{\text{ref}}, y'_{\text{ref}}) \end{pmatrix}, \quad \mathbf{x}'_{\text{ref}} \equiv \begin{pmatrix} x'_{\text{ref}} \\ y'_{\text{ref}} \end{pmatrix}, \quad (\text{A.10})$$

where

$$f(\mathbf{x}'_{ref}) = R_{\text{NIP}}^* + \frac{1}{2} \mathbf{x}'_{ref} \mathbf{T} \mathbf{K}'_{\text{R}} \mathbf{x}'_{ref}, \quad (\text{A.11})$$

\mathbf{K}'_{R} is the symmetric curvature matrix:

$$\mathbf{K}'_{\text{R}} = \begin{pmatrix} k'_{\text{R}}{}^{11} & k'_{\text{R}}{}^{12} \\ k'_{\text{R}}{}^{21} & k'_{\text{R}}{}^{22} \end{pmatrix}, \quad (\text{A.12})$$

R_{NIP}^* is the apex of the reflector:

$$R_{\text{NIP}}^* \equiv \frac{t_0 v_0}{2}, \quad (\text{A.13})$$

$\frac{t_0}{2}$ is the one-way traveltime along the central ray and v_0 is the group velocity in the z' -direction.

The normal vector to the reflector surface is equal to:

$$\hat{\mathbf{n}}'(\mathbf{x}'_{ref}) = \begin{pmatrix} k'_{\text{R}}{}^{11} x'_{ref} + k'_{\text{R}}{}^{12} y'_{ref} \\ k'_{\text{R}}{}^{21} x'_{ref} + k'_{\text{R}}{}^{22} y'_{ref} \\ -1 \end{pmatrix}. \quad (\text{A.14})$$

Since the normal wavefront originates as an exploding reflector, the direction of the vector $\hat{\mathbf{n}}'$ defines the phase polar θ and azimuthal ϕ angles:

$$\hat{\mathbf{n}}' = |\hat{\mathbf{n}}'| \begin{pmatrix} \sin \theta \cos \phi \\ \sin \theta \sin \phi \\ \cos \theta \end{pmatrix}. \quad (\text{A.15})$$

In the 3D case, the auxiliary medium is a weakly anisotropic ellipsoidal medium. In the weakly anisotropic ellipsoidal medium, the group polar Θ and azimuthal Φ angles are related with the phase angles (Daley and Krebs, 2005, p. 5 eq. 17,19):

$$\tan \Phi = \frac{A_{22}}{A_{11}} \tan \phi, \quad \tan \Theta = \frac{A_{11} \tan \theta \cos \phi [1 + (A_{22}/A_{11})^2 \tan^2 \phi]^{1/2}}{A_{33}}. \quad (\text{A.16})$$

The group angles define the direction and the value of the group velocity ζ (Daley and Krebs, 2005, p. 5 eq. 21):

$$\frac{1}{\zeta^2(\Theta, \Phi)} = \frac{\sin^2 \Theta \cos^2 \Phi}{A_{11}} + \frac{\sin^2 \Theta \sin^2 \Phi}{A_{22}} + \frac{\cos^2 \Theta}{A_{33}}. \quad (\text{A.17})$$

In summary, the parameters (x'_{ref}, y'_{ref}) define the point on the reflector $\hat{\mathbf{x}}'_{ref}$, the normal vector at this point $\hat{\mathbf{n}}'$, the phase angles θ and ϕ , the group angles Θ and Φ , and the group velocity ζ .

Now, consider the ray, which originates at the point $\hat{\mathbf{x}}'_{ref}$ on the reflector. This ray intersects the surface $z' = 0$ at the point $\hat{\mathbf{x}}'_{int}$:

$$\hat{\mathbf{x}}'_{int} = \hat{\mathbf{x}}'_{ref}(\mathbf{x}'_{ref}) + t \hat{\zeta}(\mathbf{x}'_{ref}) \quad (\text{A.18})$$

or, in components:

$$\begin{pmatrix} x'_{int} \\ y'_{int} \\ 0 \end{pmatrix} = \begin{pmatrix} x'_{ref} \\ y'_{ref} \\ f(\mathbf{x}'_{ref}) \end{pmatrix} + t \begin{pmatrix} \zeta_1(\mathbf{x}'_{ref}) \\ \zeta_2(\mathbf{x}'_{ref}) \\ \zeta_3(\mathbf{x}'_{ref}) \end{pmatrix}. \quad (\text{A.19})$$

The traveltime t as a function of \mathbf{x}'_{ref} may be determined from the z -component of the equation (A.19):

$$t(\mathbf{x}'_{ref}) = -\frac{f(\mathbf{x}'_{ref})}{\zeta_3}. \quad (\text{A.20})$$

Substituting (A.20) into (A.19), I obtain the coordinates of the ray's intersection with the surface $z' = 0$:

$$x'_{int} = x'_{ref} - f(\mathbf{x}'_{ref})\zeta_1/\zeta_3, \quad (\text{A.21a})$$

$$y'_{int} = y'_{ref} - f(\mathbf{x}'_{ref})\zeta_2/\zeta_3. \quad (\text{A.21b})$$

The ratio of the group velocity components is equal (see section A.4.2 for details):

$$\zeta_1/\zeta_3 = -\frac{1}{R_{\text{NIP}}^* k'_{\text{NIP}}{}^{11}} (k'_{\text{R}}{}^{11} x'_{ref} + k'_{\text{R}}{}^{12} y'_{ref}), \quad (\text{A.22a})$$

$$\zeta_2/\zeta_3 = -\frac{1}{R_{\text{NIP}}^* k'_{\text{NIP}}{}^{22}} (k'_{\text{R}}{}^{21} x'_{ref} + k'_{\text{R}}{}^{22} y'_{ref}). \quad (\text{A.22b})$$

By substituting (A.11) and (A.22) into (A.21), I get:

$$\mathbf{x}'_{int} = [\mathbf{I} + (1 + \Omega)\mathbf{K}'_{\text{NIP}}{}^{-1}\mathbf{K}'_{\text{R}}] \mathbf{x}'_{ref}, \quad (\text{A.23})$$

where

$$\Omega = \frac{1}{2} \mathbf{x}'_{ref}{}^{\text{T}} \mathbf{K}'_{\text{R}} \mathbf{x}'_{ref} \frac{1}{R_{\text{NIP}}^*} = \frac{\Delta z_{ref}}{R_{\text{NIP}}^*}. \quad (\text{A.24})$$

Since I only consider the rays in the vicinity of the central ray, the parameter $\Omega \ll 1$ and may be neglected:

$$\mathbf{x}'_{int} \approx [\mathbf{K}'_{\text{R}}{}^{-1} + \mathbf{K}'_{\text{NIP}}{}^{-1}] \mathbf{K}'_{\text{R}} \mathbf{x}'_{ref}. \quad (\text{A.25})$$

Therefore, in the vicinity of central ray there is a linear relation between \mathbf{x}'_{ref} and \mathbf{x}'_{int} :

$$\mathbf{x}'_{ref} \approx \mathbf{K}'_{\text{R}}{}^{-1} [\mathbf{K}'_{\text{R}}{}^{-1} + \mathbf{K}'_{\text{NIP}}{}^{-1}]^{-1} \mathbf{x}'_{int}. \quad (\text{A.26})$$

With the last relation it is possible to find the traveltime of the normal wave in the auxiliary medium as a function of \mathbf{x}'_{int} . Indeed, if I square the equation (A.20)

$$t^2(\mathbf{x}'_{ref}) = \frac{f^2(\mathbf{x}'_{ref})}{\zeta_3^2}, \quad (\text{A.27})$$

substitute into this equation the vertical component of the group velocity (see section A.4.3 for details):

$$\frac{1}{\zeta_3^2} = \frac{1}{v_0^2} \left[1 + \frac{1}{R_{\text{NIP}}^*} \mathbf{x}'_{ref}{}^{\text{T}} \mathbf{K}'_{\text{R}} \mathbf{K}'_{\text{NIP}}{}^{-1} \mathbf{K}'_{\text{R}} \mathbf{x}'_{ref} \right] \quad (\text{A.28})$$

and the squared depth of the reflector (the fourth-order term is omitted):

$$f^2(\mathbf{x}'_{ref}) = R_{\text{NIP}}^{*2} + R_{\text{NIP}}^* \mathbf{x}'_{ref} \mathbf{K}'_{\text{R}} \mathbf{x}'_{ref}, \quad (\text{A.29})$$

I obtain (the fourth-order term is omitted):

$$t^2(\mathbf{x}'_{ref}) = \frac{t_0^2}{4} + \frac{t_0}{2v_0} \mathbf{x}'_{ref} \mathbf{K}'_{\text{R}} \mathbf{K}'_{\text{NIP}} \mathbf{K}'_{\text{R}} \mathbf{x}'_{ref} + \frac{t_0}{2v_0} \mathbf{x}'_{ref} \underbrace{\mathbf{K}'_{\text{R}} \mathbf{K}'_{\text{R}}^{-1}}_{\mathbf{I}} \mathbf{K}'_{\text{R}} \mathbf{x}'_{ref}, \quad (\text{A.30})$$

or

$$t^2(\mathbf{x}'_{ref}) = \frac{t_0^2}{4} + \frac{t_0}{2v_0} \mathbf{x}'_{ref} \mathbf{K}'_{\text{R}} \mathbf{K}'_{\text{R}} \mathbf{x}'_{ref} \left[\mathbf{K}'_{\text{R}}^{-1} + \mathbf{K}'_{\text{NIP}}^{-1} \right]. \quad (\text{A.31})$$

Finally, I substitute \mathbf{x}'_{ref} from (A.26):

$$t^2(\mathbf{x}'_{int}) = \frac{t_0^2}{4} + \frac{t_0}{2v_0} \mathbf{x}'_{int} \left[\mathbf{K}'_{\text{R}}^{-1} + \mathbf{K}'_{\text{NIP}}^{-1} \right]^{-1} \mathbf{x}'_{int}. \quad (\text{A.32})$$

A.4 Group velocity components

In this section, I present the proof of the equations (A.22) giving the ratios of the group velocity components and the equation (A.28) for the vertical component of the group velocity. The proof requires two additional useful relations.

A.4.1 Additional useful relations

1. Relations between the group and phase angles:

$$\tan \Theta \cos \Phi = \frac{A_{11}}{A_{33}} \tan \theta \cos \phi, \quad (\text{A.33a})$$

$$\tan \Theta \sin \Phi = \frac{A_{22}}{A_{33}} \tan \theta \sin \phi. \quad (\text{A.33b})$$

These relations are obtained from the equations (A.16) after some basic trigonometric manipulations.

2. Ratios of density normalized elastic parameters:

$$\frac{A_{11}}{A_{33}} = \frac{1}{R_{\text{NIP}}^* k_{\text{NIP}}'^{11}}, \quad (\text{A.34a})$$

$$\frac{A_{22}}{A_{33}} = \frac{1}{R_{\text{NIP}}^* k_{\text{NIP}}'^{22}}. \quad (\text{A.34b})$$

These relations follow immediately from the equations (2.13).

A.4.2 Ratios of group velocity components

In order to proof the equation (A.22a), I use the relation (A.33a), the relation (A.34a) and the expression for the normal vector (A.14):

$$\zeta_1/\zeta_3 = \tan \Theta \cos \Phi = \frac{A_{11}}{A_{33}} \tan \theta \cos \phi = \frac{A_{11} n_1}{A_{33} n_3} = -\frac{k'_R{}^{11} x'_{ref} + k'_R{}^{12} y'_{ref}}{R_{\text{NIP}}^* k'_{\text{NIP}}{}^{11}}. \quad (\text{A.35})$$

The equation (A.22b) can be derived similarly.

A.4.3 Vertical group velocity component

The proof of the equation (A.28) will be given in several steps.

First, I use the definition of the group velocity (A.17):

$$\frac{1}{\zeta_3^2} = \frac{1}{|\zeta|^2 \cos^2 \Theta} = \frac{\tan^2 \Theta \cos^2 \Phi}{A_{11}} + \frac{\tan^2 \Theta \sin^2 \Phi}{A_{22}} + \frac{1}{A_{33}}. \quad (\text{A.36})$$

Second, I use the relations (A.33):

$$\frac{1}{\zeta_3^2} = \frac{A_{11}}{A_{33}^2} \tan^2 \theta \cos^2 \phi + \frac{A_{22}}{A_{33}^2} \tan^2 \theta \sin^2 \phi + \frac{1}{A_{33}}. \quad (\text{A.37})$$

Third, I use the relation between the phase angles and the normal vector (A.15):

$$\frac{1}{\zeta_3^2} = \frac{1}{A_{33}} \left[1 + \frac{A_{11}}{A_{33}} \left(\frac{n_1}{n_3} \right)^2 + \frac{A_{22}}{A_{33}} \left(\frac{n_2}{n_3} \right)^2 \right]. \quad (\text{A.38})$$

Fourth, I use the equations (A.34), the expression for the normal vector (A.14) and the definition of the parameter $A_{33} \equiv v_0^2$:

$$\frac{1}{\zeta_3^2} = \frac{1}{v_0^2} \left[1 + \frac{1}{R_{\text{NIP}}^* k'_{\text{NIP}}{}^{11}} (k'_R{}^{11} x'_{ref} + k'_R{}^{12} y'_{ref})^2 + \frac{1}{R_{\text{NIP}}^* k'_{\text{NIP}}{}^{22}} (k'_R{}^{21} x'_{ref} + k'_R{}^{22} y'_{ref})^2 \right]. \quad (\text{A.39})$$

Finally, I present the result using the matrix notation:

$$\frac{1}{\zeta_3^2} = \frac{1}{v_0^2} \left[1 + \frac{1}{R_{\text{NIP}}^*} \mathbf{x}'_{ref}{}^T \mathbf{K}'_R{}^T \mathbf{K}'_{\text{NIP}}{}^{-1} \mathbf{K}'_R \mathbf{x}'_{ref} \right]. \quad (\text{A.40})$$

Appendix B

3D i-CRS stacking operator

As discussed in Section 2.7, the 3D i-CRS stacking operator consists of:

1. the DSR travelttime formula:

$$t(\vartheta, \varphi) = \underbrace{\sqrt{\frac{X'_s{}^2}{A_{11}} + \frac{Y'_s{}^2}{A_{22}} + \frac{Z'_s{}^2}{A_{33}}}}_{R_s} + \underbrace{\sqrt{\frac{X'_g{}^2}{A_{11}} + \frac{Y'_g{}^2}{A_{22}} + \frac{Z'_g{}^2}{A_{33}}}}_{R_g}, \quad (\text{B.1})$$

where:

$$X'_i = x'_{ref} - x'_i, \quad Y'_i = y'_{ref} - y'_i, \quad Z'_i = z'_{ref} - z'_i, \quad i = s, g, \quad (\text{B.2})$$

$\hat{\mathbf{x}}'_s$ and $\hat{\mathbf{x}}'_g$ are the source and receiver locations, and $\hat{\mathbf{x}}'_{ref}(\vartheta, \varphi)$ is a parametric representation of the reflector surface; and

2. the system of nonlinear equations:

$$\begin{cases} \frac{\partial t}{\partial \vartheta} = 0, \\ \frac{\partial t}{\partial \varphi} = 0, \end{cases} \quad (\text{B.3})$$

which yields the parameters (ϑ_r, φ_r) defining the reflection point $\hat{\mathbf{x}}'_r$ of the paraxial ray.

In this Appendix, I discuss the solution of the system (B.3) based on the example of the ellipsoidal reflector.

B.1 Ellipsoidal reflector

The ellipsoidal reflector can be parameterized both by the lateral coordinates and by the polar angles. The formulas (B.4) and (B.6) give the ellipsoidal surfaces with the center

at the point $(0, 0, R_N^*)$ and the curvature \mathbf{K}'_R at the point $(0, 0, R_{\text{NIP}}^*)$. The depth of the center of the ellipsoid R_N^* , the depth of its apex R_{NIP}^* , and the length of its z' -semi-axis R^* are linked (see Figure 2.5b):

$$R_N^* = R_{\text{NIP}}^* + R^*.$$

B.1.1 Parameterization by lateral coordinates

In this case, the reflection surface is a function of lateral coordinates x' and y' :

$$\hat{\mathbf{x}}'_{ref}(x', y') = \begin{pmatrix} x' \\ y' \\ f(x', y') \end{pmatrix} \quad (\text{B.4})$$

where

$$f(\mathbf{x}') = R_N^* - R^* \sqrt{1 - \frac{1}{R^*} \mathbf{x}'^T \mathbf{K}'_R \mathbf{x}'}. \quad (\text{B.5})$$

B.1.2 Parameterization by polar angles

In this case, the reflection surface is a function of polar ϑ and azimuthal φ angles:

$$\hat{\mathbf{x}}'_{ref}(\vartheta, \varphi) = \begin{pmatrix} A' \sin \vartheta \cos \varphi \\ B' \sin \vartheta \sin(\varphi - \Delta\varphi) \\ R_N^* - R^* \cos \vartheta \end{pmatrix} \quad (\text{B.6})$$

where

$$A' = \sqrt{R^*} \sqrt{\frac{k'_{\text{R}}{}^{22}}{\det \mathbf{K}'_{\text{R}}}}, \quad B' = \sqrt{R^*} \sqrt{\frac{k'_{\text{R}}{}^{11}}{\det \mathbf{K}'_{\text{R}}}}, \quad \sin \Delta\varphi = \frac{k'_{\text{R}}{}^{12}}{\sqrt{k'_{\text{R}}{}^{11} k'_{\text{R}}{}^{22}}}. \quad (\text{B.7})$$

B.2 Linearized iterative approach

The linearized version of system (B.3) is:

$$\begin{cases} A_x + A_{xx} \Delta x'_r{}^{(j)} + A_{xy} \Delta y'_r{}^{(j)} = 0, \\ A_y + A_{yx} \Delta x'_r{}^{(j)} + A_{yy} \Delta y'_r{}^{(j)} = 0, \end{cases} \quad (\text{B.8})$$

where $\Delta x'_r{}^{(j)}$, $\Delta y'_r{}^{(j)}$ are the updates of the reflection point coordinates at the j -th iteration

$$\Delta x'_r{}^{(j)} \equiv x'_r{}^{(j)} - x'_r{}^{(j-1)}, \quad \Delta y'_r{}^{(j)} \equiv y'_r{}^{(j)} - y'_r{}^{(j-1)}. \quad (\text{B.9})$$

The coefficients of the system are equal:

$$\begin{aligned} A_x &= A_x^s + A_x^g, & A_y &= A_y^s + A_y^g, \\ A_{xx} &= A_{xx}^s + A_{xx}^g, & A_{yy} &= A_{yy}^s + A_{yy}^g, & A_{xy} &= A_{xy}^s + A_{xy}^g, & A_{yx} &= A_{yx}, \end{aligned} \quad (\text{B.10})$$

where

$$A_x^i = \frac{1}{R_i} \left[\frac{X'_i}{A_{11}} + \frac{Z'_i f'_{x'}}{A_{33}} \right], \quad (\text{B.11a})$$

$$A_y^i = \frac{1}{R_i} \left[\frac{Y'_i}{A_{22}} + \frac{Z'_i f'_{y'}}{A_{33}} \right], \quad (\text{B.11b})$$

$$A_{xx}^i = \frac{1}{R_i} \left[\frac{1}{A_{11}} + \frac{f'_{x'}{}^2}{A_{33}} + \frac{Z'_i f''_{x'x'}}{A_{33}} - (A_x^i)^2 \right], \quad (\text{B.11c})$$

$$A_{yy}^i = \frac{1}{R_i} \left[\frac{1}{A_{22}} + \frac{f'_{y'}{}^2}{A_{33}} + \frac{Z'_i f''_{y'y'}}{A_{33}} - (A_y^i)^2 \right], \quad (\text{B.11d})$$

$$A_{xy}^i = \frac{1}{R_i} \left[\frac{f'_{x'} f'_{y'}}{A_{33}} + \frac{Z'_i f''_{x'y'}}{A_{33}} - A_x^i A_y^i \right], \quad i = s, g, \quad (\text{B.11e})$$

and $f'_{x'}$, $f'_{y'}$ and $f''_{x'x'}$, $f''_{x'y'}$, $f''_{y'y'}$ are the first and the second-order spatial derivatives of the function f , describing the reflector surface.

Equations (2.6), (2.13) and (2.21) link the variables in (B.11) with the surface-based kinematic wavefield attributes.

B.3 Trigonometric iterative approach

When the reflector surface is parametrized by polar angles, the system (B.3) reduces to:

$$\begin{cases} \frac{1}{R_s} \left(\frac{X'_s}{A_{11}} \frac{\partial x'_{ref}}{\partial \vartheta} + \frac{Y'_s}{A_{22}} \frac{\partial y'_{ref}}{\partial \vartheta} + \frac{Z'_s}{A_{33}} \frac{\partial z'_{ref}}{\partial \vartheta} \right) + \frac{1}{R_g} \left(\frac{X'_g}{A_{11}} \frac{\partial x'_{ref}}{\partial \vartheta} + \frac{Y'_g}{A_{22}} \frac{\partial y'_{ref}}{\partial \vartheta} + \frac{Z'_g}{A_{33}} \frac{\partial z'_{ref}}{\partial \vartheta} \right) = 0, \\ \frac{1}{R_s} \left(\frac{X'_s}{A_{11}} \frac{\partial x'_{ref}}{\partial \varphi} + \frac{Y'_s}{A_{22}} \frac{\partial y'_{ref}}{\partial \varphi} + \frac{Z'_s}{A_{33}} \frac{\partial z'_{ref}}{\partial \varphi} \right) + \frac{1}{R_g} \left(\frac{X'_g}{A_{11}} \frac{\partial x'_{ref}}{\partial \varphi} + \frac{Y'_g}{A_{22}} \frac{\partial y'_{ref}}{\partial \varphi} + \frac{Z'_g}{A_{33}} \frac{\partial z'_{ref}}{\partial \varphi} \right) = 0. \end{cases} \quad (\text{B.12})$$

In the case of the ellipsoidal reflector (B.6), the partial derivatives of $\hat{\mathbf{x}}'_{ref}$ with respect to the angles ϑ and φ are equal:

$$\begin{aligned} \frac{\partial x'_{ref}}{\partial \vartheta} &= A' \cos \vartheta \cos \varphi, & \frac{\partial x'_{ref}}{\partial \varphi} &= -A' \sin \vartheta \sin \varphi, \\ \frac{\partial y'_{ref}}{\partial \vartheta} &= B' \cos \vartheta \sin(\varphi - \Delta\varphi), & \frac{\partial y'_{ref}}{\partial \varphi} &= B' \sin \vartheta \cos(\varphi - \Delta\varphi), \\ \frac{\partial z'_{ref}}{\partial \vartheta} &= R^* \sin \vartheta, & \frac{\partial z'_{ref}}{\partial \varphi} &= 0. \end{aligned} \quad (\text{B.13})$$

Substituting (B.13) into (B.12) yields two implicit equations for the angles ϑ and φ :

$$\tan \phi = \frac{\cos \Delta\varphi \left(\frac{Y'_s}{R_s} + \frac{Y'_g}{R_g} \right)}{\frac{A' A_{22}}{B' A_{11}} \left(\frac{X'_s}{R_s} + \frac{X'_g}{R_g} \right) - \sin \Delta\varphi \left(\frac{Y'_s}{R_s} + \frac{Y'_g}{R_g} \right)}, \quad (\text{B.14a})$$

$$\tan \theta = -\frac{\left(\frac{\Lambda'_s}{R_s} + \frac{\Lambda'_g}{R_g}\right)}{\left(\frac{Z'_s}{R_s} + \frac{Z'_g}{R_g}\right)}, \quad (\text{B.14b})$$

where

$$\Lambda'_i = \frac{A'}{R^*} \frac{A_{33}}{A_{11}} X'_i \cos \phi + \frac{B'}{R^*} \frac{A_{33}}{A_{22}} Y'_i \sin(\phi - \Delta\phi), \quad i = s, g. \quad (\text{B.15})$$

Equations (2.6), (2.13), (2.21) and (B.7) link the variables in (B.14) with the surface-based kinematic wavefield attributes.

Appendix C

Explicit stacking operators

C.1 Alternative representation of n-CRS

The 2D n-CRS stacking operator, proposed by [Fomel and Kazinnik \(2013\)](#), reads:

$$t(m, h) = \sqrt{\frac{F(m) + \chi h^2 + \sqrt{F(m-h)F(m+h)}}{2}}, \quad (\text{C.1})$$

where

$$F(m) = (t_0 + wm)^2 + 2t_0Nm^2, \quad (\text{C.2})$$

$$\chi = 2t_0(2M - N) + w^2, \quad (\text{C.3})$$

and w , M , N are the CRS parameters ([1.17](#)).

This stacking operator may be transformed to more intuitive expression. Indeed, taking into account the relation

$$F(m) + \chi h^2 = \frac{1}{2}F(m-h) + \frac{1}{2}F(m+h) + 4t_0(M-N)h^2 \quad (\text{C.4})$$

yields:

$$t(m, h) = \sqrt{\left[\frac{1}{2}\sqrt{F(m-h)} + \frac{1}{2}\sqrt{F(m+h)}\right]^2 + 2t_0(M-N)h^2}. \quad (\text{C.5})$$

Note, that expressions ([C.1](#)) and ([C.5](#)) are identical.

C.2 3D n-CRS stacking operator

[Fomel and Kazinnik \(2013\)](#) proposed a formal extension of the 2D n-CRS stacking operator to the 3D case. They replaced m , h , w by two-dimensional vectors \mathbf{m} , \mathbf{h} , \mathbf{w} and replaced

M, N by the symmetric 2×2 matrices \mathbf{M} and \mathbf{N} . Thereby, the 3D n-CRS stacking operator reads:

$$t(\mathbf{m}, \mathbf{h}) = \sqrt{\frac{\hat{F}(\mathbf{m}) + \mathbf{h}^T \hat{\chi} \mathbf{h} + \sqrt{\hat{F}(\mathbf{m} - \mathbf{h}) \hat{F}(\mathbf{m} + \mathbf{h})}}{2}}, \quad (\text{C.6})$$

where

$$\hat{F}(\mathbf{m}) = (t_0 + \mathbf{w}^T \mathbf{m})^2 + 2t_0 \mathbf{m}^T \mathbf{N} \mathbf{m}, \quad (\text{C.7})$$

$$\chi = 2t_0(2\mathbf{M} - \mathbf{N}) + \mathbf{w} \mathbf{w}^T. \quad (\text{C.8})$$

The alternative 3D n-CRS expression reads:

$$t(\mathbf{m}, \mathbf{h}) = \sqrt{\left[\frac{1}{2} \sqrt{\hat{F}(\mathbf{m} - \mathbf{h})} + \frac{1}{2} \sqrt{\hat{F}(\mathbf{m} + \mathbf{h})} \right]^2 + 2t_0 \mathbf{h}^T (\mathbf{M} - \mathbf{N}) \mathbf{h}}. \quad (\text{C.9})$$

C.3 3D DSR stacking operator

In this section, I give a proof for the explicit DSR stacking operator from Section 2.8. I start with the DSR expression for the traveltimes of the reflected wave (2.27):

$$t = \sqrt{\frac{X_s'^2}{A_{11}} + \frac{Y_s'^2}{A_{22}} + \frac{Z_s'^2}{A_{33}}} + \sqrt{\frac{X_g'^2}{A_{11}} + \frac{Y_g'^2}{A_{22}} + \frac{Z_g'^2}{A_{33}}}. \quad (\text{C.10})$$

I consider the value under the square root and try to interpret it. I do the following operations:

- Use the definition of $X'_i, Y'_i,$ and Z'_i (2.25):

$$S_i \equiv \frac{(x'_i - x'_{ref})^2}{A_{11}} + \frac{(y'_i - y'_{ref})^2}{A_{22}} + \frac{(z'_i - z'_{ref})^2}{A_{33}}, \quad i = s, g. \quad (\text{C.11})$$

- Use the definition of auxiliary media (2.13):

$$S_i \equiv \frac{t_0}{2v_0} k_{NIP}^{11} (x'_i - x'_{ref})^2 + \frac{t_0}{2v_0} k_{NIP}^{22} (y'_i - y'_{ref})^2 + \frac{1}{v_0^2} (z'_i - z'_{ref})^2. \quad (\text{C.12})$$

- Use the vector and matrix notations:

$$S_i \equiv \underbrace{\frac{t_0}{2v_0} (\mathbf{x}'_i - \mathbf{x}'_{ref})^T \mathbf{K}'_{NIP} (\mathbf{x}'_i - \mathbf{x}'_{ref})}_{S_i^{(1)}} + \underbrace{\frac{z_{ref}'^2}{v_0^2}}_{S_i^{(2)}} - \underbrace{\frac{2z'_i z'_{ref}}{v_0^2}}_{S_i^{(3)}} + \underbrace{\frac{z_i'^2}{v_0^2}}_{S_i^{(4)}}. \quad (\text{C.13})$$

- Find $S_i^{(1)}$:

Use the definition of \mathbf{x}'_i :

$$\mathbf{x}'_i \equiv \mathbf{m}' \mp \mathbf{h}', \quad (\text{C.14})$$

and approximation for the reflection point (2.35):

$$\mathbf{x}'_{ref} \approx \left[\mathbf{I} - \mathbf{K}'_{NIP}{}^{-1} \mathbf{K}'_N \right] \mathbf{m}'. \quad (\text{C.15})$$

$$(\mathbf{x}'_i - \mathbf{x}'_{ref}) = \mathbf{K}'_{NIP}{}^{-1} \mathbf{K}'_N \mathbf{m}' \mp \mathbf{h}'. \quad (\text{C.16})$$

$$S_i^{(1)} = \frac{t_0}{2v_0} \left[\mathbf{m}'^T \mathbf{K}'_N{}^T (\mathbf{K}'_{NIP}{}^{-1})^T \mathbf{K}'_N \mathbf{m}' \mp 2\mathbf{m}'^T \mathbf{K}'_N{}^T \mathbf{h}' + \mathbf{h}'^T \mathbf{K}'_{NIP}{}^T \mathbf{h}' \right]. \quad (\text{C.17})$$

- Find $S_i^{(2)}$:

Use the relation between curvatures (2.21):

$$\mathbf{K}'_R = [\mathbf{K}'_N{}^{-1} - \mathbf{K}'_{NIP}{}^{-1}]^{-1} \quad (\text{C.18})$$

and the paraboloidal reflector (A.11):

$$z'_{ref} = R_{NIP}^* + \frac{1}{2} \mathbf{x}'_{ref}{}^T \mathbf{K}'_R \mathbf{x}'_{ref}. \quad (\text{C.19})$$

$$z'_{ref} = \frac{t_0 v_0}{2} + \frac{1}{2} \mathbf{m}'^T \mathbf{K}'_N \mathbf{m}' - \frac{1}{2} \mathbf{m}'^T \mathbf{K}'_N{}^T (\mathbf{K}'_{NIP}{}^{-1})^T \mathbf{K}'_N \mathbf{m}'. \quad (\text{C.20})$$

$$S_i^{(2)} = \frac{t_0^2}{4} + \frac{t_0}{2v_0} \mathbf{m}'^T \mathbf{K}'_N \mathbf{m}' - \frac{t_0}{2v_0} \mathbf{m}'^T \mathbf{K}'_N{}^T (\mathbf{K}'_{NIP}{}^{-1})^T \mathbf{K}'_N \mathbf{m}'. \quad (\text{C.21})$$

- Find $S_i^{(3)}$:

Use the link between the coordinate systems (2.6):

$$\hat{\mathbf{x}}' = \underbrace{\hat{\mathbf{R}}_z^T(\delta) \hat{\mathbf{R}}_y^T(\alpha) \hat{\mathbf{R}}_z^T(\beta)}_{\hat{\mathbf{B}}^T} (\hat{\mathbf{x}} - \hat{\mathbf{x}}_0). \quad (\text{C.22})$$

$$z'_i = \hat{\mathbf{B}}_{31}^T (x_i - x_0) + \hat{\mathbf{B}}_{32}^T (y_i - y_0) + \underbrace{\hat{\mathbf{B}}_{33}^T (z_i - z_0)}_{=0}. \quad (\text{C.23})$$

The elements of the matrix $\hat{\mathbf{B}}$ are equal:

$$\hat{\mathbf{B}}_{31}^T = \sin \alpha \cos \beta, \quad \hat{\mathbf{B}}_{32}^T = \sin \alpha \sin \beta \quad (\text{C.24})$$

$$z'_i = \begin{pmatrix} \sin \alpha \cos \beta \\ \sin \alpha \sin \beta \end{pmatrix} \Delta \mathbf{x}_i = -\frac{v_0}{2} \mathbf{w}^T \Delta \mathbf{x}_i. \quad (\text{C.25})$$

$$S_i^{(3)} = \frac{t_0}{2} \mathbf{w}^T \Delta \mathbf{x}_i. \quad (\text{C.26})$$

- Find $S_i^{(4)}$:

$$S_i^{(4)} = \frac{1}{4} (\mathbf{w}^T \Delta \mathbf{x}_i)^2. \quad (\text{C.27})$$

- Combine $S_i^{(1)}$, $S_i^{(2)}$, $S_i^{(3)}$ and $S_i^{(4)}$:

$$S_i = \frac{t_0^2}{4} + \frac{t_0}{2} \mathbf{w}^T \Delta \mathbf{x}_i + \frac{1}{4} (\mathbf{w}^T \Delta \mathbf{x}_i)^2 + \frac{t_0}{2v_0} \left[\mathbf{m}'^T \mathbf{K}'_N \mathbf{m}' \mp 2\mathbf{m}'^T \mathbf{K}'_N \mathbf{h}' + \mathbf{h}'^T \mathbf{K}'_{NIP} \mathbf{h}' \right], \quad (\text{C.28})$$

or

$$\frac{1}{4} S_i = \left[t_0 + \mathbf{w}^T \Delta \mathbf{x}_i \right]^2 + 2t_0 \left[\mathbf{m}^T \mathbf{N} \mathbf{m} \mp 2\mathbf{m}^T \mathbf{N} \mathbf{h} + \mathbf{h}^T \mathbf{M} \mathbf{h} \right] \quad i = s, g. \quad (\text{C.29})$$

Finally, I obtain the 3D DSR stacking operator:

$$t(\mathbf{m}, \mathbf{h}) = \frac{1}{2} \sqrt{\left[t_0 + \mathbf{w}^T \Delta \mathbf{x}_s \right]^2 + 2t_0 \left[\mathbf{m}^T \mathbf{N} \mathbf{m} - 2\mathbf{m}^T \mathbf{N} \mathbf{h} + \mathbf{h}^T \mathbf{M} \mathbf{h} \right]} + \frac{1}{2} \sqrt{\left[t_0 + \mathbf{w}^T \Delta \mathbf{x}_g \right]^2 + 2t_0 \left[\mathbf{m}^T \mathbf{N} \mathbf{m} + 2\mathbf{m}^T \mathbf{N} \mathbf{h} + \mathbf{h}^T \mathbf{M} \mathbf{h} \right]}. \quad (\text{C.30})$$

C.4 Relation between 3D DSR and 3D n-CRS

The 3D DSR stacking operator (C.30) could be further transformed to the 3D n-CRS stacking operator. Indeed, using notation \hat{F} (C.7), the 3D DSR stacking operator reads:

$$t(\mathbf{m}, \mathbf{h}) = \frac{1}{2} \sqrt{\hat{F}(\Delta \mathbf{x}_s) + 2t_0 \mathbf{h}^T (\mathbf{M} - \mathbf{N}) \mathbf{h}} + \frac{1}{2} \sqrt{\hat{F}(\Delta \mathbf{x}_g) + 2t_0 \mathbf{h}^T (\mathbf{M} - \mathbf{N}) \mathbf{h}}. \quad (\text{C.31})$$

If I square the right-hand side of the last expression

$$t(\mathbf{m}, \mathbf{h}) = \sqrt{\left[\frac{1}{2} \sqrt{\hat{F}(\Delta \mathbf{x}_s) + 2t_0 \mathbf{h}^T (\mathbf{M} - \mathbf{N}) \mathbf{h}} + \frac{1}{2} \sqrt{\hat{F}(\Delta \mathbf{x}_g) + 2t_0 \mathbf{h}^T (\mathbf{M} - \mathbf{N}) \mathbf{h}} \right]^2}, \quad (\text{C.32})$$

"take out" $2t_0 \mathbf{h}^T (\mathbf{M} - \mathbf{N}) \mathbf{h}$ from the square roots and neglect the terms of higher order than the second, I obtain the stacking operator

$$t(\mathbf{m}, \mathbf{h}) = \sqrt{\left[\frac{1}{2} \sqrt{\hat{F}(\Delta \mathbf{x}_s)} + \frac{1}{2} \sqrt{\hat{F}(\Delta \mathbf{x}_g)} \right]^2 + 2t_0 \mathbf{h}^T (\mathbf{M} - \mathbf{N}) \mathbf{h}}, \quad (\text{C.33})$$

that is identical to 3D n-CRS (C.9).

Appendix D

Stacking operators for converted waves

D.1 Deviation angle

In this section I derive the deviation angle ϑ_r (equation (4.9)). I consider the circular reflector with the center O , the central point X_0 , and the source and the receiver at X_S , X_G , respectively (see Figure D.1). The converted PS ray reflects from the circle at the point S . The line passing through the points O and S intersects the measurement surface at the point X_P . In all derivations of this appendix, I assume that the source and receiver displacements

$$\Delta x_s \equiv X_S - X_0, \quad \Delta x_g \equiv X_G - X_0 \quad (\text{D.1})$$

are small compared to the typical scale of the problem (like $R_N \equiv OX_0$ or $R_{\text{NIP}} \approx SX_P$):

$$\varepsilon \equiv \max\left(\frac{|\Delta x_s|}{R_{\text{NIP}}}, \frac{|\Delta x_g|}{R_{\text{NIP}}}, \frac{|\Delta x_s|}{R_N}, \frac{|\Delta x_g|}{R_N}\right), \quad \varepsilon \ll 1. \quad (\text{D.2})$$

I can express the deviation angle $\vartheta_r = \angle X_0 O X_P$ by the relations in the triangle $\triangle X_0 O X_P$:

$$\sin \vartheta_r = \frac{X_0 X_P}{O X_P} \sin\left(\frac{\pi}{2} - \alpha\right) = \frac{X_0 X_P}{O X_P} \cos \alpha = \frac{X_0 X_P}{O X_0} \cos \alpha (1 + O(\varepsilon)). \quad (\text{D.3})$$

The combination of the Snell's Law and the relations in the triangles $\triangle X_S S X_P$, $\triangle X_G S X_P$,

$$\frac{\sin \theta_1}{v_P} = \frac{\sin \theta_2}{v_S}, \quad \frac{l_1}{\sin \theta_1} = \frac{r_1}{\sin \beta}, \quad \frac{l_2}{\sin \theta_2} = \frac{r_2}{\sin(\pi - \beta)}, \quad \beta = \angle X_S X_P S \quad (\text{D.4})$$

lead to the following estimation of the ratio l_1/l_2 :

$$\frac{l_1}{l_2} = \frac{v_P r_1}{v_S r_2} = \gamma \frac{r_1}{r_2} = \gamma(1 + O(\varepsilon)). \quad (\text{D.5})$$

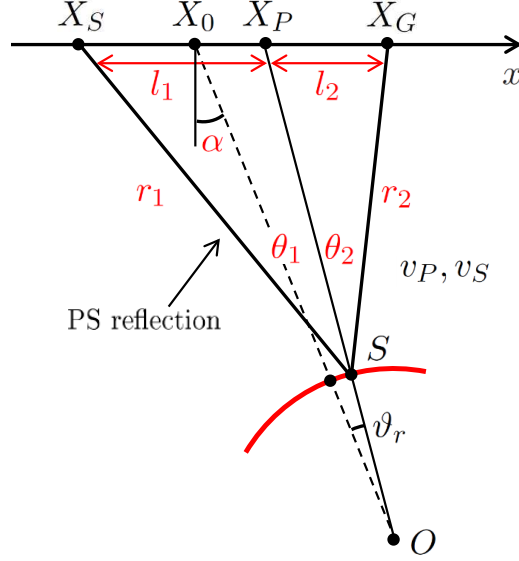


Figure D.1: Illustration of the notations used in the derivation of $\sin \vartheta$.

Here I took into account that:

$$\frac{r_1}{r_2} = 1 + O(\varepsilon). \quad (\text{D.6})$$

The combination of (D.5) and the fact that $l_1 + l_2 = X_G - X_S$ yields the following expression for $X_0 X_P$:

$$X_0 X_P = \frac{\gamma \Delta x_g + \Delta x_s}{1 + \gamma} (1 + O(\varepsilon)).$$

where a variable change from X_S, X_G to $\Delta x_s, \Delta x_g$ was made. Substituting $X_0 X_P$ into the equation (D.3) gives the final result:

$$\sin \vartheta_r = \frac{\gamma \Delta x_g + \Delta x_s}{(1 + \gamma) R_N} \cos \alpha + O(\varepsilon^2), \quad (\text{D.7})$$

or, alternatively, in the γ -CMP coordinates (4.5):

$$\sin \vartheta_r = \frac{\tilde{m}}{R_N} \cos \alpha + O(\varepsilon^2). \quad (\text{D.8})$$

D.2 Derivation of DSR-PS stacking operator

In this section I present the derivation of the DSR-PS staking operator (4.10). I start with the DSR expression for the traveltme of converted PS wave in constant-velocity medium:

$$t = \frac{1}{v_P} \sqrt{(x_s - x_r)^2 + z_r^2} + \frac{1}{v_S} \sqrt{(x_g - x_r)^2 + z_r^2}. \quad (\text{D.9})$$

Here x_s and x_g are the lateral coordinates of source and receiver, x_r, z_r denote the location of the reflection point, and v_P and v_S are the velocities of P- and S-waves, respectively

(see Figure 4.1). For convenience, I denote the expression under the square root by S_i :

$$S_i \equiv (x_i - x_r)^2 + z_r^2, \quad i = s, g. \quad (\text{D.10})$$

It is apparent from the Figures 4.1 and D.1 that the reflection point coordinates are equal:

$$\begin{aligned} x_r &= R_N \sin \alpha - R \sin(\alpha - \vartheta_r) + x_0, \\ z_r &= R_N \cos \alpha - R \cos(\alpha - \vartheta_r). \end{aligned} \quad (\text{D.11})$$

Substitution of (D.11) into (D.10) and simplification of trigonometric expressions yield:

$$S_i = R_N^2 + R^2 - 2R_N R \cos \vartheta_r + 2\Delta x_i R \sin(\alpha - \vartheta_r) - 2\Delta x_i R_N \sin \alpha + \Delta x_i^2. \quad (\text{D.12})$$

The goal is to find a traveltime approximation which is accurate up to second order of ε . Hence, in the approximation for $\cos \vartheta_r$ I include the second order term:

$$\cos \vartheta_r = 1 - \frac{1}{2} \sin^2 \vartheta_r + O(\varepsilon^4) \quad (\text{D.13})$$

and in $\sin(\alpha - \vartheta_r)$ I retain only linear terms:

$$\sin(\alpha - \vartheta_r) = \sin \alpha \underbrace{\cos \vartheta_r}_{=1+O(\varepsilon^2)} - \cos \alpha \sin \vartheta_r. \quad (\text{D.14})$$

Substituting (D.13) and (D.14) into (D.12) and taking into account the relation $R_N = R_{\text{NIP}} + R$ yields:

$$S_i = \left[R_{\text{NIP}} - \Delta x_i \sin \alpha \right]^2 + R_N R \sin^2 \vartheta_r - 2\Delta x_i R \cos \alpha \sin \vartheta_r + \Delta x_i^2 \cos^2 \alpha. \quad (\text{D.15})$$

Now, I substitute the approximation for $\sin \vartheta_r$ (D.3):

$$S_i = \left[R_{\text{NIP}} - \Delta x_i \sin \alpha \right]^2 + \cos^2 \alpha \left[\frac{R}{R_N} \tilde{m}^2 - 2 \frac{R}{R_N} \tilde{m} \Delta x_i + \Delta x_i^2 \right]. \quad (\text{D.16})$$

In equation (D.16), the source and receiver displacements $\Delta x_i, i = s, g$ are equal to:

$$\Delta x_s = \tilde{m} - \gamma \tilde{h}, \quad \Delta x_g = \tilde{m} + \tilde{h}. \quad (\text{D.17})$$

To simplify these notations, I introduce \tilde{h}_i :

$$\tilde{h}_i = \begin{cases} -\gamma \tilde{h}, & i = s \\ \tilde{h}, & i = g \end{cases}, \quad \Delta x_i = \tilde{m} + \tilde{h}_i, \quad i = s, g. \quad (\text{D.18})$$

With these notations S_i is equal:

$$S_i = \left[R_{\text{NIP}} - \Delta x_i \sin \alpha \right]^2 + \cos^2 \alpha R_{\text{NIP}} \left[\frac{\tilde{m}^2}{R_N} + \frac{2\tilde{m}\tilde{h}_i}{R_N} + \frac{\tilde{h}_i^2}{R_{\text{NIP}}} \right]. \quad (\text{D.19})$$

Velocities of P- and S-waves can be expressed as:

$$\frac{1}{v_P} = \frac{1}{1 + \gamma v_{eff}}, \quad \frac{1}{v_S} = \frac{\gamma}{1 + \gamma v_{eff}}. \quad (\text{D.20})$$

Hence,

$$\left(\frac{2}{v_{eff}}\right)^2 S_i = \left[t_0 - \frac{2 \sin \alpha}{v_{eff}} \Delta x_i\right]^2 + 2t_0 \frac{\cos^2 \alpha}{v_{eff}} \left[\frac{\tilde{m}^2}{R_N} + \frac{2\tilde{m}\tilde{h}_i}{R_N} + \frac{\tilde{h}_i^2}{R_{NIP}}\right] \quad (D.21)$$

Here I took into account that the traveltime of the central ray is equal:

$$t_0 = \frac{2R_{NIP}}{v_{eff}}. \quad (D.22)$$

Finally, by introducing the coefficients:

$$\tilde{w} = -\frac{2 \sin \alpha}{v_{eff}}, \quad \tilde{M} = \frac{\cos^2 \alpha}{v_{eff} R_{NIP}}, \quad \tilde{N} = \frac{\cos^2 \alpha}{v_{eff} R_N} \quad (D.23)$$

I obtain the compact and elegant expression for the quantity under the square root:

$$\left(\frac{2}{v_{eff}}\right)^2 S_i = \left[t_0 + \tilde{w} \Delta x_i\right]^2 + 2t_0 \left[\tilde{N} \tilde{m}^2 + 2\tilde{N} \tilde{m} \tilde{h}_i + \tilde{M} \tilde{h}_i^2\right] \quad (D.24)$$

Substitution of (D.24) into (D.9) gives the DSR-PS stacking operator:

$$t(\tilde{m}, \tilde{h}) = \frac{1}{1+\gamma} \sqrt{\left[t_0 + \tilde{w} \Delta x_s\right]^2 + 2t_0 \left[\tilde{N} \tilde{m}^2 - 2\tilde{N} \tilde{m}(\gamma \tilde{h}) + \tilde{M}(\gamma \tilde{h})^2\right]} + \frac{\gamma}{1+\gamma} \sqrt{\left[t_0 + \tilde{w} \Delta x_g\right]^2 + 2t_0 \left[\tilde{N} \tilde{m}^2 + 2\tilde{N} \tilde{m} \tilde{h} + \tilde{M} \tilde{h}^2\right]}. \quad (D.25)$$

D.3 Derivation of CRS-PS stacking operator

In this section I discuss the derivation of the CRS-PS formula (4.12). I begin with the DSR-PS stacking operator (D.25). I "take out" $(t_0 + \tilde{w} \Delta x_i)$ from the square roots, make Taylor series expansion of the square roots and neglect the terms of higher order than the second:

$$t = \frac{(t_0 + \tilde{w} \Delta x_s)}{1+\gamma} \left(1 + \frac{1}{(t_0 + \tilde{w} \Delta x_s)} \left[\tilde{N} \tilde{m}^2 - 2\tilde{N} \tilde{m}(\gamma \tilde{h}) + \tilde{M}(\gamma \tilde{h})^2\right]\right) + \frac{\gamma(t_0 + \tilde{w} \Delta x_g)}{1+\gamma} \left(1 + \frac{1}{(t_0 + \tilde{w} \Delta x_g)} \left[\tilde{N} \tilde{m}^2 + 2\tilde{N} \tilde{m} \tilde{h} + \tilde{M} \tilde{h}^2\right]\right). \quad (D.26)$$

After some simplifications:

$$t = t_0 + \underbrace{\tilde{w} \frac{\Delta x_s + \gamma \Delta x_g}{1+\gamma}}_{=\tilde{m}} + \underbrace{\frac{\tilde{N} + \gamma \tilde{N}}{1+\gamma}}_{=\tilde{N}} \tilde{m}^2 + \underbrace{\frac{2\gamma \tilde{N} - 2\gamma \tilde{N}}{1+\gamma}}_{=0} \tilde{m} \tilde{h} + \underbrace{\frac{\gamma^2 \tilde{M} + \gamma \tilde{M}}{1+\gamma}}_{=\gamma \tilde{M}} \tilde{h}^2, \quad (D.27)$$

I obtain

$$t = t_0 + \tilde{w} \tilde{m} + \tilde{N} \tilde{m}^2 + \gamma \tilde{M} \tilde{h}^2. \quad (D.28)$$

Final formula is obtained by squaring (D.28) and neglecting the terms of higher order than the second:

$$t^2(\tilde{m}, \tilde{h}) = \left[t_0 + \tilde{w} \tilde{m}\right]^2 + 2t_0 \left[\tilde{N} \tilde{m}^2 + \gamma \tilde{M} \tilde{h}^2\right]. \quad (D.29)$$

D.4 Derivation of n-CRS-PS stacking operator

In this section I discuss the derivation of the 2D n-CRS-PS formula (4.13). I begin with the DSR-PS stacking operator (D.25). Using notation \tilde{F} (4.14), the DSR-PS stacking operator reads:

$$t(\tilde{m}, \tilde{h}) = \frac{1}{1+\gamma} \sqrt{\tilde{F}(\Delta x_s) + 2t_0(\tilde{M} - \tilde{N})(\gamma\tilde{h})^2} + \frac{\gamma}{1+\gamma} \sqrt{\tilde{F}(\Delta x_g) + 2t_0(\tilde{M} - \tilde{N})\tilde{h}^2}. \quad (\text{D.30})$$

If I square the right-hand side of the last expression

$$t(\tilde{m}, \tilde{h}) = \sqrt{\left[\frac{1}{1+\gamma} \sqrt{\tilde{F}(\Delta x_s) + 2t_0(\tilde{M} - \tilde{N})(\gamma\tilde{h})^2} + \frac{\gamma}{1+\gamma} \sqrt{\tilde{F}(\Delta x_g) + 2t_0(\tilde{M} - \tilde{N})\tilde{h}^2} \right]^2}, \quad (\text{D.31})$$

"take out" $2t_0(\tilde{M} - \tilde{N})\tilde{h}^2$ from the square roots and neglect the terms of higher order than the second, I obtain the n-CRS-PS stacking operator:

$$t(m, h) = \sqrt{\left[\frac{1}{1+\gamma} \sqrt{\tilde{F}(\tilde{m} - \gamma\tilde{h})} + \frac{\gamma}{1+\gamma} \sqrt{\tilde{F}(\tilde{m} + \tilde{h})} \right]^2 + 2t_0\gamma(\tilde{M} - \tilde{N})\tilde{h}^2}. \quad (\text{D.32})$$

D.5 DSR-PS stacking operator in CMP coordinates

For some application, it might be useful to express the DSR-PS stacking operator in the standard CMP coordinates. The midpoint displacement and the half-offset in the γ -CMP and standard CMP coordinates have the following relation:

$$\tilde{m} = m + \sigma h, \quad \tilde{h} = v h, \quad (\text{D.33})$$

where

$$\sigma = \frac{\gamma - 1}{\gamma + 1}, \quad v = \frac{2}{\gamma + 1}. \quad (\text{D.34})$$

Substitution of \tilde{m} and \tilde{h} into (D.25) yields, after some algebra:

$$t(m, h) = \frac{1}{1+\gamma} \sqrt{\left[t_0 + \tilde{w}\Delta x_s \right]^2 + 2t_0 \left[\tilde{N}m^2 - 2\tilde{N}mh + [\tilde{N} + \gamma^2 v^2(\tilde{M} - \tilde{N})]h^2 \right]} + \frac{\gamma}{1+\gamma} \sqrt{\left[t_0 + \tilde{w}\Delta x_g \right]^2 + 2t_0 \left[\tilde{N}m^2 + 2\tilde{N}mh + [\tilde{N} + v^2(\tilde{M} - \tilde{N})]h^2 \right]} \quad (\text{D.35})$$

Similarly, the 3D DSR-PS stacking operator in the standard CMP coordinates reads:

$$t(\mathbf{m}, \mathbf{h}) = \frac{1}{1+\gamma} \sqrt{\left[t_0 + \tilde{\mathbf{w}}^T \Delta \mathbf{x}_s \right]^2 + 2t_0 \left[\mathbf{m}^T \tilde{\mathbf{N}} \mathbf{m} - 2\mathbf{m}^T \tilde{\mathbf{N}} \mathbf{h} + \mathbf{h}^T [\tilde{\mathbf{N}} + \gamma^2 v^2(\tilde{\mathbf{M}} - \tilde{\mathbf{N}})] \mathbf{h} \right]} + \frac{\gamma}{1+\gamma} \sqrt{\left[t_0 + \tilde{\mathbf{w}}^T \Delta \mathbf{x}_g \right]^2 + 2t_0 \left[\mathbf{m}^T \tilde{\mathbf{N}} \mathbf{m} + 2\mathbf{m}^T \tilde{\mathbf{N}} \mathbf{h} + \mathbf{h}^T [\tilde{\mathbf{N}} + v^2(\tilde{\mathbf{M}} - \tilde{\mathbf{N}})] \mathbf{h} \right]}. \quad (\text{D.36})$$

Appendix E

PS exact solution

The problem of reflection from the circular mirror has a very long history. This problem is known as Alhazen's problem ([Dörrie, 1965](#)) and can be traced further back at least to Ptolemy's time ([Neumann, 1998](#)). The problem of reflection from the circular mirror is identical to the circular billiard problem. ([Neumann, 1998](#)) and [Drexler and Gander \(1998\)](#) proved that the circular billiard problem typically has two or four solutions corresponding to the roots of fourth-order algebraic equation. [Landa et al. \(2010\)](#) used this idea to improve the quality of MF stacking operator.

In this appendix I discuss how to extend the solution proposed by [Drexler and Gander \(1998\)](#) to the case of converted waves.

E.1 Method

In the case of converted waves, the problem can be formulated as follows. Given a source x_s , a receiver x_g and a circular reflector. How to find a point on the circular reflector, where a seismic ray from x_s to x_g reflects, assuming that the mode conversion from P to S occurs on reflection?

Following the paper of [Drexler and Gander \(1998\)](#), I place the source x_s at the point $(-h, 0)$, the receiver x_g at the point $(h, 0)$ and assume that the reflector is a circle of unit radius and center at the point (m_1, m_2) , i.e., the circle is given by equation:

$$(x - m_1)^2 + (z - m_2)^2 = 1. \quad (\text{E.1})$$

I denote by v_p and v_s velocities of P- and S-waves, $\gamma \equiv v_p/v_s$.

Following [Drexler and Gander \(1998\)](#), I introduce the term "isochrone". By definition, at each point on the isochrone curve Snell's law is carried out for the incident and the reflected

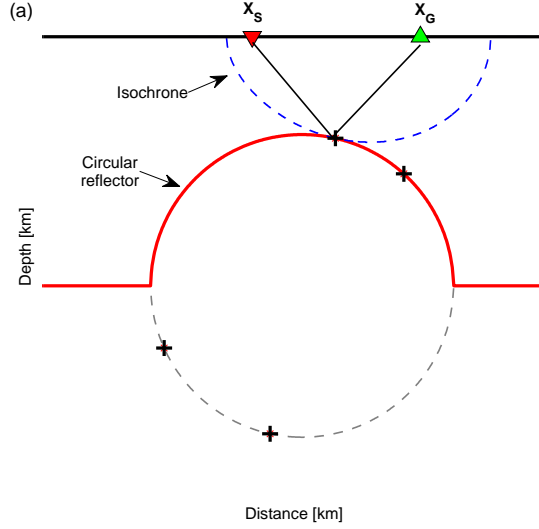


Figure E.1: Typically, equation (E.3) has four real roots. Corresponding reflection points are shown as black crosses. Only the root, giving the smallest value of traveltime, yields the required reflection point.

rays. In the case of converted waves, the isochrone is given by equation (see section E.2):

$$\sqrt{(x+h)^2+z^2} + \gamma\sqrt{(x-h)^2+z^2} = 2\sigma. \quad (\text{E.2})$$

Coefficient 2σ has a clear physical meaning of the product of the traveltime and the velocity of P-waves. In the case of monotypic waves ($\gamma = 1$), the isochrone (E.2) is an ellipse. The reflection point coordinates may be found as a solution of the system of three equations: the equation of circle (E.1), the equation of isochrone (E.2) and the condition for tangency between the circle and the isochrone (see section E.3). This system of nonlinear equations in variables $\{x, z, \sigma\}$ leads to the sixth-order algebraic equation:

$$\beta_6 u^6 + \beta_5 u^5 + \beta_4 u^4 + \beta_3 u^3 + \beta_2 u^2 + \beta_1 u + \beta_0 = 0, \quad (\text{E.3})$$

where coefficients $\beta_i, i = 0, \dots, 6$ depend on parameters h, γ, m_1, m_2 (see section E.4). The reflection points are equal:

$$x_r = m_1 + \cos \theta, \quad z_r = m_2 + \sin \theta, \quad \theta = 2 \arctan u. \quad (\text{E.4})$$

In most cases equation (E.3) has four real roots and two complex roots. The typical situation is shown in Figure E.1. Among real roots, the root, giving the smallest value of traveltime, yields the required reflection point.

E.2 Isochrone of converted wave

I assume that for the fixed traveltime t the isochrone is given in parametric form: $\mathbf{r} = \mathbf{r}(\tau)$. I denote by $\mathbf{r}_s(\tau)$ and $\mathbf{r}_g(\tau)$ radius vectors describing the isochrone from the position of

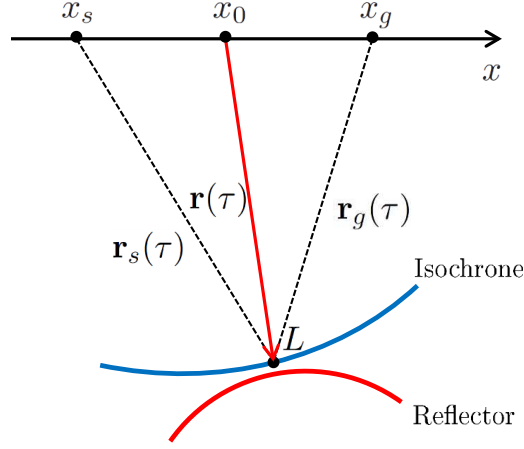


Figure E.2: Illustration of the notations used in the derivation of the isochrone equation.

source x_s and receiver x_g , respectively (see Figure E.2). If L is an arbitrary point on the isochrone, and \mathbf{n} is a unit normal vector of the isochrone, then Snell's law may be written as:

$$\sin(\widehat{\mathbf{r}_s(\tau), \mathbf{n}(\tau)}) = \gamma \sin(\widehat{\mathbf{r}_g(\tau), \mathbf{n}(\tau)}). \quad (\text{E.5})$$

If instead of the normal I consider a unit tangent vector \mathbf{k} , the Snell's law will look like:

$$\cos(\widehat{\mathbf{r}_s(\tau), \mathbf{k}(\tau)}) = -\gamma \cos(\widehat{\mathbf{r}_g(\tau), \mathbf{k}(\tau)}). \quad (\text{E.6})$$

Now, I use the definition of the scalar product of vectors, substitute expression for the unit tangent vector $\mathbf{k} = \frac{\dot{\mathbf{r}}(\tau)}{|\dot{\mathbf{r}}(\tau)|}$, multiply equation (E.6) by $|\dot{\mathbf{r}}(\tau)|$, and note that $\dot{\mathbf{r}}(\tau) = \dot{\mathbf{r}}_s(\tau) = \dot{\mathbf{r}}_g(\tau)$. Finally, I obtain:

$$\frac{\mathbf{r}_s(\tau) \cdot \dot{\mathbf{r}}_s(\tau)}{|\mathbf{r}_s(\tau)|} = -\gamma \frac{\mathbf{r}_g(\tau) \cdot \dot{\mathbf{r}}_g(\tau)}{|\mathbf{r}_g(\tau)|}. \quad (\text{E.7})$$

This expression is a total derivative with respect to τ :

$$\frac{d}{d\tau} |\mathbf{r}_s(\tau)| = -\gamma \frac{d}{d\tau} |\mathbf{r}_g(\tau)|. \quad (\text{E.8})$$

Rearranging terms and carrying out the integration yields:

$$|\mathbf{r}_s(\tau)| + \gamma |\mathbf{r}_g(\tau)| = 2\sigma, \quad (\text{E.9})$$

where 2σ is the integration constant. The coordinate representation of $\mathbf{r}_s, \mathbf{r}_g$ in equation (E.9) yields the equation of isochrone:

$$\sqrt{(x+h)^2 + z^2} + \gamma \sqrt{(x-h)^2 + z^2} = 2\sigma. \quad (\text{E.10})$$

E.3 Tangency condition

The reflection point (x_r, z_r) should satisfy Fermat's principle, according to which the reflected ray prefers the path, which minimizes the traveltime. Mathematically, this

is equivalent to the fact that the circle and the isochrone must touch each other at the reflection point. If implicit functions F and G denote the circle (E.1) and the isochrone (E.2), the condition of tangency between the curves, may be written as follows:

$$\left(\frac{\partial F}{\partial x}\right)\left(\frac{\partial G}{\partial z}\right) - \left(\frac{\partial F}{\partial z}\right)\left(\frac{\partial G}{\partial x}\right) = 0. \quad (\text{E.11})$$

The solution of equation (E.11) with respect to σ^2 yields the traveltime of converted wave as a function of reflection point:

$$\sigma^2 = (1 + \gamma^2) \left[2xh + \Theta\Delta \right] \frac{\Lambda + \Delta}{4(\Lambda\Delta + 1)}, \quad (\text{E.12})$$

where the following notations are made:

$$\Delta = \frac{1 - \gamma^2}{1 + \gamma^2}, \quad \Lambda = h \frac{z - m_2}{zm_1 - xm_2}, \quad \Theta = x^2 + z^2 + h^2. \quad (\text{E.13})$$

E.4 Coefficients of the sixth-order equation

The system of equations (E.1), (E.2) and (E.12) is solved in the following way:

1. isochrone (E.2) is twice squared to avoid irregularity;
2. σ^2 from (E.12) is substituted into (E.2);
3. x, z are substituted into (E.2) in the form $x = m_1 + \cos \theta$, $z = m_2 + \sin \theta$; they automatically satisfy equation of circle (E.1);
4. in (E.2) the variable change is made: $\theta = 2 \arctan u$.

Finally, the system reduces to the sixth-order algebraic equation for u :

$$\beta_6 u^6 + \beta_5 u^5 + \beta_4 u^4 + \beta_3 u^3 + \beta_2 u^2 + \beta_1 u + \beta_0 = 0, \quad (\text{E.14})$$

with the following coefficients:

$$\begin{aligned} \beta_6 &= (2h(m_1 - 1) - \Delta A_1)m_2^2; \\ \beta_5 &= 2h(m_1 - 1)B_1 - A_1B_2 - 4\Delta m_2^3; \\ \beta_4 &= 2h(m_1 + 1)m_2^2 + 2h(m_1 - 1)C_1 - A_2\Delta m_2^2 - 4m_2B_2 - A_1C_2; \\ \beta_3 &= -8m_2(4hm_1 + \Delta(4m_1^2 - m_2^2)); \\ \beta_2 &= 2h(m_1 - 1)m_2^2 + 2h(m_1 + 1)C_1 - A_1\Delta m_2^2 + 4m_2B_2 - A_2C_2; \\ \beta_1 &= -2h(m_1 + 1)B_1 + A_2B_2 - 4\Delta m_2^3; \\ \beta_0 &= (2h(m_1 + 1) - \Delta A_2)m_2^2; \end{aligned}$$

where:

$$\begin{aligned}A_1 &= (m_1^2 + m_2^2 + 1 + h^2 - 2m_1); \\A_2 &= (m_1^2 + m_2^2 + 1 + h^2 + 2m_1); \\B_1 &= (4\Delta hm_2 + 4m_1m_2); \\B_2 &= (4hm_2 + 4\Delta m_1m_2); \\C_1 &= (8\Delta hm_1 + 4h^2 - 2m_2^2 + 4m_1^2); \\C_2 &= (8hm_1 + \Delta(4h^2 - 2m_2^2 + 4m_1^2)).\end{aligned}$$

List of Figures

1.1	Seismic reflection experiment	6
1.2	Simple earth models	8
1.3	CMP stack	10
1.4	Ray scheme for the shifted hyperbola	11
1.5	Multidimensional stack	13
1.6	Kinematic wavefield attributes	15
1.7	Ray schemes for the MF, i-CRS and n-CRS methods	18
1.8	Classification of the multidimensional stacking operators	23
2.1	2D simplified model	28
2.2	Special ray-centered coordinate system	30
2.3	NIP experiment in the 3D case	31
2.4	Normal experiment in the 3D case	33
2.5	Paraboloidal and ellipsoidal reflectors	34
2.6	3D simplified model	36
3.1	Complex 3D model and the corresponding simplified model	44
3.2	Relative errors of the traveltimes in the simplified model	45

3.3	Error of the 3D i-CRS approximation as a function of the iteration number	46
3.4	Illustration of the analytical reflectors	47
3.5	Relative errors of 3D stacking operators along the 2D profile	49
3.6	Model with the reflector of varying curvature	50
3.7	Computational difficulty of the 3D stacking operators	51
4.1	PS reflection experiment	55
4.2	Definition of the γ -CMP coordinates	57
4.3	Accuracy of the stacking operators for converted waves	62
4.4	Gradient velocity model	64
4.5	Accuracy of the wavefield attributes	65
4.6	Complex velocity model	67
4.7	Stacked PP and PS sections	67
5.1	Illustration of the common-offset reflection experiment	70
5.2	Illustration of the CS, CR, CMP and CO experiments	74
5.3	Classification of the new multidimensional stacking operators	82
D.1	Notations used in the derivation of $\sin \vartheta$	100
E.1	Roots of the sixth-order algebraic equation	106
E.2	Notations used in the derivation of the isochrone equation	107

List of Tables

1.1	Evolution of stacking operators	22
3.1	RMS travelttime errors	48
4.1	Parameters of the constant velocity model	62
4.2	Parameters of the constant-gradient velocity model	66
5.1	Wavefront curvatures in terms of the elements of the propagator matrix. . .	73

List of Symbols

General notation rules

- a – scalar;
- \mathbf{a} – 2D vector, $\mathbf{a} \equiv \{a_x, a_y\}$, or $\mathbf{a} \equiv \{a_i\}, i = 1, 2$;
- $\hat{\mathbf{a}}$ – 3D vector, $\hat{\mathbf{a}} \equiv \{a_x, a_y, a_z\}$, or $\hat{\mathbf{a}} \equiv \{a_i\}, i = 1, 2, 3$;
- a_{ij} – element of matrix;
- A_{ij} – tensor;
- \mathbf{A} – (2×2) matrix;
- $\hat{\mathbf{A}}$ – (3×3) matrix;
- $\bar{\mathbf{A}}$ – (4×4) matrix.

Coordinate systems

- \mathcal{L} – General Cartesian coordinate system;
- \mathcal{L}' – Special ray-centered coordinate system;
- $\tilde{\mathcal{L}}$ – γ -CMP coordinate system;
- $\tilde{\mathcal{L}}'$ – Standard ray-centered coordinate system.

Subscripts

- $_0$ indicate that the value is related to the central ray;
- $_s$ indicate that the value is related to the source;
- $_g$ indicate that the value is related to the receiver;
- $_r$ indicate that the value is related to the reflection point.

Coordinates

- \mathbf{x}_{s_0} – shot coordinates of the central ray (CO case);
- \mathbf{x}_{g_0} – receiver coordinates of the central ray (CO case);
- $\mathbf{x}_0 \equiv \frac{1}{2}(\mathbf{x}_{g_0} + \mathbf{x}_{s_0})$ – midpoint of the central ray;
- $\mathbf{h}_0 \equiv \frac{1}{2}(\mathbf{x}_{g_0} - \mathbf{x}_{s_0})$ – half-offset of the central ray;
- $\mathbf{x}_{s_0} = \mathbf{x}_{g_0} = \mathbf{x}_0$ - in the ZO case;
- \mathbf{x}_s – shot coordinates of the paraxial ray;
- \mathbf{x}_g – receiver coordinates of the paraxial ray;
- $\mathbf{x}_m \equiv \frac{1}{2}(\mathbf{x}_g + \mathbf{x}_s)$ – midpoint of the paraxial ray;
- $\mathbf{h}_m \equiv \frac{1}{2}(\mathbf{x}_g - \mathbf{x}_s)$ – half-offset of the paraxial ray;
- $\mathbf{h} \equiv \mathbf{h}_m - \mathbf{h}_0$ – half-offset;
- $\mathbf{m} \equiv \mathbf{x}_m - \mathbf{x}_0$ – midpoint displacement;
- $\Delta\mathbf{x}_s \equiv \mathbf{x}_s - \mathbf{x}_{s_0}$ – shot displacement;
- $\Delta\mathbf{x}_g \equiv \mathbf{x}_g - \mathbf{x}_{g_0}$ – receiver displacement;
- $\tilde{\mathbf{x}}_m \equiv \frac{1}{1+\gamma}(\gamma\mathbf{x}_g + \mathbf{x}_s)$ – midpoint of the paraxial ray (PS case);
- $\tilde{\mathbf{m}} \equiv \tilde{\mathbf{x}}_m - \mathbf{x}_0$ – midpoint displacement (PS case);
- $\tilde{\mathbf{h}} \equiv \frac{1}{1+\gamma}(\mathbf{x}_g - \mathbf{x}_s)$ – half-offset (PS case);
- $\hat{\mathbf{x}}_{r_0}$ – reflection point of the central ray;
- $\hat{\mathbf{x}}_r$ – reflection poin of the paraxial ray;
- $\Delta\hat{\mathbf{x}}_r$ – displacement of the reflection point;
- $\hat{\mathbf{x}}_{ref}(\vartheta, \varphi) \equiv (x_{ref}(\vartheta, \varphi), y_{ref}(\vartheta, \varphi), z_{ref}(\vartheta, \varphi))$ – parametic representation of the reflector surface (3D case);
- $(x_{ref}(\vartheta), z_{ref}(\vartheta))$ – parametic representation of the reflector (2D case);
- t_0 – travelttime of the central ray;
- t – travelttime of the paraxial ray;
- t_p – focusing time;
- α, β – dip and azimuth angles of the central ray (ZO case);
- $\alpha_s, \beta_s / \alpha_g, \beta_g$ – dip and azimuth angles of the cental ray at the position of source/receiver (CO case);

- $\hat{\mathbf{p}}_s / \hat{\mathbf{p}}_g$ – slowness vector at the position of source/receiver;
- $\bar{\bar{\mathbf{T}}}$ – surface-to-surface ray propagator matrix;
- $\mathbf{A}, \mathbf{B}, \mathbf{C}, \mathbf{D}$ – elements of the propagator matrix;
- \mathbf{I} – identity matrix;
- $\hat{\mathbf{R}}_x, \hat{\mathbf{R}}_y, \hat{\mathbf{R}}_z$ – basic rotation matrices;
- $\hat{\mathbf{R}}$ – rotation matrix that accounts for the transformation from the ray-centered to the general Cartesian coordinate system;
- \mathbf{R} – upper left (2×2) part of the rotation matrix $\hat{\mathbf{R}}$;
- v – constant overburden velocity;
- v_{NMO} – normal moveout velocity;
- v_{RMS} – root-mean-square velocity;
- v_0 – near-surface velocity (ZO case);
- v_s – near-surface velocity at the source position (CO case);
- v_g – near-surface velocity at the receiver position (CO case);
- v_P – P-wave velocity (PS case);
- v_S – S-wave velocity (PS case);
- $\gamma \equiv \frac{v_P}{v_S}$ – ratio of the P- and S-wave velocities (PS case);
- v_{PS} – effective velocity of the PS wave (PS case);
- R_{NIP} – radius of curvature of the NIP wave (2D case);
- R_{N} – radius of curvature of the normal wave (2D case);
- R – radius of curvature of the reflector (2D case);
- \mathbf{K}_{NIP} – curvature of the NIP wave (3D case);
- \mathbf{K}_{N} – curvature of the normal wave (3D case);
- \mathbf{K}_{R} – curvature of the reflector (3D case);
- R_{NIP}^* – depth of the reflector in the simplified model (3D case);
- A_{ij} – density normalized elastic parameters,
- θ, ϕ – phase polar and azimuthal angles,
- $\mathbf{n}(\theta, \phi)$ – direction of phase velocity,
- $v(\theta, \phi)$ – phase velocity;

- Θ, Φ – group polar and azimuthal angles;
- $\zeta(\Theta, \Phi)$ – group velocity;
- \mathcal{S} – location of the NIP;
- \mathcal{S}^* – location of the center of curvature of the NIP wave
- \mathcal{O}^* – location of the center of curvature of the normal wave

List of Publications

The results of this thesis were presented at the following international conferences:

- Abakumov, I., Schwarz, B., Kashtan, B.M. and Gajewski, D. (2012) Implementation of double square root travelttime approximation for converted waves. In *5th Saint-Petersburg International Conference and Exhibition 2012, Saint-Petersburg, Extended Abstract*. P012
- Abakumov, I., Schwarz, B., Kashtan, B., Vanelle, C. and Gajewski, D. (2012) Double-square root travelttime approximation for converted waves. In *SEG Technical Program Expanded Abstracts 2012*, pages 1-6.
- Abakumov, I., Taganayeva, A., Kashtan, B. and Gajewski, D. (2013) Extension of the i-CRS stacking operator for the 3D case. In *International youth oil and gas forum, Almaty, Kazakhstan, Expanded Abstracts*, pages 30-32.
- Abakumov, I. and Gajewski, D. (2014) 3D i-CRS stacking operator in homogeneous isotropic media. In *74th Annual Meeting of the German Geophysical Society, Karlsruhe, Germany*.
- Abakumov, I., Kashtan, B. and Gajewski, D. (2015) 3D i-CRS stacking operator. In *Workshop meeting APSLIM 2015, Loucen Castle, Czech Republic*.

References

- Abakumov, I., Taganayeva, A., Kashtan, B., and Gajewski, D. (2013). Extension of the i-CRS stacking operator for the 3D case. In *International youth oil and gas forum, Almaty, Kazakhstan, Expanded Abstracts*, pages 30–32.
- Ahmed, K. A. (2015). *3-D seismic processing in crystalline rocks using the common reflection surface stack*. PhD thesis, University of Hamburg.
- Bakhtiari Rad, P., Vanelle, C., and Gajewski, D. (2015). 3D CRS-based prestack diffraction separation and imaging. In *77th EAGE Conference and Exhibition 2015*. WS06 A04.
- Bauer, A., Schwarz, B., and Gajewski, D. (2015). Prestack diffraction enhancement using a traveltimes decomposition approach. In *SEG Technical Program Expanded Abstracts 2015*, pages 3820–3824.
- Bauer, A., Schwarz, B., and Gajewski, D. (2016a). Enhancement of prestack diffraction data and attributes using a traveltimes decomposition approach. *Studia Geophysica et Geodaetica*, 60(3):471–486.
- Bauer, A., Schwarz, B., Lotze, M., Werner, T., and Gajewski, D. (2016b). Utilizing diffractions in wavefront-based tomography. In *78th EAGE Conference and Exhibition 2016*. Tu SRS2 10.
- Baykulov, M., Dümmong, S., and Gajewski, D. (2011). From time to depth with CRS attributes. *Geophysics*, 76(4):S151–S155.
- Baykulov, M. and Gajewski, D. (2009). Prestack seismic data enhancement with partial common-reflection-surface (CRS) stack. *Geophysics*, 74(3):V49–V58.
- Bergler, S., Duvencak, E., Höcht, G., Zhang, Y., and Hubral, P. (2002). Common-reflection-surface stack for converted waves. *Studia Geophysica et Geodaetica*, 46(2):165–175.
- Berkovitch, A., Belfer, I., Hassin, Y., and Landa, E. (2009). Diffraction imaging by multifocusing. *Geophysics*, 74(6):WCA75–WCA81.
- Berkovitch, A., Deev, K., and Landa, E. (2011). How non-hyperbolic multifocusing improves depth imaging. *First Break*, 29(9):103–111.
- Berkovitch, A., Deev, K., Pelman, D., and Rauch-Davies, M. (2012). Multifocusing 3D diffraction imaging. In *74th EAGE Conference and Exhibition incorporating SPE EUROPEC 2012*. Y026.

- Bolshykh, S. F. (1956). About an approximate representation of the reflected wave traveltimes in the case of a multi-layered medium. *Applied Geophysics*, 15:3–15. (in Russian).
- Bortfeld, R. (1989). Geometrical ray theory: Rays and traveltimes in seismic systems (second-order approximations of the traveltimes). *Geophysics*, 54(3):342–349.
- Buchanan, D. J., Davis, R., and Jackson, P. J. (1983). Method of stacking seismic data. U. S. Patent, 4,393,484.
- Castle, R. J. (1994). A theory of normal moveout. *Geophysics*, 59(6):983–999.
- Červený, V. (2001). *Seismic ray theory*. Cambridge University Press.
- Coulombe, C. A., Stewart, R. R., and Jones, M. J. (1996). AVO processing and interpretation of VSP data. *Canadian Journal of Exploration Geophysics*, 32(1):41–62.
- Cox, M. (1999). *Static corrections for seismic reflection surveys*. Society of Exploration Geophysicists, Tulsa.
- Daley, P. F. and Krebes, E. S. (2005). Quasi-compressional group velocity approximations in a weakly anisotropic orthorhombic medium. *CREWES Research Report*, 17.
- de Bazelaire, E. (1988). Normal moveout revisited: Inhomogeneous media and curved interfaces. *Geophysics*, 53(2):143–157.
- Dell, S. and Gajewski, D. (2011). Common-reflection-surface-based workflow for diffraction imaging. *Geophysics*, 76(5):S187–S195.
- Della Moretta, D., Kluever, T., and Marchetti, P. (2006). 3D CRS-based velocity model building - an accurate and cost-effective approach. In *68th EAGE Conference and Exhibition 2006*. P155.
- Dix, C. H. (1955). Seismic velocities from surface measurements. *Geophysics*, 20(1):68–86.
- Dörrie, H. (1965). *100 great problems of elementary mathematics: their history and solution*. Dover Publications, New York.
- Drexler, M. and Gander, M. J. (1998). Circular billiard. *SIAM review*, 40(2):315–323.
- Dümmong, S. and Gajewski, D. (2008). A multiple suppression method via CRS attributes. In *SEG Technical Program Expanded Abstracts 2008*, pages 2531–2535.
- Dürbaum, H. (1954). Zur Bestimmung von Wellengeschwindigkeiten aus reflexionsseismischen Messungen. *Geophysical Prospecting*, 2(2):151–167.
- Duveneck, E. (2004). Velocity model estimation with data-derived wavefront attributes. *Geophysics*, 69(1):265–274.
- Fomel, S. and Kazinnik, R. (2013). Non-hyperbolic common reflection surface. *Geophysical Prospecting*, 61(1):21–27.

- Fomel, S., Landa, E., and Taner, M. T. (2007). Poststack velocity analysis by separation and imaging of seismic diffractions. *Geophysics*, 72(6):U89–U94.
- Fomel, S. and Stovas, A. (2010). Generalized nonhyperbolic moveout approximation. *Geophysics*, 75(2):U9–U18.
- French, W. S. (1974). Two-dimensional and three-dimensional migration of model-experiment reflection profiles. *Geophysics*, 39(3):265–277.
- Fromm, G., Krey, T., and Wiest, B. (1985). Static and dynamic corrections. In *Handbook of Geophysical Exploration: Seismic Shear Waves*, volume 15A, pages 191–225. Geophysical Press.
- Garabito, G., Stoffa, P. L., Lucena, L. S., and Cruz, J. C. R. (2012). Part I – CRS stack: Global optimization of the 2D CRS-attributes. *Journal of Applied Geophysics*, 85:92–101.
- Garotta, R. (1985). Observation of shear waves and correlation with P events. In *Handbook of Geophysical Exploration: Seismic Shear Waves*, volume 15A, pages 1–86. Geophysical Press.
- Gelchinsky, B. (1989). Homeomorphic imaging in processing and interpretation of seismic data (fundamentals and schemes). In *SEG Technical Program Expanded Abstracts 1989*, pages 983–988.
- Gelchinsky, B., Berkovitch, A., and Keydar, S. (1999). Multifocusing homeomorphic imaging: Part 1. Basic concepts and formulas. *Journal of Applied Geophysics*, 42(3):229–242.
- Grechka, V. and Tsvankin, I. (1999). 3-D moveout velocity analysis and parameter estimation for orthorhombic media. *Geophysics*, 64(3):820–837.
- Green, C. (1938). Velocity determinations by means of reflection profiles. *Geophysics*, 3(4):295–305.
- Hale, D. (1991). *Dip moveout processing*. Society of Exploration Geophysicists, Tulsa.
- Harris, N. R. (1968). Stacking of seismic traces having common offset distances. U. S. Patent 3,381,266.
- Höcht, G., de Bazelaire, E., Majer, P., and Hubral, P. (1999). Seismics and optics: hyperbolae and curvatures. *Journal of Applied Geophysics*, 42(3):261–281.
- Hoecht, G., Ricarte, P., Bergler, S., and Landa, E. (2009). Operator-oriented CRS interpolation. *Geophysical Prospecting*, 57(6):957–979.
- Hubral, P. (1983). Computing true amplitude reflections in a laterally inhomogeneous earth. *Geophysics*, 48(8):1051–1062.
- Hubral, P. and Krey, T. (1980). *Interval velocities from seismic reflection time measurements*. Society of Exploration Geophysicists, Tulsa.

- Hubral, P., Schleicher, J., and Tygel, M. (1992). Three-dimensional paraxial ray properties: Part I. Basic relations. *Journal of Seismic Exploration*, 1(3):265–279.
- Iverson, W. P., Fahmy, B. A., and Smithson, S. B. (1989). v_p/v_s from mode-converted P-SV reflections. *Geophysics*, 54(7):843–852.
- Jäger, R., Mann, J., Höcht, G., and Hubral, P. (2001). Common-reflection-surface stack: Image and attributes. *Geophysics*, 66(1):97–109.
- Kendall, R. R. and Davis, T. L. (1996). The cost of acquiring shear waves. *The Leading Edge*, 15(8):943–944.
- Khaidukov, V., Landa, E., and Moser, T. J. (2004). Diffraction imaging by focusing-defocusing: An outlook on seismic superresolution. *Geophysics*, 69(6):1478–1490.
- Landa, E. (2007). *Beyond conventional seismic imaging*. EAGE Publications.
- Landa, E., Gurevich, B., Keydar, S., and Trachtman, P. (1999). Application of multifocusing method for subsurface imaging. *Journal of Applied Geophysics*, 42(3):283–300.
- Landa, E., Keydar, S., and Moser, T. J. (2010). Multifocusing revisited - inhomogeneous media and curved interfaces. *Geophysical Prospecting*, 58(6):925–938.
- Levin, F. K. (1971). Apparent velocity from dipping interface reflections. *Geophysics*, 36(3):510–516.
- Malovichko, A. A. (1978). A new representation of the travelttime curve of reflected waves in horizontally layered media. *Applied Geophysics*, 91(1):47–53. (in Russian).
- Mann, J. (2002). *Extensions and applications of the common-reflection-surface stack method*. PhD thesis, University of Karlsruhe.
- Mann, J., Jäger, R., Müller, T., Höcht, G., and Hubral, P. (1999). Common-reflection-surface stack — a real data example. *Journal of Applied Geophysics*, 42(3):301–318.
- Mayne, W. H. (1962). Common reflection point horizontal data stacking techniques. *Geophysics*, 27(6):927–938.
- Moser, T. J. and Červený, V. (2007). Paraxial ray methods for anisotropic inhomogeneous media. *Geophysical Prospecting*, 55(1):21–37.
- Müller, N.-A. (2003). *The 3D common-reflection-surface stack: theory and application*. PhD thesis, University of Karlsruhe.
- Müller, N.-A. (2009). Treatment of conflicting dips in the 3D common-reflection-surface stack. *Geophysical Prospecting*, 57(6):981–995.
- Müller, T. (1999). *The common reflection surface stack method – seismic imaging without explicit knowledge of the velocity model*. PhD thesis, University of Karlsruhe.
- Naess, O. E. (1982). Single-trace processing using iterative CDP-stacking. *Geophysical Prospecting*, 30(5):641–652.

- Nelson, R. (2001). *Geologic analysis of naturally fractured reservoirs*. Gulf Professional Publishing.
- Neumann, P. M. (1998). Reflections on reflection in a spherical mirror. *American Mathematical Monthly*, 105(6):523–528.
- Rashed, M. (2014). Fifty years of stacking. *Acta Geophysica*, 62(3):505–528.
- Rauch-Davies, M., Berkovitch, A., Pelman, D., Deev, K., and Landa, E. (2013). Using multi-focusing 3D diffraction imaging to predict fracture corridors/swarms in the Bazhenov formation. In *75th EAGE Conference and Exhibition incorporating SPE EUROPEC 2013*. We 01 08.
- Schleicher, J., Tygel, M., and Hubral, P. (1993). Parabolic and hyperbolic paraxial two-point traveltimes in 3D media. *Geophysical Prospecting*, 41(4):495–513.
- Schwarz, B. (2011). A new nonhyperbolic multi-parameter stacking operator. Master's thesis, University of Hamburg.
- Schwarz, B., Vanelle, C., and Gajewski, D. (2015). Shifted hyperbola revisited - the two faces of NMO. In *77th EAGE Conference and Exhibition 2015*. We N107 11.
- Schwarz, B., Vanelle, C., Gajewski, D., and Kashtan, B. (2014). Curvatures and inhomogeneities: An improved common-reflection-surface approach. *Geophysics*, 79(5):S231–S240.
- Schwarz, B., Vanelle, C., Kashtan, B., and Gajewski, D. (2012). i-CRS: application of a new multi-parameter stacking approach to complex media. In *SEG Technical Program Expanded Abstracts 2012*, pages 1–5.
- Sengbush, R. L. (1983). *Seismic exploration methods*. IHRDC, Boston.
- Sheriff, R. E. and Geldart, L. P. (1995). *Exploration seismology*. Cambridge University Press.
- Slotboom, R. (1990). Converted wave (P-SV) moveout estimation. In *SEG Technical Program Expanded Abstracts 1990*, pages 1104–1106.
- Soleimani, M., Piruz, I., Mann, J., and Hubral, P. (2009). Common-reflection-surface stack: accounting for conflicting dip situations by considering all possible dips. *Journal of Seismic Exploration*, 18(3):271.
- Stewart, R. R., Gaiser, J. E., Brown, R. J., and Lawton, D. C. (2002). Converted-wave seismic exploration: Methods. *Geophysics*, 67(5):1348–1363.
- Taner, M. T. and Koehler, F. (1969). Velocity spectra-digital computer derivation applications of velocity functions. *Geophysics*, 34(6):859–881.
- Tessmer, G. and Behle, A. (1988). Common reflection point data-stacking technique for converted waves. *Geophysical Prospecting*, 36(7):671–688.

- Tessmer, G., Krajewski, P., Fertig, J., and Behle, A. (1990). Processing of PS-reflection data applying a common conversion-point stacking technique. *Geophysical Prospecting*, 38(3):267–268.
- Thomsen, L. (1999). Converted-wave reflection seismology over inhomogeneous, anisotropic media. *Geophysics*, 64(3):678–690.
- Tsvankin, I. (2012). *Seismic signatures and analysis of reflection data in anisotropic media*. Society of Exploration Geophysicists, Tulsa.
- Tygel, M., Müller, T., Hubral, P., and Schleicher, J. (1997). Eigenwave based multiparameter traveltime expansions. In *SEG Technical Program Expanded Abstracts 1997*, pages 1770–1773.
- Tygel, M., Santos, L. T., and Schleicher, J. (1999). Multifocus moveout revisited: derivations and alternative expressions. *Journal of Applied Geophysics*, 42(3):319–331.
- Ursin, B. (1982). Quadratic wavefront and traveltime approximations in inhomogeneous layered media with curved interfaces. *Geophysics*, 47(7):1012–1021.
- Vanelle, C. (2002). *Traveltime-based true-amplitude migration*. PhD thesis, University of Hamburg.
- Vanelle, C., Bobsin, M., Schemmert, P., Kashtan, B., Schwarz, B., and Gajewski, D. (2012a). i-CRS: a new multiparameter stacking operator for an/isotropic media. In *SEG Technical Program Expanded Abstracts 2012*, pages 1–5.
- Vanelle, C. and Gajewski, D. (2009). NIP-wave tomography for converted waves. In *12th Annual WIT Report*, pages 167–173. Wave Inversion Technology.
- Vanelle, C., Kashtan, B., Abakumov, I., and Gajewski, D. (2012b). A CRS-type stacking operator for converted waves. In *15th Annual WIT Report*, pages 179–187. Wave Inversion Technology.
- Vanelle, C., Kashtan, B., Dell, S., and Gajewski, D. (2010). A new stacking operator for curved subsurface structures. In *SEG Technical Program Expanded Abstracts 2010*, pages 3609–3613.
- Vermeer, G. J. O. (2002). *3D seismic survey design*. Society of Exploration Geophysicists, Tulsa.
- Walda, J. and Gajewski, D. (2015a). Global optimization of the CRS operator using a genetic algorithm. In *77th EAGE Conference and Exhibition 2015*. We N107 13.
- Walda, J. and Gajewski, D. (2015b). Handling the conflicting dip problem in the CRS/iCRS methods. In *77th EAGE Conference and Exhibition 2015*. We N107 09.
- Walda, J., Schwarz, B., and Gajewski, D. (2016). A competitive comparison of multiparameter stacking approaches. In *78th EAGE Conference and Exhibition 2016*. Th LHR2 09.

-
- Warner, M., Ratcliffe, A., Nangoo, T., Morgan, J., Umpleby, A., Shah, N., Vinje, V., Štekl, I., Guasch, L., Win, C., Conroy, G., and Bertrand, A. (2013). Anisotropic 3D full-waveform inversion. *Geophysics*, 78(2):R59–R80.
- Xie, Y. and Gajewski, D. (2016). Automatic estimation of the 3d crs attributes by a metaheuristic-based optimization. In *78th EAGE Conference and Exhibition 2016*. Th P6 09.
- Yilmaz, Ö. (2001). *Seismic data analysis*, volume 1. Society of Exploration Geophysicists, Tulsa.
- Zhang, Y., Bergler, S., and Hubral, P. (2001). Common-reflection-surface (CRS) stack for common offset. *Geophysical Prospecting*, 49(6):709–718.

Used software

The results of this thesis were derived on the working station running under a free GNU/Linux operating system.

Processing and visualisation of the seismic data was performed in an open source seismic utilities package Seismic Unix (Center for Wave Phenomena). Additional figures were generated using MATLAB (MathWorks) and Microsoft Power Point.

The Wave Inversion Technology (WIT) consortium provided further software for the CRS processing:

- 2D ZO CRS stack code as implemented by [Mann \(2002\)](#) with updates by [Schwarz \(2011\)](#).
- 3D ZO CRS stack code as implemented by [Müller \(2003\)](#) with updates by [Ahmed \(2015\)](#) and [Xie and Gajewski \(2016\)](#).

Synthetic datasets were generated with NORSAR-2D, and NORSAR-3D software (NORSAR Innovation AS).

The thesis itself was written on a PC with the free operating system Debian GNU/Linux with the typesetting system \LaTeX .

Acknowledgments

First and foremost, I would like to thank my supervisor **Prof. Dr. Dirk Gajewski** for careful supervision, valuable advices and constant support. I believe I was not an easy student to supervise, but Dirk wisely and patiently guided me in the right direction. I'm grateful for his enthusiasm and interest to my research which gave me the confidence and motivation to continue my work.

This work could not have been completed without the tremendous help and kindness of many people. I'm deeply grateful to:

- **Prof. Dr. Boris Kashtan** from St. Petersburg University. Many ideas in this thesis were inspired by discussions with Professor Kashtan;
- **PD Dr. Claudia Vanelle** for the fruitful discussions about stacking operators for converted waves, outstanding management talent, attention to details and for all her generosity;
- **Dr. Ekkehart Tessmer** for his almost "magic" help with all IT-related problems;
- **Prof. Dr. Martin Tygel** from the University of Campinas for the very inspiring discussion about the history of CRS;
- **Prof. Dr. Alexey Stovas** from Norwegian University of Science and Technology for his interest to the 3D auxiliary medium and for suggesting the term "curvature-induced anisotropy";
- **Dr. Benjamin Schwarz**. You were like an older brother for me. Thank you for all the knowledge and experience you have shared with me;
- **Dr. Khawar Ashfaq Ahmed** for his help with the 3D land data;
- **Dr. Sergius Dell** for his help, support, interest and sharing experience about 3D i-CRS stacking operator;
- **Jan Walda** for the very inspiring discussions about global optimization techniques;
- **Yujiang Xie** for providing his 3D CRS code with the global search of stacking parameters;

- **Paola Dal Corso, Manizheh Vefagh, Helmar-Sven Hansen and Natalia Kolanovska** for advices, information and administrative support.

Last but not least, I'd like to thank my family and friends, especially **Amel Hammami**, for their love and support.

Eidesstattliche Versicherung

Eidesstattliche Versicherung **Declaration on oath**

Hiermit erkläre ich an Eides statt, dass ich die vorliegende Dissertationsschrift selbst verfasst und keine anderen als die angegebenen Quellen und Hilfsmittel benutzt habe.

I hereby declare, on oath, that I have written the present dissertation by my own and have not used other than the acknowledged resources and aids.

Hamburg, den 8. November 2016
City and date

Unterschrift
Signature

A handwritten signature in black ink, appearing to be 'J. J.' or similar, written in a cursive style.